sciendo

Contributions to Geophysics and Geodesy Vol. 49/4, 2019 (391–402)

Indoor radon monitoring in selected fault zones, Slovakia – preliminary results from the summer monitoring period

Iveta SMETANOVÁ[1,*], Andrej MOJZEŠ[2], František MARKO[2], Kamil FEKETE[1], Kristián CSICSAY[1]

[1] Earth Science Institute, Slovak Academy of Sciences, Dúbravská cesta 9, P. O. Box 106, 840 05 Bratislava, Slovak Republic

[2] Faculty of Natural Sciences, Comenius University, Ilkovičova 6, 842 15 Bratislava, Slovak Republic

Abstract: Indoor radon survey in Sološnica, Vydrník and Zázrivá villages has been performed within the framework of the project "Multidisciplinary research of geophysical and structural parameters, and environmental impacts of faults of the Western Carpathians". Integration measurement of ^{222}Rn activity concentration has been carried out using RamaRn detectors in houses, offices, schools and kindergartens. Indoor radon activity in the summer monitoring period (June–August 2018) varied from values under the detection limit of 55 Bq/m^3 to 480 Bq/m^3. In 94% of rooms the radon activity below 200 Bq/m^3 was found. The results have been examined in respect of the most used building material and presence or absence of a cellar underneath the room. Indoor radon higher than 300 Bq/m^3 was measured only in rooms in direct contact with the subsoil.

Key words: radon, activity concentration, building, integral monitoring, survey

1. Introduction

Soil gas infiltration is recognized as the most important source of indoor radon concentration (IRC). Radon may enter in dwellings by diffusion or a pressure driven flow if suitable pathways between the soil and living spaces are present. Other sources, including building material and water extracted from wells, are of less importance (*WHO, 2009*). The building characteristics as thermal retrofit, presence or absence of a cellar and ventilation type and intensity may also significantly affect IRC (*Borgoni et al., 2014; Collignan et al., 2016*). Energy saving reconstructions of buildings often results in an increase of IRC (*Collignan et al., 2016; Fojtíková and Navrátilová-Rovenská, 2015*).

*corresponding author: e-mail: Iveta.Smetanova@savba.sk

doi: 10.2478/congeo-2019-0020

Geological fault mapping methods is difficult to apply in covered or built-up areas. The hidden morphology of the fault could be revealed by the high resolution soil radon survey. Many studies proved an increased soil radon activity in the proximity of active faults (*Burton et al., 2004; Font et al., 2008; Neri et al., 2011; Bonforte et al., 2013; Moreno et al., 2018*). The presence of faults nearby buildings may increase IRC (*Drolet and Martel, 2016; Neri et al., 2019*). However, not all surveys confirmed an elevated indoor radon in fault areas, because radon concentration level in a house is the result of many parameters and processes of different origin (*Font et al., 2008*).

In Slovakia, several indoor radon surveys were performed. The first indoor radon monitoring in randomly selected dwellings was conducted in the nineties, using the integral method (*Vičanová, 2003*). In 2005 radon research in dwellings situated on the fault zone was carried out, together with soil radon measurements, in the Malá Magura Mts. (Horná Nitra region of Central Slovakia), however the influence of the fault presence on radon concentration was not proven (*Mojzeš et al., 2017*). In recent years indoor radon monitoring was conducted within the frame of the Visegrad countries project and the common questionnaire and common measurement protocol was elaborated (*Műllerová et al., 2016*).

In this paper the preliminary results from the summer monitoring period (June–August 2018) in Sološnica, Vydrník and Zázrivá villages are presented and the potential influencing factors on IRC are evaluated. For Sološnica the results are compared also with the spring monitoring period (March–May 2018). The aim of this radon survey was to verify if the houses built on the fault zones are prone to high indoor radon. Indoor radon monitoring in above mentioned localities was performed within the framework of the project "Multidisciplinary research of geophysical and structural parameters, and environmental impacts of faults of the Western Carpathians".

2. Methods and site description

In three selected localities (Sološnica, Vydrník, Zázrivá) situated on the fault zones (Fig. 1) indoor radon monitoring has been carried out. The measurements were performed mainly in houses, but also offices, schools and kindergartens were included in this survey. Throughout the whole year

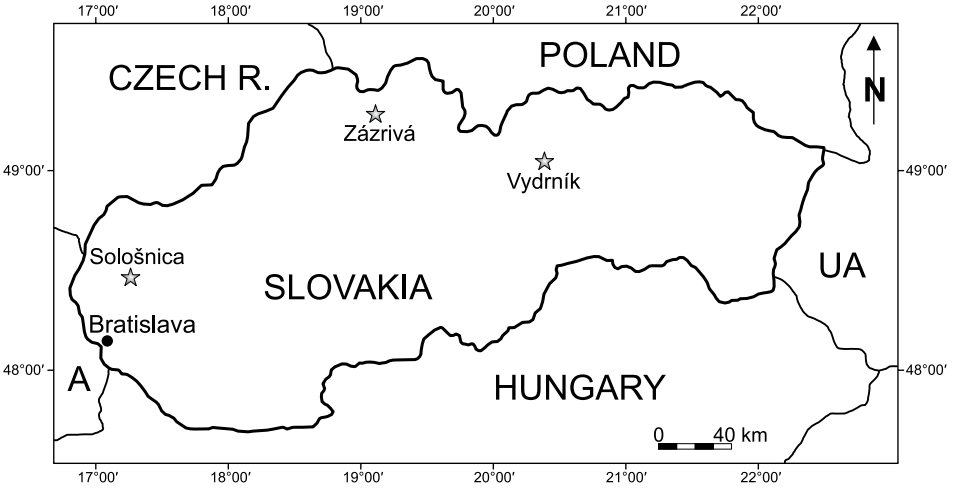

Fig. 1. Location of the three studied areas.

sets of detectors were changed after three months of exposure (spring, summer, autumn and winter period). Radon survey in Sološnica started in the spring monitoring period (March–May 2018). Due to technical reasons, radon monitoring in Vydrník and Zázrivá started later, in the summer period (June–August 2018).

In the monitored buildings, two or three detectors were placed, primarily in the rooms situated on the ground floor, where the inhabitants spend most of their time. Detectors were placed 15–20 cm from the walls, as far as possible from the windows, doors and heating bodies. Building characteristics as building material, window tightness, cellar, year of construction and reconstruction, number of inhabitants, intensity of ventilation and time spent in monitored rooms were obtained through a questionnaire, distributed to voluntary participants of the survey together with information leaflet about radon (*Műllerová et al., 2016*). Passive alpha track detector RamaRn (SÚJCHBO, Milín, Czech Republic), with Kodak LR 115 film located at the bottom of the diffusion chamber was used in this survey (*Thinová and Burian, 2008*).

The Sološnica village is situated on the border of two geomorphological provinces – the Malé Karpaty Mts. and the Záhorská nížina Lowland, at the contact of the Paleogene sediments of the Buková furrow and the Pan-

nonian sediments of the Vienna basin. Paleogene sediments (*Fordinál et al., 2012*) are represented by the Upper Eocene–Oligocene Zuberec Formation (Kyscellian Hrabník Formation *sensu Marko et al., 1990*) formed by the flysch-type sediments, which are folded and faulted. Lower Pleistocene–Holocene Quaternary formations are represented by proluvial-wetland sediments with organic admixture, loams with fragments of sandy pebbles in low alluvial fans and deluvial-fluvial sediments with sandy debris. According to the radon risk map elaborated by the State Geological Survey of Dionýz Štúr, Sološnica village belongs to the low and medium radon risk areas (*Gluch et al., 2009*). Buildings situated on the three profiles crossing assumed faults location were selected for indoor radon monitoring.

Vydrník village is located in the zone of the supposed map trace of E–W Vikartovce fault, rimming from the south uplifted and tilted block of the Kozie Chrbty Mts., composed of Mesozoic sequences of the Choč unit. Southward of the Vikartovce fault downthrown block of Hornád river occurs, with preserved Paleogene sediments (*Vojtko et al., 2011*). According to the radon risk map Vydrník is situated in the medium radon risk area (*Gluch et al., 2009*). The monitored buildings were situated on two profiles, one of them running parallel and one perpendicularly to the Vikartovce fault.

Zázrivá village is situated across the tectonic contact zone of the Pieniny klippen belt unit with both Outer and Inner Western Carpathians units (*Marko et al., 2005*). One part of the detectors was placed in the buildings at the vicinity of a supposed map trace of the neotectonically active E–W Kozinec fault inside the Pieniny klippen belt zone, in a high radon risk area (*Gluch et al., 2009*). Another part of the monitored buildings in Zázrivá was situated close to the southern tectonic contact of the Pieniny klippen belt zone with peri-Klippen Paleogene sediments, in the medium radon risk area.

3. Results and discussion

For the summer monitoring period the detectors were distributed to 225 rooms in 112 buildings (Table 1). In total, 218 detectors were collected (96.9%).

Most of the collected detectors (84.4%) were placed in the living room, kitchen, bedroom, child room and classroom (Table 2). During the summer

Table 1. Detectors distributed in the summer monitoring period (June–August 2018) and maximum of IRC.

Locality	houses (rooms)	max IRC (Bq/m^3)
Sološnica	66 (136)	405
Vydrník	22 (44)	370
Zázrivá	24 (45)	480
total	112 (225)	480

period IRC ranged from values under the detection limit of 55 Bq/m^3 to 480 Bq/m^3. A histogram of the frequency distribution for IRC in monitored rooms is depicted in Fig. 2. In 67% of rooms IRC was lower than the detection limit 55 Bq/m^3. Radon activity less than 200 Bq/m^3 was found in the majority of monitored rooms (94%). All monitored buildings were mechanically ventilated, by opened windows. Generally low IRC values in the summer period can be explained by intensive ventilation of investigated rooms in the summer season (*Papaefthymiou et al., 2003*).

Table 2. Building characteristics.

Type of a room	rooms (%)	Building material	rooms (%)
living room	66 (30.3)	aerated concrete (AC)	56 (25.7)
kitchen	54 (24.7)	brick	44 (20.2)
bedroom	45 (20.6)	slag block	24 (11.0)
child room	11 (5.0)	AC + brick	16 (7.3)
classroom	8 (3.7)	stone	14 (6.4)
office	4 (1.8)	no info	5 (2.3)
other	30 (13.8)	other	47 (21.6)

The preliminary results were examined in respect of five of the most used building materials (Table 2) and presence or absence of a cellar underneath the room. Increased IRC is often measured in room when it has direct contact with the subsoil. Radon from soil air can penetrate through the cracks in mat-slab foundations into the room, as a consequence of pressure difference between a building and the surrounding soil. A cellar can protect rooms from direct soil airflow (*Papaefthymiou et al., 2003; Borgoni et al., 2014; Műllerová et al., 2016*). However, unless they were well insulated,

cellars may also act as an entry point for radon into a building (*Buchli and Burkart, 1989*).

Almost 41% of the rooms monitored in the summer period were situated above a cellar. The distribution of IRC between rooms with and without a cellar underneath in Sološnica, Vydrník and Zázrivá is depicted in Fig. 3. During the summer monitoring period IRC higher than 300 Bq/m^3 was found only in the rooms with direct contact to the subsoil. IRC levels were

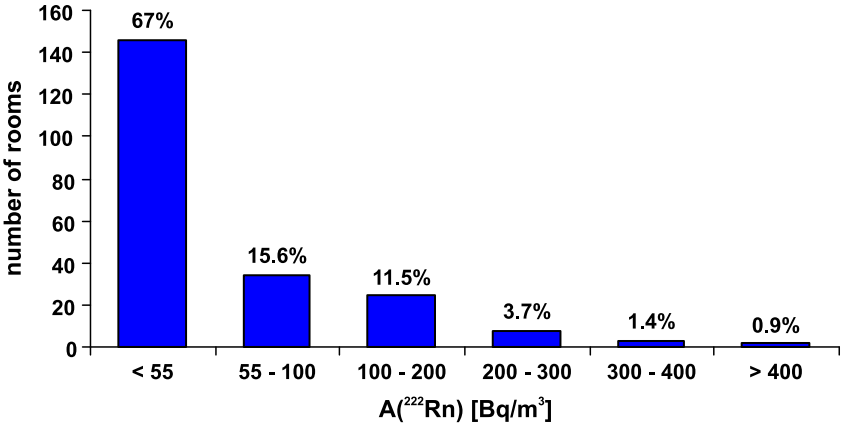

Fig. 2. The frequency distribution of IRC during the summer monitoring period (June–August 2018).

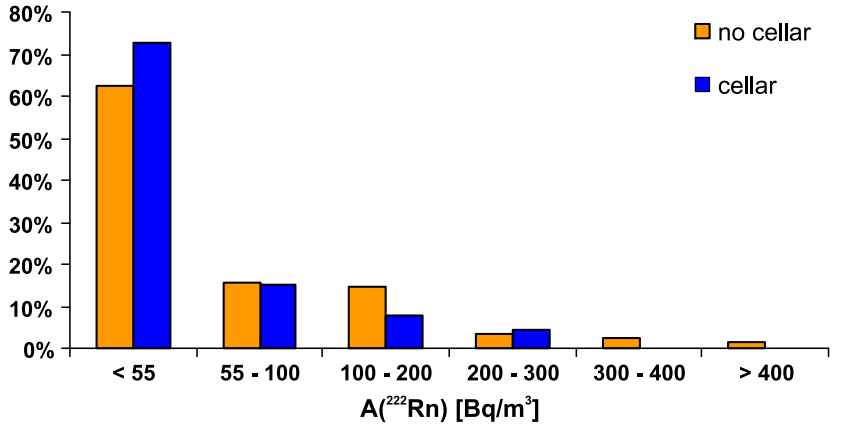

Fig. 3. The comparison of indoor ^{222}Rn concentration according to the contact of monitored room with the subsoil.

lower than the detection limit in 73% of the rooms situated above a cellar and in 62% of the rooms without a cellar. The results obtained in Sološnica for the spring period showed that in 58 % of the rooms situated above the cellar IRC was lower than the detection limit, while in rooms without a cellar only in 31% (*Smetanová et al., 2018*).

The most used building material differs among studied localities and the utilization of a specific material and the building methods are connected with the year of construction. While in Sološnica the major part of investigated buildings was built from aerated concrete (29%), slag blocks (14%) and brick (12%), in Zázrivá brick (28%) and aerated concrete (26%) prevailed and in Vydrník buildings constructed from bricks (41%) and stone (17%) dominated. However, also wood, adobe, concrete and various combinations of previously mentioned materials were used for the construction. Relatively new buildings constructed after year 1990 were made mainly of brick and aerated concrete, or their combination. Buildings constructed before 1960 were usually built from brick, stone and adobe.

According to the questionnaire (Table 2), the major part of the investigated buildings were constructed from aerated concrete, brick, slag blocks, local stone (limestone, travertine) or a combination of aerated concrete and brick. Among the above listed five materials, IRC higher than 300 Bq/m^3 was found in the building made of bricks. In all investigated buildings made of aerated concrete mixed with brick IRC was less than the detection limit (Fig. 4).

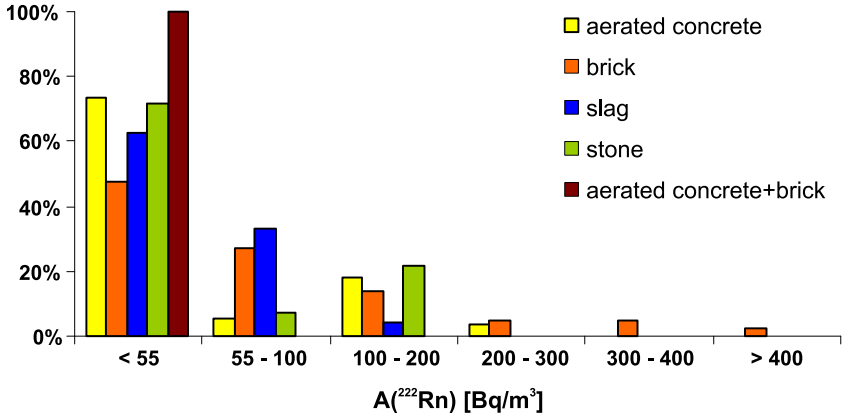

Fig. 4. The comparison of IRC according to the five the most used building materials.

In the summer monitoring period IRC exceeding 300 Bq/m^3 was found in all three monitored areas. The highest IRC in this monitoring period equal to (480±60) Bq/m^3 was measured in Zázrivá, in a relatively new house constructed in 2012, made of a combination of wood and aerated concrete. The house has no cellar under the monitored room. This house was built in a part of Zázrivá which is situated in the high radon risk area, however according to the questionnaire it was poorly ventilated, which probably caused an elevated IRC.

In all monitoring sites the indoor radon monitoring was performed in kindergartens (Sološnica, Zázrivá) or schools (Sološnica, Vydrník). Increased IRC measured in schools and kindergartens during the summer period can be connected with poor ventilation of rooms through the summer vacation, when the windows were closed for several weeks (*Műllerová et al., 2016*). Unfortunately, comparative data from the kindergarten in Zázrivá is missing, because both detectors were lost.

The highest IRC in Sološnica was detected in a kindergarten. The groundfloor building was constructed of brick in the seventies and thermally retrofitted in 2008 (replaced windows, thermal insulation) and has no cellar. Detectors were placed in all three classrooms. According to the questionnaire, the classrooms were intensively ventilated. In the summer monitoring period IRC equal to 285 Bq/m^3, 305 Bq/m^3 and 405 Bq/m^3 was found. However, the classroom with the highest IRC was closed for two months (from June to the end of August 2018) and the remaining two classrooms operated only until the last week of July 2018, so the results obtained during the summer monitoring period are not representative, they are strongly affected by a ventilation regime. Nevertheless, elevated IRC in comparison with the rest of the monitored buildings in Sološnica (Table 3) was confirmed in all classrooms also in the spring monitoring period (*Smetanová et al., 2018*).

Table 3. The comparison of indoor radon concentration measured in the kindergarten in Sološnica in the spring and summer monitoring periods.

A(^{222}Rn) (Bq/m^3)	classroom 1	classroom 2	classroom 3
spring (March–May)	315±55	365±35	280±50
summer (June–August)	285±50	305±50	405±55

In comparison with the kindergarten, IRC in the primary school in Sološnica was significantly lower, both in the spring and summer periods. A part of this building was made of brick in 1942, with a cellar under several classrooms. The new part built in 1992 from aerated concrete has no cellar. Three classrooms on the ground-floor were selected for the monitoring purposes. One of them was situated in the new part of the building. The remaining two monitored classrooms were in the older part, one of them was situated above the cellar. All classrooms were equipped with new plastic windows, but the building was not thermally insulated. During the summer vacation (July–August) the building maintenance work (painting) was performed and classrooms were intensively ventilated by opened windows. IRC equal to (70±25) Bq/m^3 or below the detection limit was found in the summer period. Similarly as in the kindergarten, the results obtained during the summer monitoring period are not representative, because of a different ventilation regime during the summer vacation. However, IRC in the classrooms was low also in the spring period, equal to (130±40) Bq/m^3 or was below the detection limit.

Another building in Sološnica with IRC exceeding 300 Bq/m^3 in the summer period was built in the 19-th century from a mixture of brick and local stone (limestone) and has no cellar under the both investigated rooms used as offices. The building was reconstructed in 2002 (replaced windows, thermal insulation). IRC in both rooms was higher than in the spring monitoring period (105±35) Bq/m^3 and (100±35) Bq/m^3, equal to (310±50) Bq/m^3 and (150±30) Bq/m^3 in the summer period, respectively.

In Vydrník IRC above 300 Bq/m^3 was registered in the house built from brick at the beginning of the 20-th century. While in the room above the cellar IRC was low (56±35) Bq/m^3, in the room with a direct contact with the subsoil it reached (370±55) Bq/m^3. According to the questionnaire, both monitored rooms were intensively ventilated.

IRC in the three monitored classrooms in the primary school in Vydrník reached (180±45) Bq/m^3, (225±50) Bq/m^3 and (250±50) Bq/m^3. The school was constructed in 1972 from brick and concrete. The lowest IRC was determined in the classroom on the basement. Two classrooms on the ground floor were both situated above a cellar. Classrooms are equipped with new plastic windows, but the building is not thermally insulated. The higher indoor radon levels than in the rest of monitored buildings can be explained

by poor ventilation of the classrooms during the summer vacation.

The preliminary results from the spring and summer monitoring period in Sološnica and summer monitoring period in Vydrník and Zázrivá did not satisfactorily prove the possible influence of assumed fault zones crossing monitored areas on IRC levels in monitored rooms. However, in some of the buildings, situated close to assumed fault lines (the kindergarten in Sološnica, the house with the highest IRC in Vydrník), significantly higher IRC was found in the comparison with the rest of monitored buildings in the studied area. The application of a wider complex of geophysical methods, together with the soil radon emanometry measurements in the vicinity of the buildings with elevated IRC, is necessary to show whether increased IRC is connected with fault zones or with the building characteristics or ventilation regime of monitored rooms.

4. Conclusion

In the summer monitoring period (June–August 2018) IRC was measured in 218 rooms of three localities Sološnica, Vydrník and Zázrivá situated on assumed fault zones. Possible influencing factors (cellar, building material) on IRC were analyzed. The majority of IRC in investigated rooms was below the detection limit of 55 Bq/m^3, probably as a result of intense ventilation of rooms in the summer months. However, IRC exceeding 300 Bq/m^3 was found in all monitored areas, in the rooms in direct contact with the subsoil. IRC below the detection limit was found in all buildings made of aerated concrete mixed with brick.

On the basis of the preliminary results from the spring and summer monitoring period in Sološnica and summer monitoring period in Vydrník and Zázrivá a possible relation between elevated indoor radon levels and position of a monitored building in relation to an assumed fault line was not sufficiently proven.

Acknowledgements. This work was supported by the Slovak Research and Development Agency of Ministry of Education, Science, Research and Sport of the Slovak Republic (project APVV-16-0146) and the Scientific Grant Agency of Ministry of Education, Science, Research and Sport of the Slovak Republic (VEGA project 2/0083/18).

References

Bonforte A., Cinzia F., Giammanco S., Guglielmino F., Liuzzo M., Neri M., 2013: Soil gases and SAR measurements reveal hidden faults on the sliding flank of Mt. Etna (Italy). J. Volcanol. Geotherm. Res., **251**, 27–40, doi: 10.1016/j.jvolgeores.2012.08.010.

Borgoni R., De Francesco D., De Bartolo D., Tzavidis N., 2014: Hierarchical modeling of indoor radon concentration: how much do geology and building factors matter? J. Environ. Radioact., **138**, 227–237, doi: 10.1016/j.jenvrad.2014.08.022.

Buchli R., Burkart W., 1989: Influence of subsoil geology and construction technique on indoor air 222Rn levels in 80 houses of the central Swiss Alps. Health Phys., **56**, 4, 423–429, doi: 10.1097/00004032-198904000-00003.

Burton M., Neri M., Condarelli D., 2004: High spatial resolution radon measurements reveal hidden active faults on Mt. Etna. Geophys. Res. Lett., **31**, 7, L07618, doi: 10.1029/2003GL019181.

Collignan B., Le Ponner E., Mandin C., 2016: Relationships between indoor radon concentrations, thermal retrofit and dwelling characteristics. J. Environ. Radioact. **165**, 124–130, doi: 10.1016/j.jenvrad.2016.09.013.

Drolet J.-P., Martel R., 2016: Distance to faults as a proxy for radon gas concentration in dwellings. J. Environ. Radioact. **152**, 8–15, doi: 10.1016/j.jenvrad.2015.10.023.

Fojtíková I., Navrátilová Rovenská K., 2015: Methodology for measurement in schools and kindergartes: experiences. Radiat. Prot. Dosim., **164**, 4, 612–617, doi: 10.1093/rpd/ncv340.

Font Ll., Baixeras C., Moreno V., Bach J., 2008: Soil radon levels across the Amer fault. Radiat. Meas., **43**, Suppl. 1, S319–S323, doi: 10.1016/j.radmeas.2008.04.072.

Fordinál K. (Ed.), Maglay J., Elečko M., Nagy A., Moravcová M., Vlačiky M., Kučera M., Polák M., Plašienka D., Filo I., Olšavský M., Buček S., Havrila M., Kohút M., Bezák V., Németh Z., 2012: Geological map of the Záhorská nížina Lowland (scale 1:50,000). State Geological Institute of Dionýz Štúr, Bratislava.

Gluch A., et al., 2009: Maps of natural radioactivity (Prehľadné mapy prírodnej rádioaktivity). State Geological Institute of Dionýz Štúr, Bratislava, available online at: http://apl.geology.sk/radio.

Marko F., Kováč M., Fodor L., Šútovská K., 1990: Deformations and kinematics of a Miocene shear zone in the northern Little Carpathians (Bukovská Furrow, Hrabník Formation) (Deformácia a kinematika miocénnej strižnej zóny severnej časti Malých Karpát (Bukovská brázda, hrabnícke súvrstvie)). Miner. Slovaca, **22**, 399–410 (in Slovak with English summary).

Marko F., Vojtko R., Plašienka D., Sliva Ľ., Jablonský J., Reichwalder P., Starek D., 2005: A contribution to the tectonics of the Periklippen zone near Zázrivá (Western Carpathians). Slovak Geol. Mag., **11**, 1, 37–43.

Mojzeš A., Marko F., Porubčanová B., Bartošová A., 2017: Radon measurements in an area of tectonic zone: A case study in Central Slovakia. J. Environ. Radioact., **166**, Part 2, 278–288, doi: 10.1016/j.jenvrad.2016.08.012.

Moreno V., Bach J., Zarroca M., Font Ll., Roqué C., Linares R., 2018: Characterization of radon levels in soil and groundwater in the North Maladeta Fault Area (Central Pyrenees) and their effects on indoor radon concentration in a thermal spa. J. Environ. Radioact., **189**, 1–13, doi: 10.1016/j.jenvrad.2018.03.001.

Műllerová M., Kozak K., Kovács T., Smetanová I., Csordás A., Grzadziel D., Holý K., Mazur J., Moravcsík A., Neznal M., Neznal M., 2016: Indoor radon survey in Visegrad countries. Appl. Radiat. Isot., **110**, 124–128, doi: 10.1016/j.apradiso.2016.01.010.

Neri M., Giammanco S., Ferrera E., Patanè G., Zanon V., 2011: Spatial distribution of soil radon as a tool to recognize active faulting on an active volcano: the example of Mt. Etna (Italy). J. Environ. Radioact., **102**, 9, 863–870, doi: 10.1016/j.jenvrad.2011.05.002.

Neri M., Giammanco S., Leonardi A., 2019: Preliminary Indoor Radon Measurements Near Faults Crossing Urban Areas of Mt. Etna Volcano (Italy). Front. Public Health, **7**, 105, doi: 10.3389/fpubh.2019.00105.

Papaefthymiou H., Mavroudis A., Kritidis P., 2003: Indoor radon levels and influencing factors in houses of Patras, Greece. J. Environ. Radioact., **66**, 3, 247–260, doi: 10.1016/S0265-931X(02)00110-8.

Smetanová I., Mojzeš A., Marko F., Fekete K., 2018: Indoor radon survey – preliminary results from Sološnica village, Slovakia. In: Barnet I., Neznal M., Pacherová P. (Ed.): Proc. 14th Int. Workshop on Geological Aspects of Radon Risk Mapping, Prague, September 17–21, 143–148, ISBN: 978-80-01-06493-1.

Thinová L., Burian I., 2008: Effective dose assessment for workers in caves in the Czech Republic: experiments with passive radon detectors. Radiat. Prot. Dosim., **130**, 1, 48–51, doi: 10.1093/rpd/ncn118.

Vičanová M., 2003: Utilisation of solid state nuclear track detectors in the solution of radon problems (Využitie detektorov stôp v pevnej fáze pri riešení radónovej problematiky). Ph.D. Thesis, Faculty of Mathematics, Physics and Informatics, Comenius University of Bratislava, 82 p. (in Slovak).

Vojtko R., Marko F., Preusser F., Madarás J., Kováčová M., 2011: Late Quarternary fault activity in the Western Carpathians: Evidence from the Vikartovce fault (Slovakia). Geol. Carpath., **62**, 6, 563–574, doi: 10.2478/v10096-011-0040-9.

WHO, 2009: Handbook on Indoor Radon: A Public Health Perspective. World Health Organization, ISBN: 978-92-4-154767-3, 95 p.

sciendo

Contributions to Geophysics and Geodesy Vol. 49/4, 2019 (403–424)

Monitoring changes of the Antarctic Ice sheet by GRACE, ICESat and GNSS

Fang ZOU, Robert TENZER*, Samurdhika RATHNAYAKE

Department of Land Surveying and Geo-Informatics, Hong Kong Polytechnic University, 181 Chatham Road South, Kowloon, Hong Kong

Abstract: In this study, we estimate the ice mass changes, the ice elevation changes and the vertical displacements in Antarctica based on analysis of multi-geodetic datasets that involve the satellite gravimetry (GRACE), the satellite altimetry (ICESat) and the global navigation satellite systems (GNSS). According to our estimates, the total mass change of the Antarctic ice sheet from GRACE data is −162.91 Gt/yr over the investigated period between April 2002 and June 2017. This value was obtained after applying the GIA correction of −98.12 Gt/yr derived from the ICE-5G model of the glacial isostatic adjustment. A more detailed analysis of mass balance changes for three individual drainage regions in Antarctica reveal that the mass loss of the West Antarctic ice sheet was at a rate of −143.11 Gt/yr. The mass loss of the Antarctic Peninsula ice sheet was at a rate of −24.31 Gt/yr. The mass of the East Antarctic ice sheet increased at a rate of 5.29 Gt/yr during the investigated period. When integrated over the entire Antarctic ice sheet, average rates of ice elevation changes over the period from March 2003 to October 2009 derived from ICESat data represent the loss of total ice volume of $-155.6\,\mathrm{km}^3$. The most prominent features in ice volume changes in Antarctica are characterized by a strong dynamic thinning and ice mass loss in the Amundsen Sea Embayment that is part of the West Antarctic ice sheet. In contrast, coastal regions between Dronning Maud Land and Enderby Land exhibit a minor ice increase, while a minor ice mass loss is observed in Wilkes Land. The vertical load displacement rates estimated from GRACE and GPS data relatively closely agree with the GIA model derived based on the ice-load history and the viscosity profile. For most sites, the GRACE signal appears to be in phase and has the same amplitude as that obtained from the GPS vertical motions while other sites exhibit some substantial differences possibly attributed to thermo-elastic deformations associated with surface temperature.

Key words: Antarctica, ice sheet, glacier, GRACE, ICESat

1. Introduction

The Antarctic ice sheets, the world's largest single mass of ice, cover an area of 14×10^6 km^2. The knowledge and understanding of the mass balance of

*corresponding author: phone: +852 2766-5592; email: robert.tenzer@polyu.edu.hk

doi: 10.2478/congeo-2019-0021

this vaste ice volume play a key role in studies of global sea level change and global water cycle (e.g. *Tang et al., 2012; Shepherd and Wingham, 2007;* or *Jacob et al., 2012*). Antarctic glaciers also provide important information about the past and present climate that could help understanding the impact of future climate change (e.g. *Zammit-Mangion et al., 2015; Van Wessem et al., 2014;* or *Hanna et al., 2013*).

The mass balance of the Antarctic ice sheet has long been a controversial topic, because of difficulties in estimating it accurately. This is evident from Table 1, where we summarized estimates of the total mass balance of the Antarctic ice sheet from selected studies. As seen, the results from different or even the same techniques (i.e. satellite-radar altimetry, satellite gravity, or Synthetic Aperture Radar) differ significantly. The results from the satellite radar altimetry, such as ICESat, suggest a mass rate for the whole continent in the range from -89 to -103 Gt/yr for the period 2003–2007. Spatial variations in snow, firn ice and ice densities and thickness have a significant impact on the final mass change estimates. Consequently, it makes it difficult to assess realistically uncertainties of the ICESat estimates. Results from the Interferometric Synthetic Aperture Radar (InSAR) indicate that over the last decade, the glacial mass discharge exceeds model predictions of the snow accumulation. Based on the analysis of ERS-1 and ERS-2 data, *Zwally et al. (2005)* suggested that the mass loss of the Antarctic ice sheet was at a rate of -31 ± 12 Gt/yr within the period from 1992 to 2002. The estimates of Antarctic ice/snow mass changes from monitoring the ice elevation changes (based on radar altimetry and radar scatter meter) are limited by spatial and temporal coverage and by uncertainties in snow and firn ice density and thickness. Estimates of mass changes of the Antarctic ice sheet from the Gravity Recovery And Climate Experiment (GRACE) range from -60 up to about -190 Gt/yr (cf. Table 1). These large discrepancies in published results are mainly due to different methods used to convert the monthly gravity field solutions (expressed as spherical harmonics, i.e. Level-2 GRACE data) into surface mass changes. Major reasons are related to processing GRACE data from different data centres, using different processing methods that involve filtering techniques, treatments of low-degree terms and the leakage of GRACE signals between different mass bodies. Important aspect is also due to uncertainties associated with other geophysical signals in GRACE data, particularly to mention the Glacial

Isostatic Adjustment (GIA). Naturally, differences in published results are also due to processing of GRACE data over different time-periods. *Velicogna and Wahr (2006)*, for instance, estimated that over the first three years of GRACE data availability between April 2002 and August 2005, the total mass loss of the Antarctic ice sheet was at a rate of −152±80 Gt/yr (while accounting for the GIA correction of 192±79 Gt/yr). This ice mass loss is equivalent to a global sea level rise at a rate of 0.4±0.2 mm/yr. *Chen et al. (2009)*, based on the analysis of GRACE RL04 data products, estimated the total mass loss of the Antarctic ice sheet at a rate of −190±77 Gt/yr during the period between April 2002 and January 2009. *Ivins et al. (2013)* demonstrated that uncertainties in GIA largely affect estimates of the total

Table 1. Major studies of the total mass balance of the Antarctic ice sheet.

Study	Data	Time span	Filtering	GIA model	Leakage effect	Rate [Gt/yr]	Acceleration [Gt/yr^2]
Zwally et al. (2005)	ERS	1992–2002				−31±12	
Velicogna et al. (2006)	GRACE RL04	2002.4–2005.8		ICE5G 192±79 Gt/y	GLDAS	152±80	
Chen et al. (2006)	GRACE RL04	2002.04–2005.11	800 km Gausian	No GIA correction	Numerical Simulation IJ05	−31±12	
Gunter et al. (2009)	GRACE RL04	2003.02–2007.02	Kaula regularization, P3M7 and 400 km Gaussian	ICE5G 149 Gt/y	*Klees et al. (2008)*	−91 to −102	
	ICESat	2003.02–2007.02		IJ05 107 Gt/y		−89 to −103	
Chen et al. (2009)	GRACE RL04	2002.04–2009.01	P4M6 and 300 km Gaussian	IJ05	forward modelling	−190±77	
Velicogna (2009)	CSR	2002.04–2009.02	a specific factor	176±76 Gt/y	*Wahr et al. (2006)*	−246	−26±14
Jacob et al. (2012)	CSR RL05	2003.01–2010.12	averaging kernel	ICE5G	N	−165±72	
Chen et al. (2009)	GRACE RL04	2002.04–2009.01	P4M6 and 300 km Gaussian	IJ05	forward modelling	−190±77	
Ivins et al. (2013)	GRACE RL05	2003.02–2013.06	3° Gaussian smoothing operator	ICE5G		−171±22	−12±7
				IJ05 R2		−93±29	−12±7
				W12a		−91±23	−12±7
Velicogna et al. (2014)	GRACE RL05	2003.01–2013.12	250 km Gaussian	*Ivins et al. (2013)* and ICEG5G	*Velicogna and Wahr (2013)*	−67±44	−11±4
This study	GRACE CSR RL06	2002.04–2017.06	P4M6 and 500 km Gaussian	ICE5G	forward method	−162.91±5.09	−10.12±4.3

mass balance in Antarctica. For the investigated period between February 2003 and June 2013, they reported rates of the mass loss from −91 to −171 Gt/yr. In more recent study, *Velicogna et al. (2014)* estimated that over the period between January 2003 and December 2013 the mass loss was at a rate of only −67±44 Gt/yr.

In this study, we estimated the total mass changes over the entire continent of Antarctica using GRACE data. We also provided individual estimates for three major Antarctic regions, involving the East and West Antarctica and the Antarctic Peninsula. We estimated ice elevations and their changes based on the analysis of ICESat data. We then compared results obtained from GRACE and ICESat data, focusing on secular trends observed in the ice elevation and mass variability. These secular trends were validated using vertical displacements from the continuous GPS stations installed in Antarctica.

2. Data acquisition

In this section, we briefly describe datasets and models used to estimate changes of the total mass budget in Antarctica.

2.1. Study area

Applying a commonly adopted geographical description of Antarctica, we investigated the mass balance for the whole continent as well as for three distinctive regions (see Fig. 1). West and East Antarctica are separated by the Transantarctic Mountains spreading between the Ross Sea and the Weddell Sea. West Antarctica is covered by the West Antarctic ice sheet. The ice sheet has been of recent concern because of a possibility of its collapse. East Antarctica lies on the Indian Ocean side of the Transantarctic Mountains. Only small portion of East Antarctica is part of the western hemisphere. East Antarctica is largely covered by the East Antarctic ice sheet. The Antarctic Peninsula is part of a larger peninsula of West Antarctica. The Antarctic Peninsula consists of a string of bedrock islands beneath the ice sheet, which cover it. Floating ice shelves whose mass GRACE does not measure are not discussed in this paper.

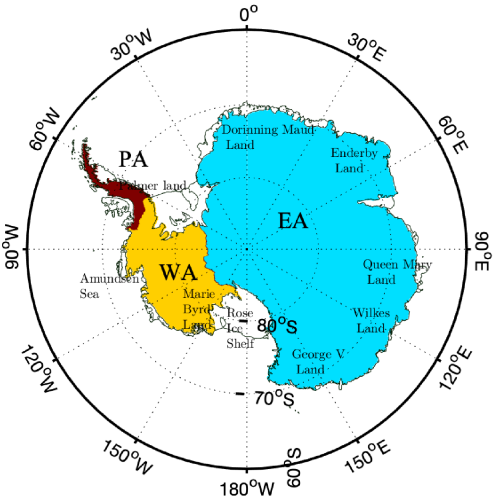

Fig. 1. The Antarctic drainage system, comprising the West Antarctic (WA) ice sheet, the East Antarctic (EA) ice sheet, and the Antarctic Peninsula (PA) ice sheet.

2.2. GRACE data

We used the GRACE RL06 monthly solutions prepared by the Center for Space Research at the University of Texas at Austin over the period from April 2002 to June 2017. The GRACE monthly solutions are provided with the spectral resolution up to degree of 60. The first-degree spherical harmonic coefficients that could not directly be detected by GRACE were determined from combining GRACE data with numerical ocean models. The second-zonal spherical harmonic coefficient C_{20} (due to Earth's flattening) was determined from the analysis of the Satellite Laser Ranging measurements. The P4M6 decorrelation filter was applied for destripping. The Gaussian filter (with a radius of 500 km) was applied to minimize spatial noise in GRACE monthly solutions. We note that monthly variations were taken with respect to the average value over the entire period (from April 2002 to June 2017).

2.3. ICESat data

We used the ICESat/GLAS Level 2 altimetry product (GLA14) that includes the global land surface elevation data, the footprint centroid ge-

olocation, the laser reflectance, the geoid, the instrument gain, the waveform saturation and many other relevant parameters. The ICESat/GLA14 Release-34 elevation data crossing Antarctica over the period from March 2003 to October 2009 were obtained through the National Snow and Ice Data Center (NSIDC). The ICESat ground tracks over this period are illustrated in Fig. 2.

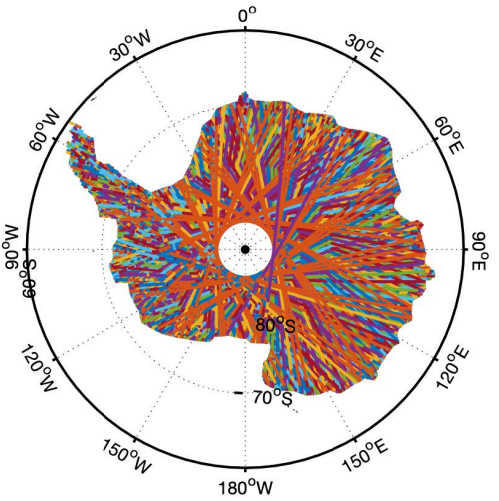

Fig. 2. The ICESat ground tracks in Antarctica over the period from March 2003 to October 2009.

2.4. Glacial isostatic adjustment

GIA models depend on the hypotheses on the ice-load history and the viscosity profile. In this study, we adopted the recent GIA model to correct for secular mass changes derived from GRACE data based on the ICE5G ice-load history, the VM2 viscosity profile and the same PREM elastic structure (*A et al., 2013*).

3. Method

Data and models described in the preceding section were used to estimate changes in total mass balance and elevations of the Antarctic ice sheet according to methods briefly recapitulated next.

3.1. Water storage change from GRACE

The monthly GRACE solutions consist of the (fully-normalized) spherical harmonic coefficients ΔC_{nm} and ΔS_{nm} of degree n and order m. The terrestrial water storage anomalies $\Delta\eta$ over the land were computed directly from these coefficients for a particular time period t (typically choosing a monthly period) according to the following expression (e.g. *Wahr et al., 1998*):

$$\Delta\eta(\theta,\lambda,t) = \frac{R\rho}{3\rho_w}\sum_{n=0}^{\infty}\sum_{m=0}^{n}\frac{2n+1}{(1+k_n')}W_n\tilde{P}_{nm}(\cos\theta)\times \\ \times\left(\Delta\hat{C}_{nm}(t)\cos m\lambda + \Delta\hat{S}_{nm}(t)\sin m\lambda\right), \tag{1}$$

where ρ is Earth's mean density, ρ_w is the freshwater density, R is Earth's equatorial radius, $\tilde{P}_{nm}(\cos\theta)$ represents the (fully-normalized) Legendre associated function of degree n and order m, $k_n^{'}$ represents the (degree-dependent) Love number, $n = 60$ is a maximum degree of spherical harmonics, and W_n is the (degree-dependent) kernel function of a Gaussian filter. The horizontal position in Eq. (1) and thereafter is described by the spherical co-latitude θ and longitude λ.

GRACE data has a limited spatial resolution. Moreover, the GRACE monthly solutions are spatially filtered in order to reduce the noise. Therefore, a leakage effect suppresses the actual gravitational signal attributed to ice sheet mass variations. This effect causes inaccurate results, particularly in land-ocean areas. It significantly attenuates amplitudes and biases of mass balance estimates in Antarctica. We applied forward modelling technique to estimate monthly solutions of the GRACE mass variations in order to mitigate the ocean-land signal leakage.

By taking into consideration annual and semi-annual signals, the long-term change rate was estimated by applying an ordinary least-square fit at each grid point. This numerical procedure is described by means of secular and seasonal trends of monthly mass anomalies in the following form:

$$M(\theta,\lambda) = a_1 + a_2\,(t-t_0) + a_3\sin\left[w_1(t-t_0)+\varphi_1\right] + \\ + a_4\sin\left[w_2(t-t_0)+\varphi_2\right] + \varepsilon\,, \tag{2}$$

where M is the surface mass anomaly specified at a location (θ,λ), t_0 is an initial epoch (in this study August 2002), a_2 is a linear rate of mass

changes at a grid point (θ, λ), a_3 and a_4 are amplitudes of annual w_1 and semi-annual w_2 frequencies, respectively, φ_1 and φ_2 are phases, and ε is the noise. The surface mass anomaly described by a functional model in Eq. (2) comprises the GIA secular trend and the secular as well as seasonal trends in mass balance variations.

To estimate the surface displacement due to the mass load effect, we used the CSR de-aliasing Level-1B (AOD1B) solution (GAC products) and the monthly Stokes' coefficients GSM (GRACE satellite only model) to compute the whole surface vertical loads, including the hydrological, atmospheric and non-tidal ocean loads. The vertical displacement dr due to the changing mass load is defined in terms of spherical harmonic coefficients for gravity field from GRACE (including GSM and GAC productions). It reads (*Farrell, 1972*):

$$\mathrm{d}r(\theta,\lambda) = R\sum_{n=0}^{\infty}\sum_{m=0}^{n}\frac{h_n^{'}}{(1+k_n^{'})}\tilde{P}_{nm}(\cos\theta)\times \\ \times\left(\Delta\hat{C}_{nm}(t)\cos m\lambda + \Delta\hat{S}_{nm}(t)\sin m\lambda\right), \tag{3}$$

where $h_n^{'}$ and $k_n^{'}$ are the (degree-dependent) Love numbers.

3.2. Elevation changes from ICESat

The GLA14 data release is provided with control indicators and corrections to illustrate data acquisition and to correct elevation data. In order to ensure data accuracy and to improve data quality, we selected the ICESat elevation data based on checking a quality index and applying a number of necessary corrections (such as the saturation elevation correction).

We used planes fitted to the repeated-tracks method to measure elevation changes. Firstly, we applied least-square regression technique that fits rectangular planes to segments of the repeated-track ICESat data. Along each reference track, multi-temporal ICESat points were assigned to 700 m long planes, with overlaps of 350 m. The width of planes depends on the maximum cross-track separation distance between repeated profiles, typically a few hundred meters. The plane equation describes the change of plane elevation and gradient in different periods as follows:

$$h(t,x,y) = S_e(x-x_0) + S_n(y-y_0) + \mathrm{d}h/\mathrm{d}t\, v(t-t_0) + h_0\,, \tag{4}$$

where x and y are coordinates and t is the observation time of each observation point on a plane; h is the elevation of each observation point on the plane; x_0 and y_0 are coordinates of a central reference point on a plane; h_0 is the elevation of a central reference point on a plane; and t_0 is a reference time.

For each plane, the east and north slopes S_e and S_n including the constant elevation change rate $\mathrm{d}h/\mathrm{d}t$ were estimated by solving the following system of observation equations:

$$\begin{bmatrix} \mathrm{d}h_1 \\ \mathrm{d}h_2 \\ \vdots \\ \mathrm{d}h_n \end{bmatrix} = \begin{bmatrix} \mathrm{d}x_1 & \mathrm{d}y_1 & \mathrm{d}t_1 \\ \mathrm{d}x_2 & \mathrm{d}y_2 & \mathrm{d}t_2 \\ \vdots & \vdots & \vdots \\ \mathrm{d}x_n & \mathrm{d}y_n & \mathrm{d}t_n \end{bmatrix} \begin{bmatrix} S_e \\ S_n \\ \mathrm{d}h/\mathrm{d}t \end{bmatrix} + \begin{bmatrix} r_1 \\ r_2 \\ \vdots \\ r_n \end{bmatrix}, \tag{5}$$

where $\mathrm{d}x$, $\mathrm{d}y$, $\mathrm{d}h$ and $\mathrm{d}t$ are, respectively, differences in the 3-D position (x,y,h) and time t (in decimal years) between each point and the average of all points on a plane. The residuals r of a plane regression contain remaining elevation variations, which cannot be attributed to an assumption of planar slopes and an invariable elevation change rate. To avoid gross errors in $\mathrm{d}h/\mathrm{d}t$ due to cloud-affected signals or a small-scale topography, we removed potential outlier points if $r > 5\,\mathrm{m}$ and recomputed the regression iteratively until all residuals were below this threshold. We removed all planes with a shorter observational time span than two years and planes that consisted of less than four repeated tracks or less than 10 points. It is also noted that we used filter to make sure that each plane coincided with the same season (such as winter-to-winter) to reduce the impact of seasonal bias.

4. Results and analysis

Methods recapitulated in Section 3 were applied to estimate changes in total mass budget of the Antarctic ice sheet from GRACE data after applying the GIA correction. We also used ICESat data to estimate elevation changes of the Antarctic ice sheet. The results are presented in this section.

4.1. Mass changes from GRACE

Without considering uncertainties, the time series of ice sheet mass changes

estimated from GRACE data include the long-term (secular), seasonal and inter-annual signals. The long-term signal mainly reflects the trend of mass changes of the ice sheet over the period of cyclical fluctuations exceeding more than 10 years. The long-term signal is used to evaluate the state of ice sheet mass balance. Seasonal signals are seasonal or short-term fluctuations in the mass change of ice sheets caused by seasonal factors such as Earth's revolution around the Sun. The seasonal signals are dominated by annual and semi-annual changes. The inter-annual signal is the mass change signal whose spectrum is between the seasonal and long-term signals, which is often greater than 1 year and less than 10 years. It mainly reflects variations in the ice sheet mass during the years. Taking into account seasonal and inter-annual changes, we derived the long-term changes of the Antarctic ice sheet mass from GRACE data. Results are presented in Fig. 3.

Maps of secular mass change rate indicate that the West Antarctic ice sheet and Antarctica Peninsula experienced a significant ice loss over the fifteen-year period. Coastal areas in the East Antarctic ice sheet (30°W∼65°E), on the other hand, experienced a slight mass accumulation. As seen in Fig. 3, the leakage effect attenuates the amplitude of mass change signal, especially in areas where the significant mass loss occurred. Before the leakage effect correction, the mass loss of Marie Byrd Land, which is part of the West Antarctic ice sheet, was the fastest reaching -5 to -10 cm/yr (cf. Fig. 3a). After applying the leakage correction, the mass loss there was estimated to be at a rate up to -20 cm/yr. We see that after applying this correction, most of the mass change signal in Antarctica was restored. The mass loss rate of the West Antarctic and Antarctic Peninsula ice sheets increased significantly. We also see that the mass change along coastal areas of the East Antarctic ice sheet (like Queen Maud Land) increased. The central part of the East Antarctic ice sheet does not exhibit significant mass changes over the period from April 2002 and June 2017. Coastal regions between Dronning Maud Land and Enderby Land (20°W–60°E) exhibited a minor mass gain, while a slight mass loss was detected between Wilkes Land and Victoria Land (110°E–160°E). The Antarctic ice sheet gained mass through snowfall, while lost mass at its margins through submarine melting and iceberg calving. These losses occurred primarily within ice shelves and floating ice sheet. Almost the entire ice sheet in West Antarctica experienced a clear mass loss over the investigated period. The negative mass-change pattern

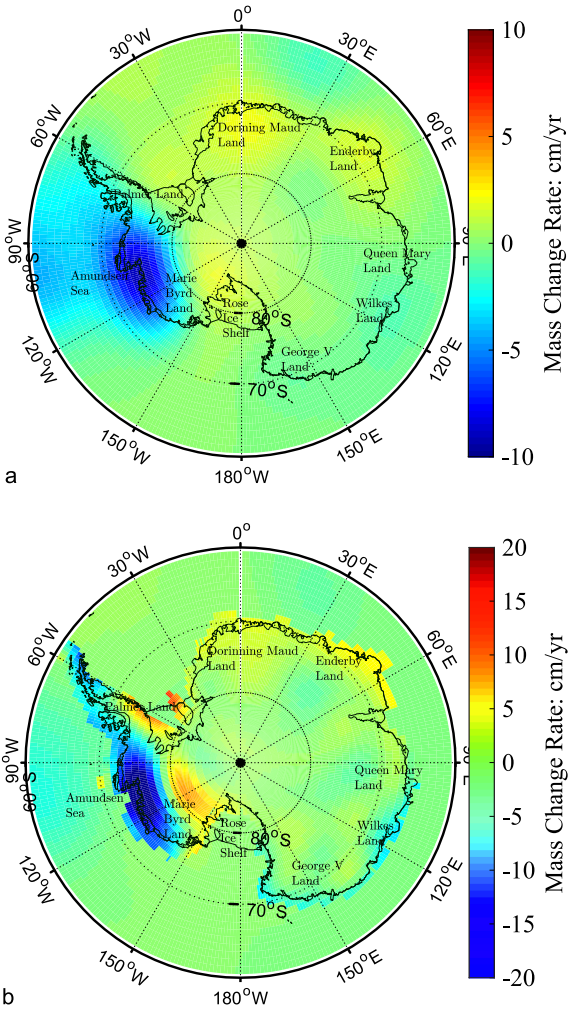

Fig. 3. The average annual rates (mm/yr) of equivalent water thickness between April 2002 and June 2017 derived from: (a) processing the GRACE monthly solutions, and (b) the forward modeling reconstructed estimate. The GIA effect was corrected for according to *A et al. (2013)*.

spreads from the tip of the Antarctic Peninsula up to the coast of Marie Byrd Land. The most rapid decrease of the Antarctic ice sheet occurred along the coast of the Amundsen Sea with substantial thinning of adjoining ice shelves and along the Antarctic Peninsula after ice-shelf disintegration

events. The estimated rate after correcting for the leakage effect has a consistent trend and seasonal periodic variation with the estimated rate directly from GRACE data. The results are plotted in Fig. 4. Both solutions shown in Fig. 3 exhibit a secular rate of decreasing mass changes (between April 2002 and June 2017). According to a reconstructed trend (obtained after applying the forward modelling), the total ice/snow budget over this period decreased at a rate of -162.91 ± 5.09 Gt/yr, attributing to the global sea level rise by 0.45 mm/yr. The GIA effect of -98.12 Gt/yr was taken from *A et al. (2013)*. A downtrend estimated directly from GRACE data (without applying the forward modelling) was at a rate of -137.87 ± 4.42 Gt/yr. The time series of the Antarctic ice sheet change shows a clear seasonal signal that is superimposed over a linear trend (cf. Fig. 4).

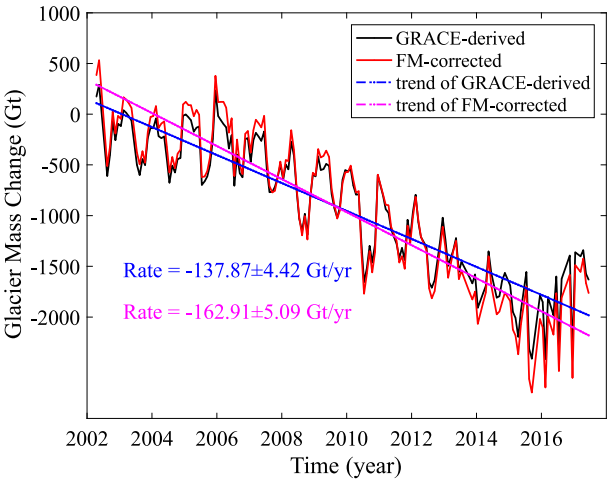

Fig. 4. Time series of mass variations of the Antarctic ice sheet between April 2002 and June 2017. Black lines represent direct estimates from GRACE monthly solutions, and red lines show reconstructed mass variations by using the forward modelling technique. Blue-dotted lines present a linear rate of direct GRACE estimates, and red-dotted lines show a linear rate of reconstructed mass variations. The GIA effect was corrected for according to *A et al. (2013)*.

Mass changes on the Antarctic ice sheet exhibited significant spatial heterogeneities (Fig. 3) that reflect a unique topography and climatic conditions of its different regions. To illustrate this, we plotted mass variations individually for each drainage area (Fig. 5). For the Antarctic ice sheet, the

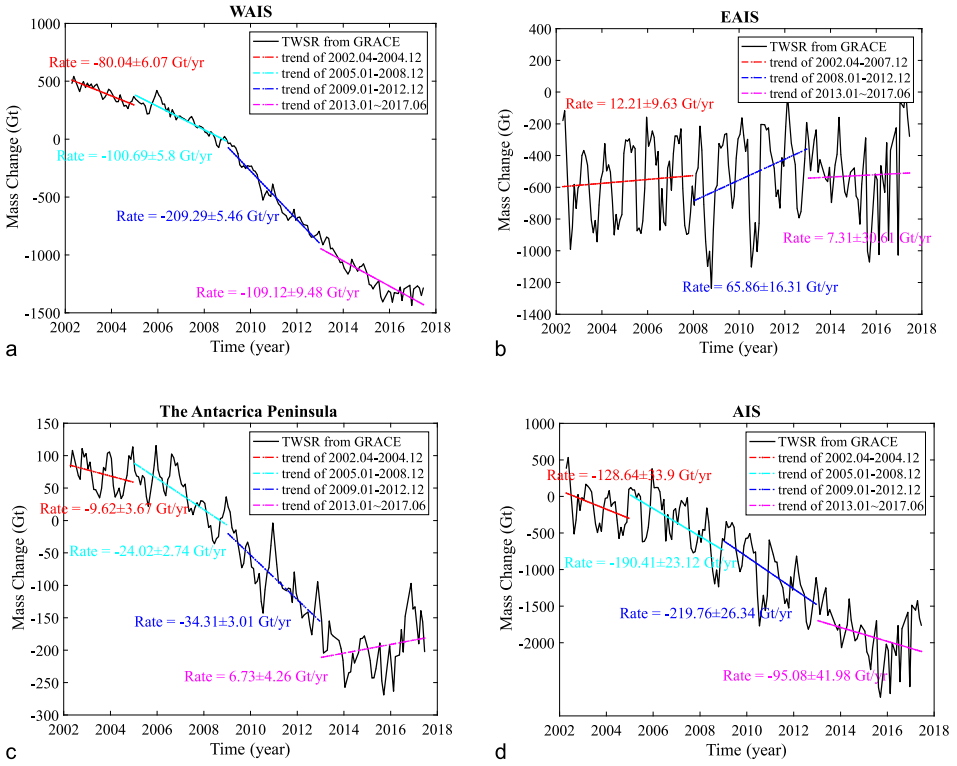

Fig. 5. The time series of total mass balance of: (a) the West Antarctic ice sheet, (b) the East Antarctic ice sheet, (c) the Antarctic Peninsula ice sheet, and (d) the whole Antarctic ice sheet. The GIA effect was corrected for according to *A et al. (2013)*.

time series during the whole investigated period was separated into four distinctive events. The first period between March 2003 and December 2004 is characterized by the mass loss at a rate of −128.64 Gt/yr. After 2005, the mass loss reached a rate of −190.41 Gt/yr, and further accelerated after January 2009 until December 2012 at a rate up to −219.76 Gt/yr. After January 2013 until June 2017, the mass loss was at a rate of −95.08 Gt/yr

Compared to temporal changes of the total mass volume of the Antarctic ice sheet, we see quite different patterns for individual drainage areas. The West Antarctic ice sheet is characterized by mass loss over the whole investigated period. The fastest mass loss at a rate of 209.29 Gt/yr occurred between January 2009 and December 2012. Prior to January 2009,

the detected mass loss was clearly lower. After January 2013, the mass loss again slowed down in the West Antarctica. Most of this mass loss happen in the Amundsen Sea region. These results are consistent with findings by *Dutrieux et al. (2014)*. They detected a significant drop in seawater temperature of the Amundsen Sea between 2012 and 2013. Our results are also highly consistent with observations made by *Mouginot et al. (2014)* using InSAR data. We see a similar decreasing trend for the Antarctic Peninsula ice sheet, except for the last period from January 2013 until June 2017 when we observe a slight mass increase at a rate of 6.73 Gt/yr. In contrast, the mass balance of the East Antarctic ice sheet is relatively stable with only a minor increase, except for the period of a relatively fast mass increase between January 2008 and December 2012 at a rate of 65.86 Gt/yr. Two exceptionally large accumulation events took place in Dronning Maud Land in 2009 and 2011 (*Boening et al., 2012; Lenaerts et al., 2013*).

4.2. Elevation changes from ICESat

In Fig. 6, we present the first maps of ice elevations and its changes for the entire Antarctic ice sheet derived from ICESat data acquired during the period from March 2003 to October 2009. We used in total 200 million areas in Antarctica to derive the elevation change map that successfully reproduced large-scale patterns of ice sheet changes. The most prominent changes in ice elevations are associated with a strong dynamical thinning in the Amundsen Sea Embayment. This phenomenon has been confirmed to be caused by the rapid flow of glaciers and their tributaries. Crosson and Dotson ice shelves, situated near the Amundsen Sea, have been infused by many small independent glaciers that also experienced a dynamic thinning explained by ocean currents (cf. *Pritchard et al., 2009*). A dynamic thinning was also observed at Totten Glacier (that is part of the East Antarctic ice sheet) and some large glaciers along the Antarctic Peninsula. In Dronning Maud Land (in East Antarctica), on the other hand, we detected an extended area of dynamic thickening of up to 0.30 m/yr. The dynamic thickening was detected also inland but at lower rates approximately within 0.1 to 0.2 m/yr. Most of central part of the East Antarctic ice sheet is nearly stable, without exhibiting any significant changes in ice elevations. This finding agrees with our results of mass changes obtained from processing GRACE data.

The largest decrease in ice elevations was inferred over the terminus of Smith Glacier (part of the West Antarctic ice sheet) with a maximum surface lowering at a rate of −6.4 m/yr. Another large decrease was found over the Wilkes Land (part of the East Antarctic ice sheet) at a rate of −0.8 m/yr. Elsewhere in East Antarctica, we detected a clear growth of the ice sheet near the Enderby Land, Ellsworth Land and Macrobertson Land (near the Amer Ice sheet) that is likely attributed to ocean currents.

We see apparent similarities between spatial patterns of the total mass changes from GRACE (Fig. 3b) and elevation changes from ICESat (Fig. 6b). Both, GRACE and ICESat results revealed the largest mass and elevation changes in the Amundsen Sea region. When integrated over whole Antarctica, the average elevation changes derived from the ICESat (after applying also the GIA correction) correspond to a total loss of ice volume of $-155.6\,\mathrm{km}^3$ (between March 2003 and October 2009). Most of this mass loss ($-139.7\,\mathrm{km}^3$) happened in West Antarctica, while much less ($-37.1\,\mathrm{km}^3$) in the Antarctic Peninsula. East Antarctica exhibited a slight mass increase ($21.2\,\mathrm{km}^3$).

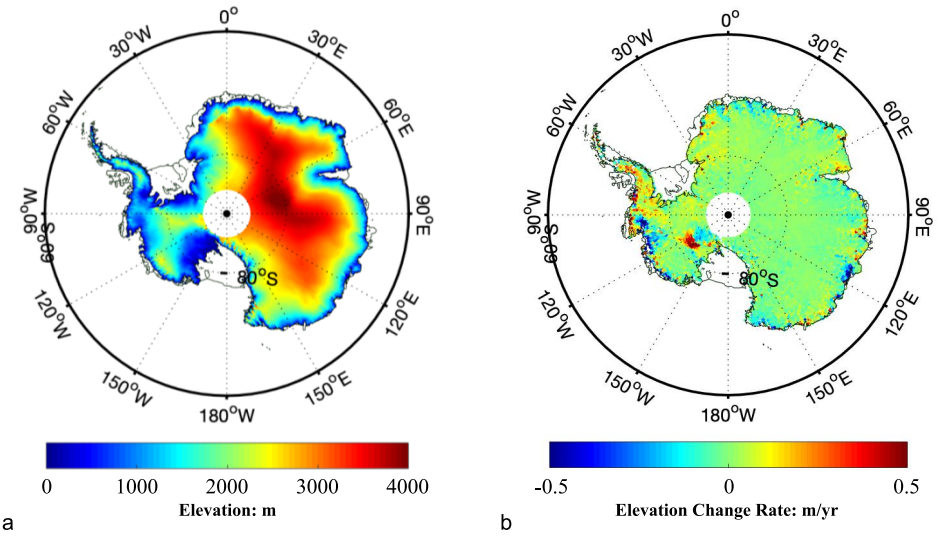

Fig. 6. Maps of: (a) the ice elevation (m) and (b) its changes (m/yr) in Antarctica over the period from March 2003 to October 2009 derived from ICESat data.

4.3. Displacement from GNSS and GRACE

The vertical displacement rates at 44 Antarctic GNSS stations over the period from 1992 to 2018 provided by the Jet Propulsion Laboratory (`https://sideshow.jpl.nasa.gov/post/series.html`) are shown in Fig. 7. In Fig. 8, we plotted the vertrical displacements obained from GRACE data

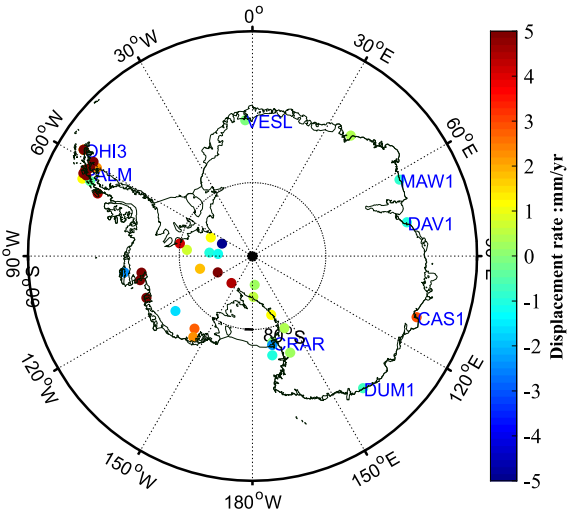

Fig. 7. The vertical displacement rates at 44 GNSS stations in Antrarctica over the period from 1992 to 2018.

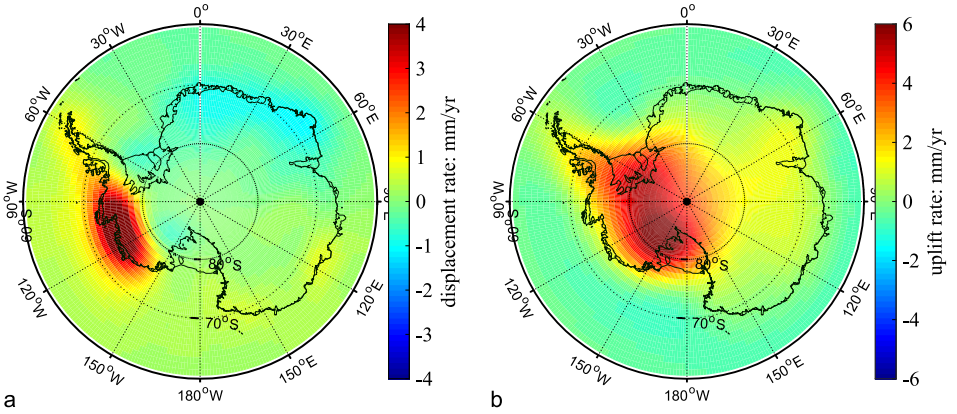

Fig. 8. The vertical displacement rates in Antactica from: (a) GRACE, and (b) GIA model (*A et al., 2013*).

and accoding to GIA model (*A et al., 2013*). We note that all these GNSS stations are stabilized to the bedrock. We see a relatively good spatial consistency between the vertical displacement rates from GRACE (Fig. 8a) and GNSS observations (Fig. 7) when compared with the vertical load displacement rates from the GIA model (*A et al., 2013*) that was derived from the ice-load history and the viscosity profiles. These findings indicate that most of the long-term changes in vertical loads, which were estimated from GNSS and GRACE, are due to GIA. The largest vertical changes are mainly concentrated in the Ronne Ice Shelf, the Ross ice shelf, Enderby Land, Amery Ice Shelf and Princess Elizabeth Land. To have consistency between the time span of records at 44 GNSS sites and GRACE time coverage, we selected only 8 stations (those which have data over the whole period as GRACE from April 2002 until June 2017) to conduct the comparison of vertical displacement rates from GNSS and GRACE. The annual signals from GNSS and GRACE are plotted in Fig. 9. For most of sites, the GRACE signal appears to be in phase and have the same amplitude as GPS signal. A particularly good agreement is seen at sites of CAS1, CRAR, DAV1 and MAW1. This shows that the ice mass changes close to these sites can (to a large extent) explain the surface deformations, because the vertical displacements from GNSS include the loading deformation due to the mass changes as well as the vertical crustal motions. There are also sites where the GNSS and GRACE estimates differ significantly in amplitude and phase, like OHI3 and PALM sites instated in the Antarctica Peninsula.

5. Discussion

Large uncertainties in GRACE and ICESat estimates are mainly due to the GIA effect (cf. *Gunter el al., 2009; Ivins et al., 2013*). The knowledge of GIA with a high accuracy is thus indispensable for studying changes in total mass budget of the Antarctic ice sheet. Moreover, the estimates of ice elevation changes from ICESat are affected by an unknown time-varying compaction effect of snow and firn ice that complicates the conversion of elevation-to-mass changes. Whether using the density of ice (917 $\mathrm{kg/m^3}$) or the surface mass density model, the results are exactly correct only in an ideal condition that obviously deviates from the actual situation in many regions of

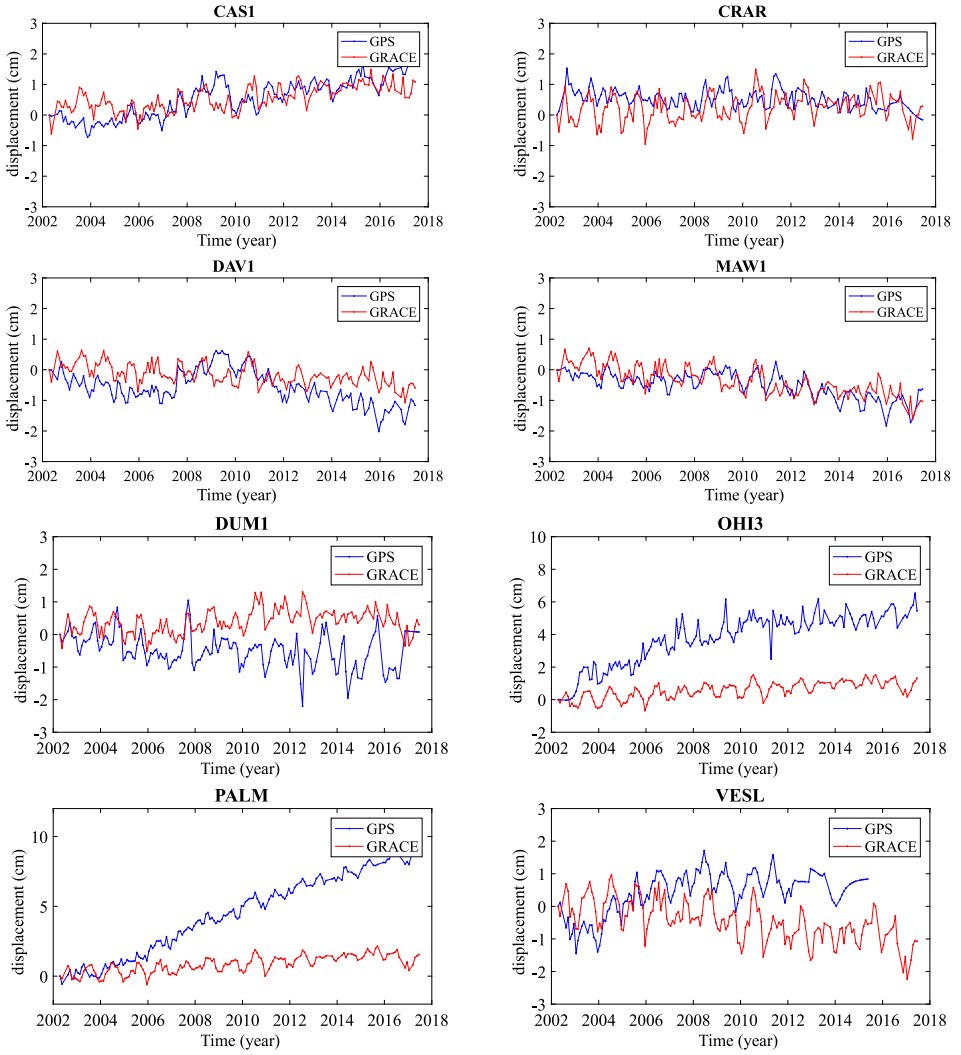

Fig. 9. The vertical displacments at 8 GNSS sites in Antarctica from GNSS and GRACE.

Antarctica, especially along ice sheet margins where mass fluctuations are quite large. Areas with large uncertainties are generally concentrated in areas with high ice flow rates. The more complex the ice sheet elevation changes in regions with a higher ice flow velocity (mostly coastal areas), the

greater the uncertainties of ICESat results. Furthermore, regions with a high ice flow velocity are characterized by typically larger mass changes and consequently affected more by a leakage effect that substantially influences GRACE estimates.

The discrepancies between the load displacements monitored by GNSS and GRACE might be explained by the fact that surface displacements at these GNSS sites are also affected by the thermo-elastic deformations associated with surface temperature changes in addition to the influence of surface mass redistribution (*Tan et al., 2016; 2017*). While the GRACE observations are only sensitive to mass changes, they are not affected by the surface temperature. Another possible reason for these differences is a limited spatial resolution of GRACE. Moreover, GRACE estimates represent regional averages, while the GNSS estimates reflect vertical motions at particular locations.

6. Summary and Conclusions

We have investigated the ice mass changes, the ice elevation changes and vertical displacements in Antarctica from processing GRACE and ICESat data. In addition, we analyzed the vertical displacement from GNSS data and GIA model.

According to our results, the total mass change of the Antarctic ice sheet was at a rate of -162.91 ± 5.09 Gt/yr during the period from April 2002 to June 2017. Most of these changes are attributed to the ice mass loss of the West Antarctic ice sheet (at a rate of -143.11 ± 2.24 Gt/yr) and the Antarctic Peninsula ice sheet (at a rate of -24.31 ± 0.71 Gt/yr). In contrast, we detected a small ice mass increase (at a rate of 5.29 ± 3.54 Gt/yr) of the East Antarctic ice sheet over the investigated period. These significant spatial heterogeneities (Fig. 3) in changes of the total mass balance reflect a unique topography and climatic conditions of different regions at this continent. Interestingly, the most significant spatial factor is not necessary the contrast between coastal and inland areas that mainly controls the total mass budget in Greenland. Instead, in Antarctica the contrast between mass changes in West and East Antarctica are also significant. The fastest ice mass loss was detected in Amundsen Sea Embayment (i.e. Marie Byrd Land) at a rate up

to −10 cm/yr. Among remarkable spatial variations in the ice mass changes, we detected also large temporal variations in different regions during the investigated period of fifteen years. Overall, temporal variations of ice mass changes over the entire continent of Antarctica could be characterized by an accelerating mass loss from March 2003 until December 2012, followed by slowing trend after January 2013 until June 2017.

The large ice mass loss detected by GRACE in the Amundsen Sea Embayment was confirmed from ICESat data, with the localized extreme decrease in ice elevations at a rate of −6.4 m/yr inferred over the terminus of Smith Glacier. This significant dynamic thinning was explained by ocean currents. In Dronning Maud Land, the ICESat estimates indicate a relatively significant dynamic thickening at a rate of 0.30 m/yr.

The vertical load displacement rates estimated by GRACE and GNSS are in good agreement with the GIA model developed by *A et al. (2013)* based on the ICE5G ice-load history, the VM2 viscosity profile and the same PREM elastic structure. For most sites, the GRACE signal appears to be in phase and have the same amplitude as those detected from GNSS, but large discrepancies were also found. These discrepancies might be due to the fact that GNSS estimates are also affected by the thermo-elastic deformations associated with surface temperature, while GRACE detects only mass changes.

Acknowledgements. This research was funded by the Hong Kong Research Grants Council, Project 1-ZE8F: Remote-sensing data for studying Earth's and planetary inner structure.

References

A G., Wahr J., Zhong S., 2013: Computations of the viscoelastic response of a 3-D compressible Earth to surface loading: an application to Glacial Isostatic Adjustment in Antarctica and Canada. Geophys. J. Int., **192**, 2, 557–572, doi: 10.1093/gji/ggs030.

Boening C., Lebsock M., Landerer F., Stephens G., 2012: Snowfall-driven mass change on the East Antarctic ice sheet. Geophys. Res. Lett., **39,** 21, L21501, doi: 10.1029/2012GL053316.

Chen J. L., Wilson C. R., Blankenship D., Tapley B. D., 2009: Accelerated Antarctic ice loss from satellite gravity measurements. Nat. Geosci., **2**, 859–862, doi: 10.1038/ngeo694.

Chen J. L., Wilson C. R., Blankenship D. D., Tapley B. D., 2006: Antarctic mass rates from GRACE. Geophys. Res. Lett., **33**, 11, L11502, doi: 10.1029/2006GL026369.

Dutrieux P., De Rydt J., Jenkins A., Holland P. R., Ha H. K., Lee S. H., Steig E. J., Ding Q., Abrahamsen E. P., Schröder M., 2014: Strong sensitivity of Pine Island ice-shelf melting to climatic variability. Science, **343,** 6167, 174–178, doi: 10.1126/science.1244341.

Farrell W. E., 1972: Deformation of the Earth by surface loads. Rev. Geophys., **10**, 3, 761–797, doi: 10.1029/RG010i003p00761.

Gunter B., Urban T., Riva R., Helsen M., Harpold R., Poole S., Nagel P., Schutz B., Tapley B., 2009: A comparison of coincident GRACE and ICESat data over Antarctica. J. Geod., **83,** 11, 1051–1060, doi: 10.1007/s00190-009-0323-4.

Hanna E., Navarro F. J., Pattyn F., Domingues C. M., Fettweis X., Ivins E. R., Nicholls R. J., Ritz C., Smith B., Tulaczyk S., Whitehouse P. L., Zwally H. J., 2013: Ice-sheet mass balance and climate change. Nature, **498,** 7452, 51–59, doi: 10.1038/nature12238.

Ivins E. R., James T. S., Wahr J., Schrama E. J. O., Landerer F. W., Simon K. M., 2013: Antarctic contribution to sea level rise observed by GRACE with improved GIA correction. J. Geophys. Res. Solid Earth, **118,** 6, 3126–3141, doi: 10.1002/jgrb.50208.

Jacob T., Wahr J., Pfeffer W. T., Swenson S., 2012: Recent contributions of glaciers and ice caps to sea level rise. Nature, **482**, 7386, 514–518, doi: 10.1038/nature10847.

Klees R., Revtova E., Gunter B., Ditmar P., Oudman E., Winsemius H., Savenije H., 2008: Filter design for GRACE gravity models. Geophys. J. Int., **175**, 2, 417–432, doi: 10.1111/j.1365-246X.2008.03922.x.

Lenaerts J. T. M., van Meijgaard E., van den Broeke M. R., Ligtenberg S. R. M., Horwath M., Isaksson E., 2013: Recent snowfall anomalies in Dronning Maud Land, East Antarctica, in a historical and future climate perspective. Geophys. Res. Lett., **40**, 11, 2684–2688, doi: 10.1002/grl.50559.

Mouginot J., Rignot E., Scheuchl B., 2014: Sustained increase in ice discharge from the Amundsen Sea Embayment, West Antarctica, from 1973 to 2013. Geophys. Res. Lett., **41,** 5, 1576–1584, doi: 10.1002/2013GL059069.

Pritchard H. D., Arthern R. J., Vaughan D. G., Edwards L. A., 2009: Extensive dynamic thinning on the margins of the Greenland and Antarctic ice sheets. Nature, **461,** 7266, 971–975, doi: 10.1038/nature08471.

Shepherd A., Wingham D., 2007: Recent sea-level contributions of the Antarctic and Greenland ice sheets. Science, **315,** 5818, 1529–32, doi: 10.1126/science.1136776.

Tan W., Dong D., Chen J., Wu B., 2016: Analysis of systematic differences from GPS-measured and GRACE-modeled deformation in Central Valley, California. Adv. Space Res., **57**, 1, 19–29, doi: 10.1016/j.asr.2015.08.034.

Tan W., Xu X., Dong D., Chen J., Wu B., 2017: Thermoelastic Seasonal Deformation in Chinese Mainland. Acta Geod. et Cartogr. Sin., **46**, 9, 1080–1087, doi: 10.11947/j.AGCS.2017.20160628.

Tang J., Cheng H., Liu L., 2012: Using nonlinear programming to correct leakage and estimate mass change from GRACE observation and its application to Antarctica. J. Geophys. Res. Solid Earth, **117,** B11, B11410, doi: 10.1029/2012JB009480.

Van Wessem J. M., Reijmer C. H., Morlighem M., Mouginot J., Rignot E., Medley B., Joughin I., Wouters B., Depoorter M. A., Bamber J. L., Lenaerts J. T. M., Van De Berg W. J., Van Den Broeke M. R., Van Meijgaard E., 2014: Improved representation of East Antarctic surface mass balance in a regional atmospheric climate model. J. Glaciol., **60**, 222, 761–770, doi: 10.3189/2014JoG14J051.

Velicogna I., 2009: Increasing rates of ice mass loss from the Greenland and Antarctic ice sheets revealed by GRACE. Geophys. Res. Lett., **36**, 19, L19503, doi: 10.1029/2009GL040222.

Velicogna I., Sutterley T. C., van den Broeke M. R., 2014: Regional acceleration in ice mass loss from Greenland and Antarctica using GRACE time-variable gravity data. Geophys. Res. Lett., **41,** 22, 8130–8137, doi: 10.1002/2014GL061052.

Velicogna I., Wahr J., 2006: Measurements of time-variable gravity show mass loss in Antarctica. Science, **311,** 5768, 1754–1756, doi: 10.1126/science.1123785.

Velicogna I., Wahr J., 2013: Time-variable gravity observations of ice sheet mass balance: Precision and limitations of the GRACE satellite data. Geophys. Res. Lett., **40**, 12, 3055–3063, doi: 10.1002/grl.50527.

Wahr J., Swenson S., Velicogna I., 2006: Accuracy of GRACE mass estimates. Geophys. Res. Lett., **33**, 6, L06401, doi: 10.1029/2005GL025305.

Wahr J., Molenaar M., Bryan F., 1998: Time variability of the Earth's gravity field: Hydrological and oceanic effects and their possible detection using GRACE. J. Geophys. Res., Solid Earth, **103**, B12, 30205–30229, doi: 10.1029/98JB02844.

Zammit-Mangion A., Rougier J., Schön N., Lindgren F., Bamber J., 2015: Multivariate spatio-temporal modelling for assessing Antarctica's present-day contribution to sea-level rise. Environmetrics, **26,** 3, 159–177, doi: 10.1002/env.2323.

Zwally H. J., Giovinetto M. B., Li J., Cornejo H. G., Beckley M. A., Brenner A. C., Saba J. L., Yi D., 2005: Mass changes of the Greenland and Antarctic ice sheets and shelves and contributions to sea-level rise: 1992–2002. J. Glaciol., **51,** 175, 509–527, doi: 10.3189/172756505781829007.

sciendo

Contributions to Geophysics and Geodesy Vol. 49/4, 2019 (425–440)

LAS: A combination of the analytic signal amplitude and the generalised logistic function as a novel edge enhancement of magnetic data

Luan Thanh PHAM[1,*], Erdinc OKSUM[2], Thanh Duc DO[1], Minh LE-HUY[3], Minh Duc VU[1], Vinh Duc NGUYEN[1]

[1] Faculty of Physics, VNU University of Science, Vietnam National University, Hanoi, Vietnam

[2] Süleyman Demirel University, Engineering Faculty, Department of Geophysical Engineering, Isparta, Turkey

[3] Institute of Geophysics, Vietnam Academy of Science and Technology, 18 Hoang Quoc Viet, Cau Giay, Hanoi, Vietnam

Abstract: In the evaluation of magnetic field data, edge enhancement and detection techniques are important treatments for the interpretation of geological structures. In general geological sense, contiguity of deep and shallow magnetic sources leads to weak and intense anomalies that complicates the interpretation to disclose adjacent anomalous sources. Many of the existing filters for edge detection in magnetics mostly have the disadvantage that they require a reduction to pole transformation as the pre-process of the data or they cannot balance weak and intense anomalies and therefore fail in detecting edges of deep and shallow sources simultaneously. This study presents an improved edge detection filter LAS (logistic function of the analytical signal), based on the generalised logistic function configured by the ratio of derivatives of the analytical signal. This novel approach has the capability of reducing the dependence on the direction of the magnetization and also balancing anomalies of sources at different levels of depth. The feasibility of the method is examined on both theoretical and real data cases comparatively with some other methods that utilize the analytical signal in their basis. In comparison, the results demonstrate that the LAS method provides more accurate estimation of edge localization.

Key words: generalised logistic function, analytic signal amplitude, edge detection

1. Introduction

The determination of the edges of the anomalous bodies is one of the important tasks in magnetic interpretation. The data usually contain the effect

*corresponding author: e-mail: luanpt@hus.edu.vn

doi: 10.2478/congeo-2019-0022

of sources located at different positions either in horizontal or vertical plane or the effects of sources with different magnetic properties, thus the overall anomaly mostly comprise weak and strong intensities together in the same frame. Most of existing edge detector filters are based on vertical and horizontal derivatives of the data. In this context, the 3D analytic signal (AS) (also called the total gradient) proposed by *Roest et al. (1992)* is one of the commonly used edge detection filter. *Hsu et al. (1996)* introduced an enhanced analytical signal (AS_2) that uses the higher order derivatives to reduce the interference effect due to adjacent sources.

Many previous works have interpreted the magnetic anomaly data using the AS and AS_2 (e.g. *Le-Huy et al., 2001, 2002; Salem and Ravat, 2003; Paoletti et al., 2004; Fairhead and Williams, 2006; Saleh and Pašteka, 2012; Saibi et al., 2016; Tran and Nguyen, 2017*). However, both the AS and AS_2 have limited achievement in simultaneously disclosing the edges from high and low amplitude anomalies. To balance the amplitudes of the different anomalies, normalized edge detector filters are used. *Miller and Singh (1994)* introduced the tilt angle that is defined as the arctangent of the ratio between vertical gradient and total horizontal gradient of the data. *Verduzco et al. (2004)* proposed the use of the total horizontal gradient of tilt angle. *Wijns et al. (2005)* suggested using the theta map method that is, in theory, the same angle as the tilt angle of the magnetic anomaly data. *Cooper and Cowan (2006)* suggested using horizontal tilt angle. *Ferreira et al. (2013)* introduced the tilt angle of the horizontal derivative amplitude. *Zhang et al. (2014)* used the tilt angle of the first order vertical gradient of the total horizontal gradient. *Ma et al. (2014)* used the tilt angle of the ratio between the first order horizontal gradient and the second order horizontal gradient. *Yao et al. (2015)* used the normalized enhanced analytic signal; *Chen et al. (2017)* used modified theta map filters. *Nasuti and Nasuti (2018)* proposed using a modified tilt angle that based on the vertical derivative of the analytical signal amplitude in different. *Pham et al. (2019)* suggested the use of the horizontal gradient amplitude configured in the generalised logistic function. However, although they can balance high and low amplitudes of anomalies, they still require pole reduction of the magnetic data (*Li and Pilkington 2016; Nguyen et al., 2017; Pham et al., 2018; Pham et al., 2019*). On the other hand, *Ansari and Alamdar (2011)* described the use of the analytic signal amplitude of the tilt angle

(AT) which can be applied to the magnetic dataset directly. Although the method is more effective than the analytic signal, it still performs poorly in detecting all the edges of the body (*Cooper, 2014a*). *Cooper (2014a)* presented another approach namely the tilt angle of the amplitude of analytical signal (TAS) which is less dependent on the direction of the magnetization vector. In this study, we introduce an enhanced balanced edge detection filter that has reduced dependence on magnetization vector direction to improve edge detection.

The proposed filter utilises the generalised logistic function build up with the ratio of vertical derivative to total horizontal derivative of the AS. The potentiality of the proposed method is experienced on model anomalies of both 1D and 2D data and also on real magnetic anomalies from central India where the results are compared with other methods that realize the analytic signal amplitude and its modiefied versions.

2. Method

The generalised logistic function of the horizontal gradient amplitude is defined as (*Nelder, 1961; Birch, 1999; Malkina-Pykh and Pykh, 2013; Pham et al., 2019*):

$$\mathrm{LTHG} = \left[1 + \exp\left(-\frac{\dfrac{\partial \mathrm{THG}}{\partial z}}{\sqrt{\left(\dfrac{\partial \mathrm{THG}}{\partial x}\right)^2 + \left(\dfrac{\partial \mathrm{THG}}{\partial y}\right)^2}}\right)\right]^{-\alpha}, \tag{1}$$

where THG is the total horizontal derivative of the magnetic intensity anomaly $M(x, y)$:

$$\mathrm{THG}(x, y) = \sqrt{\left(\frac{\partial M}{\partial x}\right)^2 + \left(\frac{\partial M}{\partial y}\right)^2}, \tag{2}$$

and α is a positive constant number decided by the interpreter. By Eq. (1), the method can equalize signals from different levels of depth. However, its practical application in magnetic interpretation still requires the pole reduction of the data.

Here we suggest replacing THG by AS that is less dependent on the magnetization vector direction than the THG. Therefore, Eq. (1) becomes:

$$\mathrm{LAS} = \left[1 + \exp\left(-\frac{\dfrac{\partial \mathrm{AS}}{\partial z}}{\sqrt{\left(\dfrac{\partial \mathrm{AS}}{\partial x}\right)^2 + \left(\dfrac{\partial \mathrm{AS}}{\partial y}\right)^2}}\right)\right]^{-\alpha}, \tag{3}$$

where

$$\mathrm{AS} = \sqrt{\left(\frac{\partial M}{\partial x}\right)^2 + \left(\frac{\partial M}{\partial y}\right)^2 + \left(\frac{\partial M}{\partial z}\right)^2}. \tag{4}$$

Following *Florio et al. (2006)*, the analytic signal is a nonharmonic function, so its vertical derivative cannot be computed by conventional methods. The direct expressions for the derivatives of the analytic signal amplitude are given by *Cooper (2014b)* as:

$$\frac{\partial \mathrm{AS}}{\partial x} = \frac{\dfrac{\partial M}{\partial x}\dfrac{\partial^2 M}{\partial x^2} + \dfrac{\partial M}{\partial y}\dfrac{\partial^2 M}{\partial x \partial y} + \dfrac{\partial M}{\partial z}\dfrac{\partial^2 M}{\partial x \partial z}}{\mathrm{AS}}, \tag{5}$$

$$\frac{\partial \mathrm{AS}}{\partial y} = \frac{\dfrac{\partial M}{\partial x}\dfrac{\partial^2 M}{\partial x \partial y} + \dfrac{\partial M}{\partial y}\dfrac{\partial^2 M}{\partial y^2} + \dfrac{\partial M}{\partial z}\dfrac{\partial^2 M}{\partial y \partial z}}{\mathrm{AS}}, \tag{6}$$

$$\frac{\partial \mathrm{AS}}{\partial z} = \frac{\dfrac{\partial M}{\partial x}\dfrac{\partial^2 M}{\partial x \partial z} + \dfrac{\partial M}{\partial y}\dfrac{\partial^2 M}{\partial y \partial z} + \dfrac{\partial M}{\partial z}\dfrac{\partial^2 M}{\partial z^2}}{\mathrm{AS}}. \tag{7}$$

The enhancement by this configuration reduces the dependence on the direction of the magnetization but also balances anomalies from different levels of depth and produces maximal amplitudes on the edges of source body.

This filter uses the ratio of derivatives of the amplitude of analytic signal to display the edges of strong and weak amplitude simultaneously. The main attributes of our edge detector filter are to provide maximum peak values on the edges of source body, as well as to reduce the dependence on the direction of the magnetization and to balance anomalies from shallow and deep sources.

3. Methods used for comparison

Four different methods based on analytical signal which can be applied directly to the magnetic data set have been chosen to show comparatively the effectiveness of the LAS method. They are the analytical signal (AS) (Eq. (4)), the enhanced analytical signal (AS_2), the analytical signal amplitude of the tilt angle (AT) and the tilt angle of the ratio of derivatives of the analytic signal amplitude (TAS).

The AS_2 is based on the higher order derivatives to enhance the source edges. This filter is given by *Hsu et al. (1996)*:

$$\mathrm{AS}_2 = \sqrt{\left(\frac{\partial M_{zz}}{\partial x}\right)^2 + \left(\frac{\partial M_{zz}}{\partial y}\right)^2 + \left(\frac{\partial M_{zz}}{\partial z}\right)^2}, \tag{8}$$

where M_{zz} is the second order derivative of the magnetic intensity anomaly.

Ansari and Alamdar (2011) used the analytic signal amplitude of the tilt angle. Its expression is:

$$\mathrm{AT} = \sqrt{\left(\frac{\partial T}{\partial x}\right)^2 + \left(\frac{\partial T}{\partial y}\right)^2 + \left(\frac{\partial T}{\partial z}\right)^2}, \tag{9}$$

where:

$$T = \mathrm{atan}\left(\frac{\dfrac{\partial M}{\partial z}}{\sqrt{\left(\dfrac{\partial M}{\partial x}\right)^2 + \left(\dfrac{\partial M}{\partial y}\right)^2}}\right). \tag{10}$$

Cooper (2014a) suggested the use of the arctangent function of the ratio of derivatives of the analytic signal expressed as:

$$\mathrm{TAS} = \mathrm{atan}\frac{\dfrac{\partial \mathrm{AS}}{\partial z}}{\sqrt{\left(\dfrac{\partial \mathrm{AS}}{\partial x}\right)^2 + \left(\dfrac{\partial \mathrm{AS}}{\partial y}\right)^2}}. \tag{11}$$

4. Synthetic examples

In this section, the proposed method is applied to 2D and 3D synthetic examples to evaluate its effectiveness. The results of the present method

were compared with the results of AS, AS_2, AT and TAS methods. In the 2-D example, the above methods are applied to magnetic anomalies (Fig. 1b) due to a 2D block (Fig. 1a) for a range of geomagnetic field inclinations (0°, 30°, 60°, and 90°). Figs. 1c,d,e and f display the outputs of AS, AS_2,

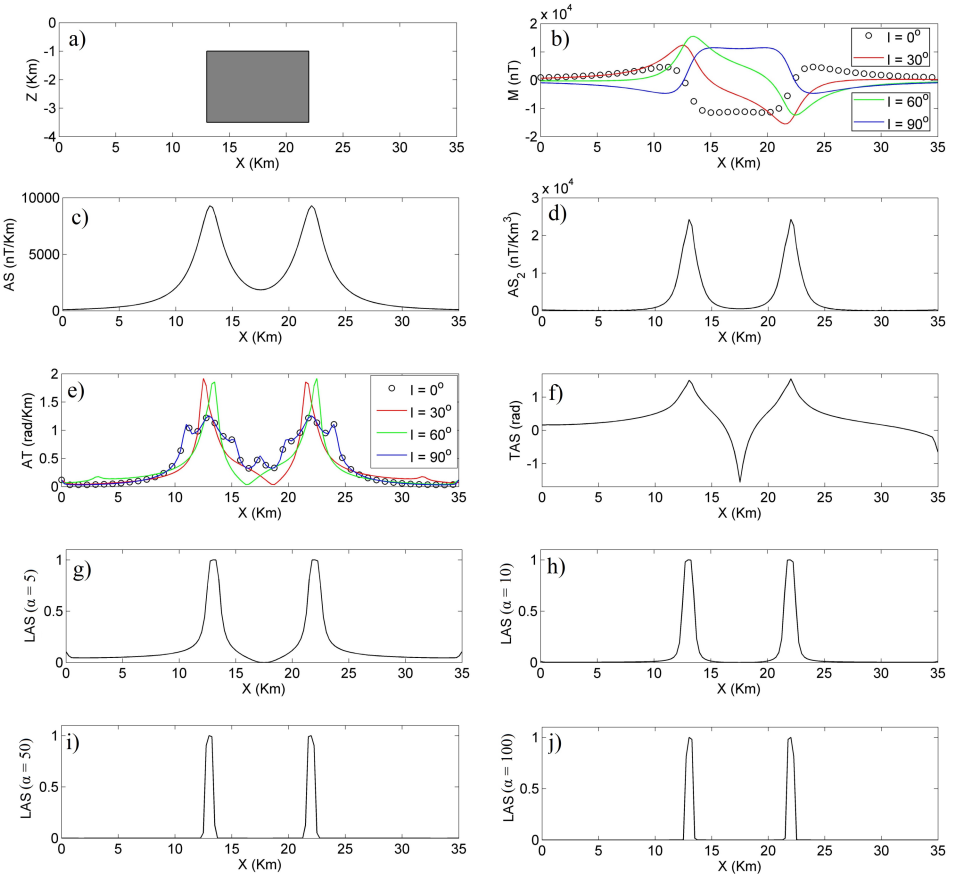

Fig. 1. (a) 2D block model (gray shading); (b) Total magnetic intensity M across a 2D block (Fig. 1a) with varying inclinations; (c) The analytic signal amplitude AS for all varieties of inclinations; (d) The enhanced analytic signal AS_2 for all varieties of inclinations; (e) The analytic signal amplitude of the tilt angle AT for all varieties of inclinations; (f) The tilt angle of the analytic signal amplitude TAS for all varieties of inclinations; (g) The generalised logistic function of the analytic signal amplitude LAS for all varieties of inclinations, with $\alpha = 5$; (h) with $\alpha = 10$; (i) with $\alpha = 50$; (j) with $\alpha = 100$.

AT and TAS applied to the data given in Fig. 1b. The maxima of the AS, AS_2, AT and TAS can automatically recognise the edges of the source body. In this case, the AS, AS_2 and TAS are independent of magnetization direction, but for the AT, this independence is seem lost. Figs. 1g,h,i and j show the application of the proposed method with different values of the parameter α (5, 10, 50 and 100). The LAS filter successfully detects the edges of the causative body when apply directly to the magnetic data, which clearly gives better resolution of the source edges than other filters, and can display the edges in a more centralized way. It can be observed from these figures that, as the value of the parameter α increase, the resolution of the edges of the sources also increases. Tests showed that $\alpha \geq 10$ yielded the best results.

The efficiency of the proposed method is also evaluated by two 3-D synthetic examples. The first 3D example involves a single prism with dimensions of $32 \times 32 \times 2\,\mathrm{km}^3$, at a depth of 2 km, induced magnetization of 5 A/m, rotation angle of 30°, and a magnetization vector with an inclination of 30° and a declination of −1°. Fig. 2 illustrates the geometric appearance of the model. Fig. 3a shows the theoretical magnetic anomaly due to this model calculated by the forward formula of *Rao and Babu (1991)* on a field dimension of 63.5 × 63.5 km with 0.5 km grid steps. The outlines of the body are shown by the black lines in planar views. Fig. 3b is the AS and Fig. 3c is the AS_2 of the magnetic data in Fig. 3a. It can be observed from these figures that the AS is not effective in balancing of high and low amplitude anoma-

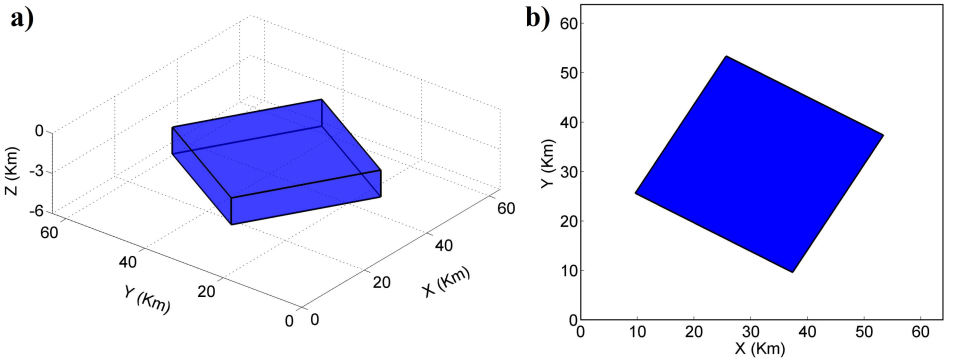

Fig. 2. (a) A 3D view of a synthetic model with one prism; (b) Plan view of the synthetic model in (a).

lies simultaneously. Although the AS_2 has a better resolution than the AS, similar shortcomings can also be observed for this as well. Fig. 3d shows the AT of the magnetic anomaly data in Fig. 3a. The AT is more effective than the AS and AS_2 in balancing all the edges of the source body, but although the maximal values of AT can enclose the borders of the source, estimation of edges near to the corners are diffused. Figs. 3e and f show the TAS and LAS of the magnetic data in Fig. 3a, respectively. Although the TAS can enhance all the edges of the source body, the identified edges is lower in resolution. Besides, the maximum values of LAS delineates the edges of the real model more in detail. Consequently, by the overall comparison of the edge detection results obtained from the four filters applied in this example, the LAS filter achieves higher resolution of the edges than the others.

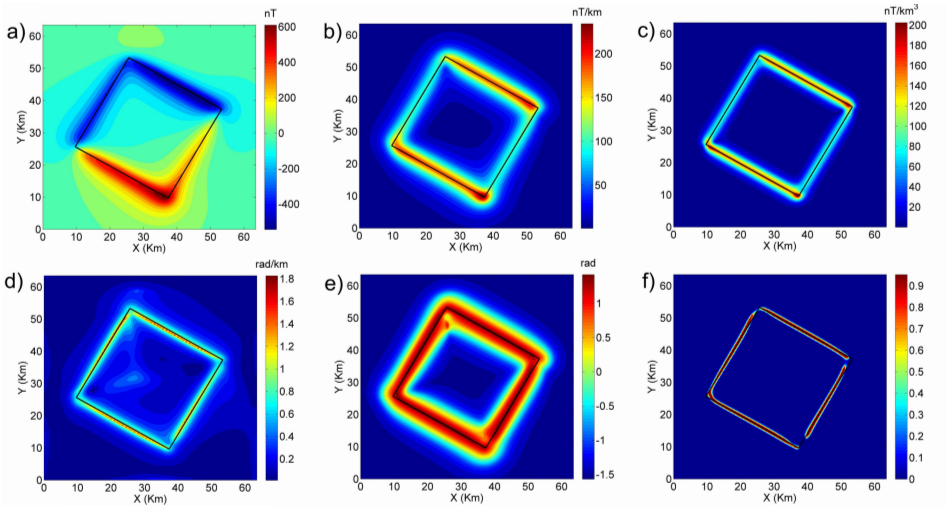

Fig. 3. (a) Synthetic magnetic anomaly of the single prism model; (b) AS; (c) AS2; (d) AT; (e) TAS; (f) LAS; with $\alpha = 50$.

The second 3D example involves three prisms same in size but located at different depths and also with varied low magnetic inclinations (Table 1). Fig. 4 illustrates the geometric appearance of the three prisms (A, B and C) model. Fig. 5a shows the magnetic anomaly due to the three prisms with addition of 0.2 % Gaussian random noise in order to examine also the influence of noise in this example. The outlines in plan view of the bodies are shown by the black lines in all figures. Because the filters are defined

Table 1. Parameters of the three prism model.

Parameters / Prism ID	A	B	C
Center coordinates (km; km)	12; 31.5	31.5; 31.5	51; 31.5
Inclination I (°)	8	10	12
Declination D (°)	25	26	27
Magnetization (A/m)	5	5	5
Length × Width (km)	45×10	45×10	45×10
Depth of top (km)	1	2	3
Depth of bottom (km)	2	3	4
Rotation angle (°)	0	0	0

by derivatives which increase the noise influence, upward continuation filter is applied prior to calculations of edge detection. Fig. 5b,c,d,e and f display the results of the AS, AS_2, AT, TAS and LAS after upward continuation of 0.2 km, respectively. As can be seen from Fig. 5b, in this low-inclination case, the AS is only effective in delineating two of the four edges of each causative body. It is worth noting that the AS_2 uses third order derivatives of the anomalies while the others use first or second order derivatives, thus, this filter is more sensitive to noise. In this case, the AS_2 is only effective in enhancing two of the four edges of shallow source (body A), and fails to detect any edges from the deeper sources (body B and C) (Fig. 5c). Likewise, even though there are some offset from the actual edges, the edges of the shallow source are determined by the AT, but the edges associated with the deeper sources cannot be effectively identified by this filter (Fig. 5d). In comparison, the AT is clearly more sensitive to noise than the AS and

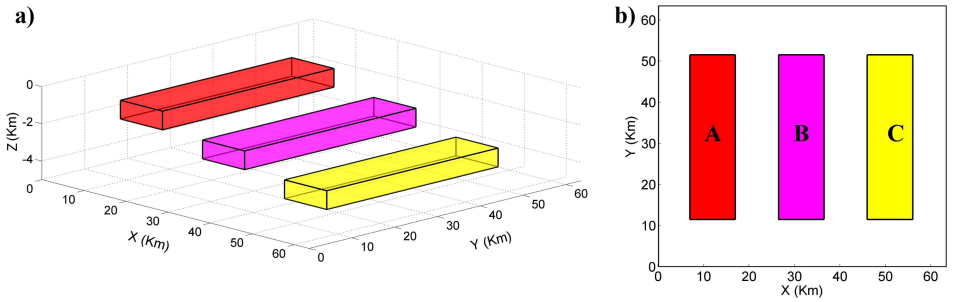

Fig. 4. (a) A 3D view of a synthetic model with three prisms; (b) Plan view of a synthetic model with three prisms.

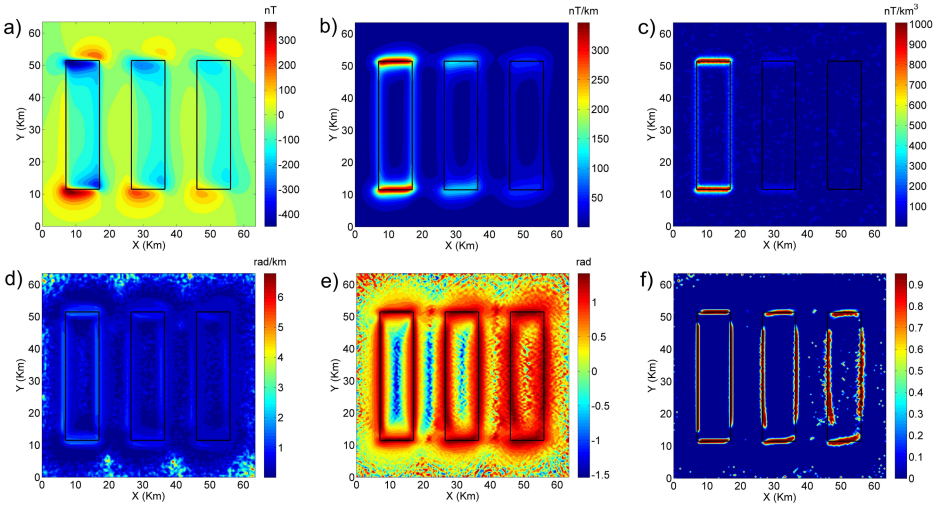

Fig. 5. (a) Synthetic magnetic anomaly of three prisms model; (b) AS; (c) AS2; (d) AT; (e) TAS; (f) LAS, with $\alpha = 50$.

LAS. As can be seen from Fig. 5e and f, the TAS and LAS filters can enhance all the edges of the three causative bodies even they are located at different depths. Besides, although the results of the TAS and LAS methods produce similar results, it can be observed that LAS method discloses the true edges in higher resolution. Furthermore, it also takes advantage because the response of LAS values are nearly similar in amplitude with each other even the anomalies from the depth varied sources have different amplitudes. By comparison among the results in Fig. 5, it is apparent that the LAS results in enhance the edges to be more visible and the response is gained sharp over the true edges more than the AS, AS_2, AT and TAS filters do.

5. Real magnetic data application

In this section, the practical applicability of the method proposed is demonstrated with the interpretation of magnetic anomaly data from the central part of the Indian continent (Fig. 6a). The study area lies between 80.49°E and 81.40°E, of the eastern longitudes and 23.6°N and 24.35°N, of northern latitudes, covering an area about 101 km by 83 km. This area is located in a seismically active transition zone featured with varying geological complex-

ities such as variation of density, magnetic susceptibility, seismic velocities, thermal regime, etc. (*Ghosh, 2016*). Fig. 6b shows the geological map of the area with different subsurface geological formation types, viz., Semri, Rewa, Bhander, Gondwana, Gneisses, Mahakoshal, Granite Plutons and Kaimur groups exist in the area with various ages of geological features (*Mohanty, 2012; Ghosh, 2016; Chetty, 2017*). A regional fault namely the Sone-Narmada fault is marked by the northern boundary of Mahakoshal groups ages (*Mohanty, 2012*). A number of subparallel east-northeast to west-southwest trending major shear zones dissecting the study area are also seen on the map.

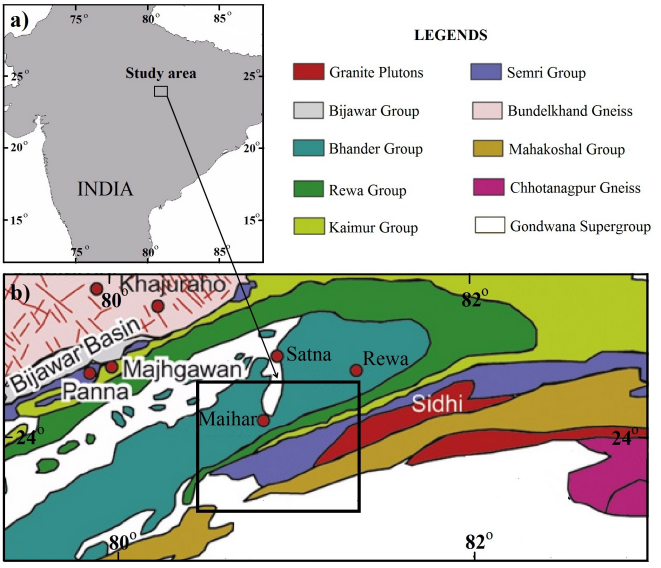

Fig. 6. Location and geological maps of the study area (modifed after *Mohanty, 2012*).

Fig. 7a shows the total field magnetic anomaly data of the study area (*Ghosh*, 2016) digitized on a 108 × 66 grid along the north–south and east–west directions, respectively. Following *Ghosh (2016)*, the magnetic data have been acquired by Geological Survey of India (*Project Crumansonata, 1995*). The data have been collected by Scintrex Fluxgate (MFM-2) magnetometer with the station interval of 1.0 km. The data set vary from −813 to 953 nT with anomalies having higher intensities locate over the northern part of the area, whereas anomalies having lower intensities appear in

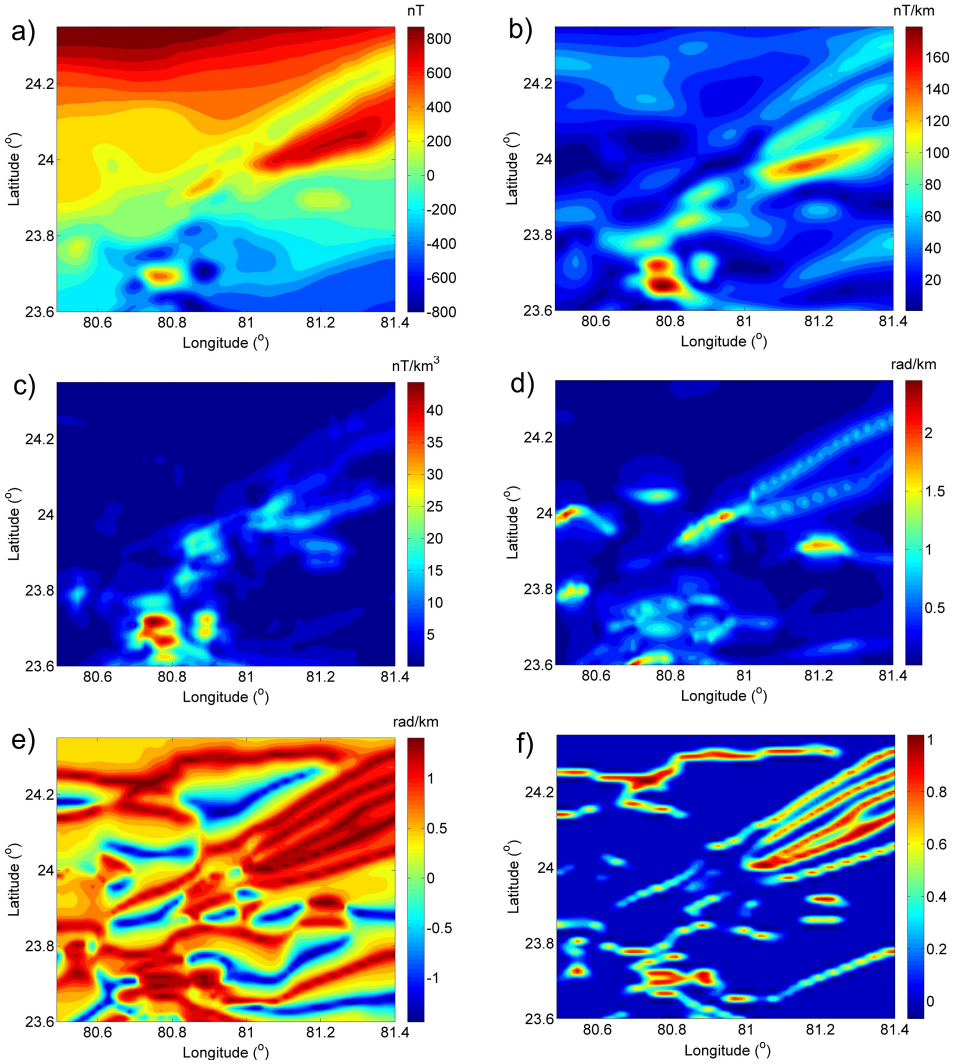

Fig. 7. (a) The total field magnetic anomaly of the study area; (b) AS; (c) AS2; (d) AT; (e) TAS; (f) LAS, with $\alpha = 10$.

the southern part. The magnetic data trends in the area are varying east-northeast to west-southwest direction. In order to attenuate the effects of shortest wavelenghts upward continuation to 2 km height is applied to the data set prior to determination of the edges. Hereby, this operation also

produced results that are smoother and less sensitive to random noise than the original anomaly, but will not change the primary structures of the area. Fig. 7b,c,d and e show the AS, AS_2, AT and TAS after upward continuation of magnetic dataset shown in Fig. 7a. It can be seen that the AS filter perform poor at balancing the edges from high and low amplitude anomalies simultaneously. As expected (and discussed in the above sections), the AS_2 and AT results as more noisy than the other filters outputs and also give insufficient results to accurately determine the edges of the magnetic sources. The results from TAS reveals to be more effective in determining the source edges than the AS, AS_2 and AT but the recognized edges from this data are diffused as well.

Fig. 7f illustrates the LAS response of the upward continuated magnetic data. Both the TAS and LAS filters are less sensitive to noise than the AS_2 and AT, so can delineate more outlines than these methods. It can be observed from Figs. 7b,c,d,e and f that the LAS is not only effective in balancing the different amplitude edges, but also provides the higher resolution, and can detect the edges of source body more prominently and precisely, making the geological structures more visible. By and large, as can be observed from Fig. 6b and Fig. 7f, there is a good correlation between the edges obtained from LAS filter and geologic structures, with many of structure trends are oriented in an east-northeast to west-southwest direction in the study area. However, some magnetic structures in the north-western part of this area are not identified by geological map alone (Fig. 6b) and their existence can only be detected through interpretation of the magnetic field data.

6. Conclusions

In this study, we introduced an improved edge detection method LAS based on the configuration of the generalised logistic function and the ratio of the vertical gradient and total horizontal gradient of the analytical signal amplitude. Unlike almost other edge enhancement methods that require a reduction to the pole or pseudogravity transformation prior to application, the LAS can be applied to the magnetic dataset directly. The disadvantage of the proposed method is that it is more sensitive to noise than some conventional methods that use only first-order derivatives of the field. Using an

upward continuation filter, the noise effect can be reduced. The evaluation of the method comparative with other filters on both the synthetic and real magnetic data illustrate the capability and practicability for interpretation of magnetic data. The results show that the presented method can not only balance the amplitude responses from both shallow and deep sources, but also give a higher resolution, and can detect the source edges more clearly and precisely.

Acknowledgements. The authors would like to thank the editor Peter Vajda and Dr. Roman Pašteka for their very useful suggestions to improve the manuscript.

References

Ansari A. H., Alamdar K., 2011: A new edge detection method based on the analytic signal of tilt angle (ASTA) for magnetic and gravity anomalies. Iran. J. Sci. Technol., **35**, 2, A2, 81–88, doi: 10.22099/IJSTS.2011.2131.

Birch C., 1999: A New Generalized Logistic Sigmoid Growth Equation Compared with the Richards Growth Equation. Ann. Bot., **83**, 6, 713–723, doi: 10.1006/anbo.1999.0877.

Chen A. G., Zhou T. F., Liu D. J., Zhang S., 2017: Application of an enhanced theta-based filter for potential field edge detection: a case study of the Luzong ore district. Chin. J. Geophys., **60**, 2, 203–218, doi: 10.1002/cjg2.30039.

Chetty T. R. K., 2017: Proterozoic Orogens of India, A Critical Window to Gondwana. Chapter 4 ? The Central Indian Tectonic Zone. 211–265, doi: 10.1016/B978-0-12-804441-4.00004-3.

Cooper G. R. J., 2014a: Reducing the dependence of the analytic signal amplitude of aeromagnetic data on the source vector direction. Geophysics, **79**, 4, J55–J60, doi: 10.1190/geo2013-0319.1.

Cooper G. R. J., 2014b: The Automatic Determination of the Location and Depth of Contacts and Dykes from Aeromagnetic Data. Pure Appl. Geophys., **171**, 9, 2417–2423, doi: 10.1007/s00024-014-0789-8.

Cooper G. R. J., Cowan D. R., 2006: Enhancing potential field data using filters based on the local phase. Comput. Geosci., **32**, 10, 1585–1591, doi: 10.1016/j.cageo.2006.02.016.

Fairhead J. D., Williams S. E., 2006: Evaluating normalized magnetic derivatives for structural mapping. SEG Technical Program Expanded Abstracts, SEG 2006 New Orleans, **25**, 1, 845?849, doi: 10.1190/1.2370388.

Ferreira F. J. F., Souza J., Bongiolo A. B. S., Castro L. G., 2013: Enhancement of the total horizontal gradient of magnetic anomalies using the tilt angle. Geophysics, **78**, 3, J33–J41, doi: 10.1190/geo2011-0441.1.

Florio G., Fedi M., Pasteka R., 2006: On the application of Euler deconvolution to the analytic signal. Geophysics, **71**, 6, L87–L93, doi: 10.1190/1.2360204.

Ghosh G. K., 2016: Magnetic data interpretation for the source-edge locations in parts of the tectonically cctive transition zone of the Narmada-Son lineament in central India. Pure Appl. Geophys., **173**, 2, 555–571, doi: 10.1007/s00024-015-1082-1.

Hsu S. K., Coppense D., Shyu C. T., 1996: High-resolution detection of geologic boundaries from potential field anomalies: An enhanced analytic signal technique. Geophysics, **61**, 2, 373–386, doi: 10.1190/1.1443966.

Le-Huy M., Luu H. V., Cao T. D., 2001: Some modern methods of the interpretation aeromagnetic data applied for Tuan Giao region. Vietnam J. Earth Sci., **23**, 3, 207–216, doi: 10.15625/0866-7187/23/3/11333, (in Vietnamese with English summary).

Le-Huy M., Luu H. V., Cao T. D., 2002: Using the maximum horizontal gradient vector to interpret magnetic and gravity data in Vietnam. Vietnam J. Earth Sci., **24**, 1, 67–80, doi: 10.15625/0866-7187/24/1/11380, (in Vietnamese with English summary).

Li X., Pilkington M., 2016: Attributes of the magnetic field, analytic signal, and monogenic signal for gravity and magnetic interpretation. Geophysics, **81**, 6, 79?86, doi: 10.1190/geo2015-0697.1.

Ma G., Liu C., Li L., 2014: Balanced horizontal derivative of potential field data to recognize the edges and estimate location parameters of the source. J. Appl. Geophys., **108**, 12–18, doi: 10.1016/j.jappgeo.2014.06.005.

Malkina-Pykh I. G., Pykh, Y. A., 2013: The Method of Response Function in Psychology and Sociology. Southampton Boston: WIT Press, p. 69.

Miller H. G., Singh V., 1994: Potential field tilt—a new concept for location of potential field sources. J. Appl. Geophys, **32**, 213–217, doi: 10.1016/0926-9851(94)90022-1.

Mohanty S., 2012: Spatio-temporal evolution of the Satpura Mountain Belt of India: A comparison with the Capricorn Orogen of Western Australia and implication for evolution of the supercontinent Columbia. Geosci. Front., **3**, 3, 241–267, doi: 10.1016/j.gsf.2011.10.005.

Nasuti Y., Nasuti A., 2018: NTilt as an improved enhanced tilt derivative filter for edge detection of potential field anomalies. Geophys. J. Int., **214**, 1, 36–45, doi: 10.1093/gji/ggy117.

Nelder J. A., 1961: The Fitting of a Generalization of the Logistic Curve. Biometrics, **17**, 1, 89–110, doi: 10.2307/2527498.

Nguyen H. T. T., Do T. D., Le-Huy M., 2017: Application of directional derivative method to determine boundary of magnetic sources by total magnetic anomalies. Vietnam J. Earth Sci., **39**, 4, 360–375, doi: 10.15625/0866-7187/39/4/10731.

Paoletti V., Fedi M., Florio G., Supper R., Rapolla A., 2004: The new integrated aeromagnetic map of the Phlegrean Fields volcano and surrounding areas. Ann. Geophys.-Italy, **47**, 5, 1569–1580, doi: 10.4401/ag-3360.

Pham L. T., Le-Huy M., Oksum E., Do T. D., 2018: Determination of maximum tilt angle from analytic signal amplitude of magnetic data by the curvature-based method, Vietnam J. Earth Sci., **40**, 4, 354–366, doi: 10.15625/0866-7187/40/4/13106.

Pham L. T., Oksum E., Do T. D., 2019: Edge enhancement of potential field data using the logistic function and the total horizontal gradient, Acta Geod. Geophys., **54**, 1, 143–155, doi: 10.1007/s40328-019-00248-6.

Project Crumansonata, 1995: Geoscientific studies of the Son-Narmada-Tapti lineament zone. Calcutta, Geological Survey of India, Special publication, 10, pp. 371.

Rao D. B., Babu N. R., 1991: A rapid method for three-dimensional modeling of magnetic anomalies. Geophysics, **56**, 11, 1729–1737, doi: 10.1190/1.1442985.

Roest W. R., Verhoef J., Pilkington M., 1992: Magnetic interpretation using the 3-D analytic signal. Geophysics, **57**, 1, 116–125, doi: 10.1190/1.1443174.

Tran D. T., Nguyen M. Q., 2017: Eruptive-volcanic-basalt structures in the Truong Sa-Spratly Islands and adjacent areas from interpreting gravity and magnetic data. Vietnam J Earth Sci, **39**, 1, 1–13, doi: 10.15625/0866-7187/39/1/9167.

Saibi H., Azizi M., Mogren S., 2016: Structural Investigations of Afghanistan Deduced from Remote Sensing and Potential Field Data. Acta Geophys., **64**, 4, 978–1003, doi: 10.1515/acgeo-2016-0046.

Saleh S., Pašteka R., 2012: Applying the regularized derivatives approach in Euler deconvolution and modeling geophysical data to estimate the deep active structures for the northern Red Sea Rift region, Egypt. Contrib. Geophys. Geod., **42**, 1, 25–61, doi: 10.2478/v10126-012-0003-x.

Salem A., Ravat D., 2003: A combined analytic signal and Euler method (AN-EUL) for automatic interpretation of magnetic data. Geophysics, **68**, 6, 1952–1961, doi: 10.1190/1.1635049.

Verduzco B., Fairhead J. D., Green C. M., MacKenzie C., 2004: New insights into magnetic derivatives for structural mapping. Lead. Edge, 23(2), 116–119, doi: 10.1190/1.1651454.

Wijns C., Perez C., Kowalczyk P., 2005: Theta map: edge detection in magnetic data. Geophysics, **70**, 4, 39–43, doi: 10.1190/1.1988184.

Yao Y., Huang D., Yu X., Chai B., 2015: Edge interpretation of potential field data with the normalized enhanced analytic signal. Acta Geod. Geophys., **51**, 1, 125–136, doi: 10.1007/s40328-015-0120-x.

Zhang X., Yu P., Tang R., Xiang Y., Zhao C. J., 2014: Edge enhancement of potential field data using an enhanced tilt angle. Explor. Geophys., **46**, 3, 276–283, doi: 10.1071/EG13104.

sciendo

Contributions to Geophysics and Geodesy Vol. 49/4, 2019 (441–458)

Characterization of the leakage problem in Salhab earthen dam using electrical resistivity tomography and SP measurements, Syria

Walid AL-FARES

Atomic Energy Commission of Syria, Department of geology,
P.O. Box 6091, Damascus, Syria
e-mail: cscientific@aec.org.sy, tel.: +963-11-2132580, fax: +963-11-6112289

Abstract: The earthen dam of Salhab is located in the southern margins of Al-Ghab plain at 3–4 km of Salhab town northern-west of Syria. The dam consists of two separated embankments: the main one extends east-west along a distance of 895 m with 14.5 m height, while the second embankment towards northwest-southeast over a distance of 510 m and 11 m of height. The dam crest has a constant topographic elevation of 220 m above sea level (a.s.l). Electrical Resistivity Tomography surveys (ERT) combined with a Self-Potential measurements (SP), were implemented at the upstream and at the top of the main and the secondary embankments of the dam in order to identify the possible leakage zones under the dam's body. The interpretation of the ERT sections and the SP measurements, carried out at the upstream side, revealed a distinct zone of leakage extending along the beginning and the end parts under the main embankment. Moreover, many punctual anomalous spots of low resistivity values were recognized within the dam's clay core. One of those spots was confirmed by the implementation of a detailed ERT profile and by a piezometric borehole drilled at the top of the dam. Whereas, the clay core of the secondary embankment seems relatively coherent and homogeneous as well as a trace of a tectonic fault was identified under the end part of the embankment body but no manifestations of leakage were observed under and behind the secondary dam body.

Key words: ERT and SP surveys, leakage, Salhab earthen dam, Syria

1. Introduction

Leakage issue is a common problem and widely happens in the earth fill dams either through its foundations or through the dam body itself. The Subsurface geological structure and tectonic features are the most factors leading to the occurrence of leakage processes form dams (*Johansson and Dahlin, 1996; Panthulu et al., 2001; Foster et al., 2002; Al-Fares, 2014; Bedrosian et al., 2012*). The evolution of leakage problem within or under

doi: 10.2478/congeo-2019-0023

the dam body leads to increasing the leaking rate and affects directly on the safety and stability of the dam (*Sjödahl et al., 2006; Asfahani et al., 2010; Bedrosian et al., 2012*). Therefore, it is necessary to conduct periodic monitoring for the leakage rates to avoid the occurrence of a sudden failure or collapse of the dam. Using modern and sophisticated geophysical techniques contributes significantly in giving an image of the subsurface geological features and consequently outlining the possible paths of water leakage (*Seaton and Burbey, 2002; Cho and Yeom, 2007; Al-Fares, 2011; Ikard et al., 2013; Gutiérrez et al., 2015*). This certainly assists in providing appropriate technical solutions to reduce the leaking rates and ensure the safety and stability of the dam.

The Salhab earthen dam is located in north-west of Syria at the southern Al-Ghab plain margins north-west Hama city (Fig. 1). The dam consists of two embankments: the main one extends east-west and has a length of 895 m, and it has 14.5 m of height, while the second towards northwest-southeast with the length of 510 m and 11 m of height. The both dam's embankments have a constant topographic level of 220 m above sea level

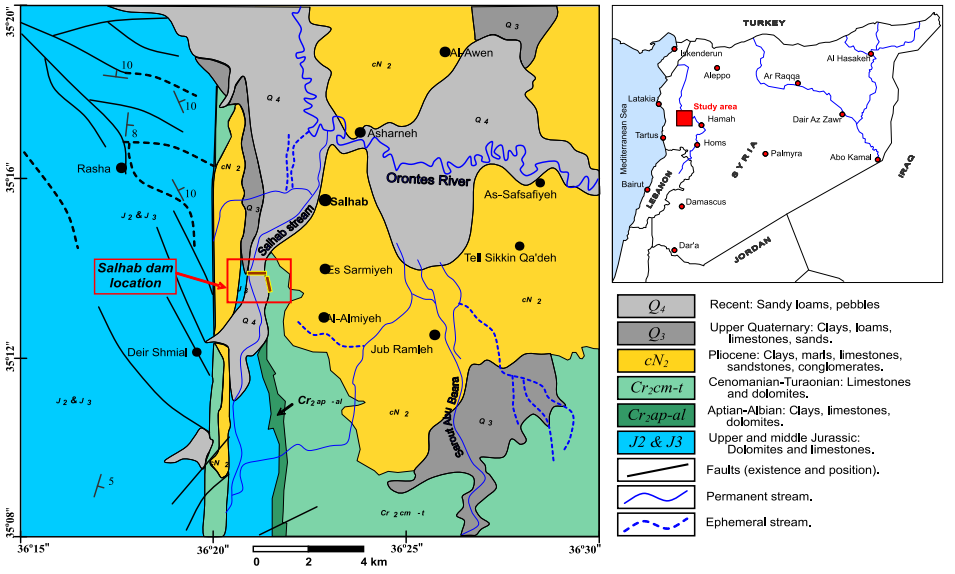

Fig. 1. Simplified geological map of the study area showing the location of Salhab dam (modified after *Ponikarov, 1963*).

(Fig. 2). The dam's lake has a surface of the 145 hectares with 2 km of length and 7.75 Mm^3 as a storage capacity. The dam was built on Salhab riverbed in 1993 in order to fend off the floods on Al-Ghab plain and to storage the water for agricultural uses in summer. Most of the water of reservoir comes from the flows of the karstic springs scattered on the slopes of the mountain heights located at the west and south of the dam site and close to Deir Shamil village. After putting the dam in operation for the first time, a water flow was observed exiting from the piezometric wells drilled behind the main embankment body and the amount of the percolated water through the leaching channel reached up to 160 L/s, especially when the storage level passes 210 m (*Al-Diab, 2008*). This phenomenon is continuing and repeated during the consecutive storage periods. In the current case study, the Electrical Resistivity Tomography (ERT) method and SP measurements were proposed to contribute in outlining the possible zones of water leakage through the implantation of many geo-electrical profiles close and along the dam body. Since this technique has provided its performance in giving a clear image of the substructure and localizing the probable leaks paths in many earthen dams studies (*Oh and Sun, 2008; Osazuwa and Chii, 2009; Moore et al., 2011; Thompson et al., 2012*).

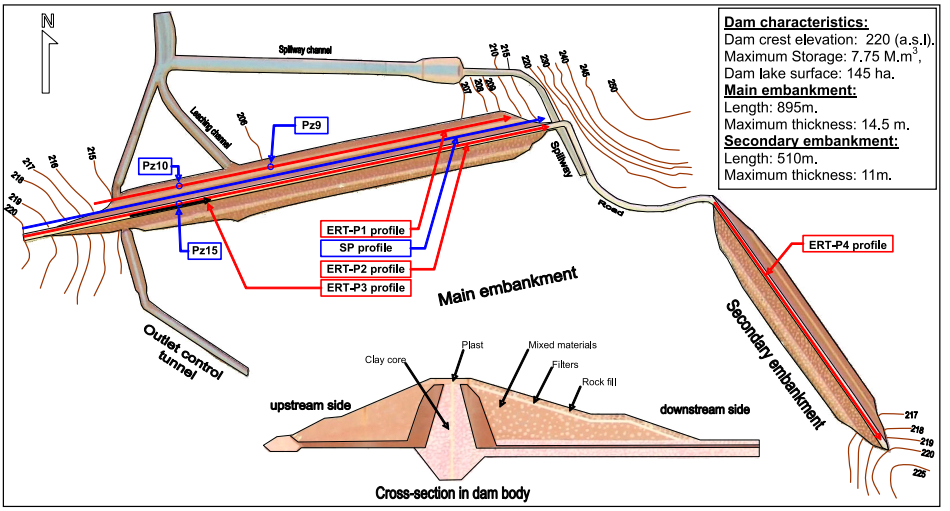

Fig. 2. Shows the general structure of Salhab dam, and the locations of the ERT, SP profiles and Pz piezometric boreholes.

Therefore, the aim of the present case study is to identify the potential zones of leakage in the dam through mapping in detail the subsurface structures of the geological formations underneath and behind the dam body by the implementation of numbers of electrical resistivity tomography profiles combined with SP measurements and available boreholes logs data.

2. Geological and hydrogeological settings

Salhab dam is located at the southern fringes of Al-Ghab plain depression (Fig. 1). The region including the dam area is strongly influenced by the tectonic activities of the Dead Sea Faults Systems (DSFS) of the large Asian-African Rift (*Devyatkin et al., 1997; Brew, 2001*). The central parts of Al-Ghab depression are filled by Neogene and Quaternary alluvium deposits with thickness reaching more than 100 m. These deposits are overlaying uncomfortably the Cretaceous calcareous rocks, which constitute basement of the Al-Ghab basin (*Ponikarov, 1963; Gomez et al., 2006*). From a local geological perspective, the mountains located to the west of Salhab dam consist of fractured and karstified limestones and dolomites rocks of Upper and Middle Jurassic (J_3, J_2). While the heights located at the East of the dam are compounded by limestones and dolomites rocks of Cenomanian-Turonian (Cr_2cm-t). These rocks are outcropping over formations of limestones and dolomites, alternating with marly and chalky limestones of Aptian and Albian formation (Cr_1ap-al).

With regard to the dam site, the preliminary investigations and the geological maps 1/200,000 and 1/50,000 (*Ponikarov, 1963; General Establishment for Geology and Mineral Resources, 1984*) indicate that the storage basin of the dam, close to the axe of the main embankment, is covered by Quaternary alluvial deposits compounded essentially from clays, loams, sands and pebbles (Q_4). These deposits overlay a geological formation consisting of marls, limestones, sandstones and consolidated conglomerates referred to the upper Miocene and Pliocene (cN_2). The conglomerates are composed of rounded to sub-angular pebbles and boulders in limy cement, whereas, the alluvial deposits, close to the secondary embankment, cover a layer composed of marly calcareous rocks. The difference in the geological structure of the storage basin close to the main and secondary embankments of the dam is due to the presence of a tectonic fault on the left shoulder

of the dam extending parallel to the main course of the dam valley. This fault led to the decline of the level of the storage basin and the rise of the Cretaceous plateaus chain in the east and played later an important role in determining the current course of the Salhab stream.

From hydrogeology point of view, the Quaternary alluvium deposits, which are composed from clays, sands and gravels, constitute the shallow groundwater aquifer in the study area. According to the hydrogeological investigations carried out in the site, the groundwater level appears at a depth ranging between 12–15 m, nearby the main embankment, while it is about 24 m close to the second embankment. Whereas the limestone and dolomite formations referred to the Jurassic and Cretaceous ages, constitute the main and the deep aquifer in the region. These formations are characterized by high permeability due to the presence of cracks, fractures and karstic voids at various depths. The limestone and dolomite rocks are considered the main source of all of the karstic springs feeding the local rivers and streams in the region. In general, the groundwater flow directs from West to East perpendicular to water flow of Salhab river.

3. Methodology and instruments

3.1. ERT measurements

The electrical resistivity tomography (ERT) was applied in Salhab earthen dam to identify the origin of the leakage observed behind the dam body while the dam is partially filled with water. For this purpose, three ERT profiles (ERT-P1, ERT-P2, and ERT-P3) of different lengths have been conducted in upstream and at the top of the main embankment (Figs. 2 and 3). Only one ERT profile (ERT-P4) was carried out at the top of the secondary embankment. The ERT profiles were straight and parallel to the dam body and realized at water storage level of 215 m (a.s.l.).

To execute the field measurements, the resisto-meter Syscal Switch-72 was used. The instrument is equipped with a control unit and four multi-swatches cable bobbins to connect 72 electrodes at once with maximum inter-electrodes step of 5 m. The 72 electrodes are planted in a straight line along the measurement profile. Electrodes checking and the data collecting are performed automatically according to a mathematical sequence prepared

in advance using special software. Each standard sequence of 360 m length includes 759 measuring points distributed on 16 levels of depth. In the case where the profile is longer than the standard sequence (up of 360 m), a roll-along sequence or more are required to end the profile of the measurements. The roll-along sequence should be compatible with the standard one in term of configuration and the electrodes interval. The roll-along sequence used includes 304 additional measuring points. The collected data are au-

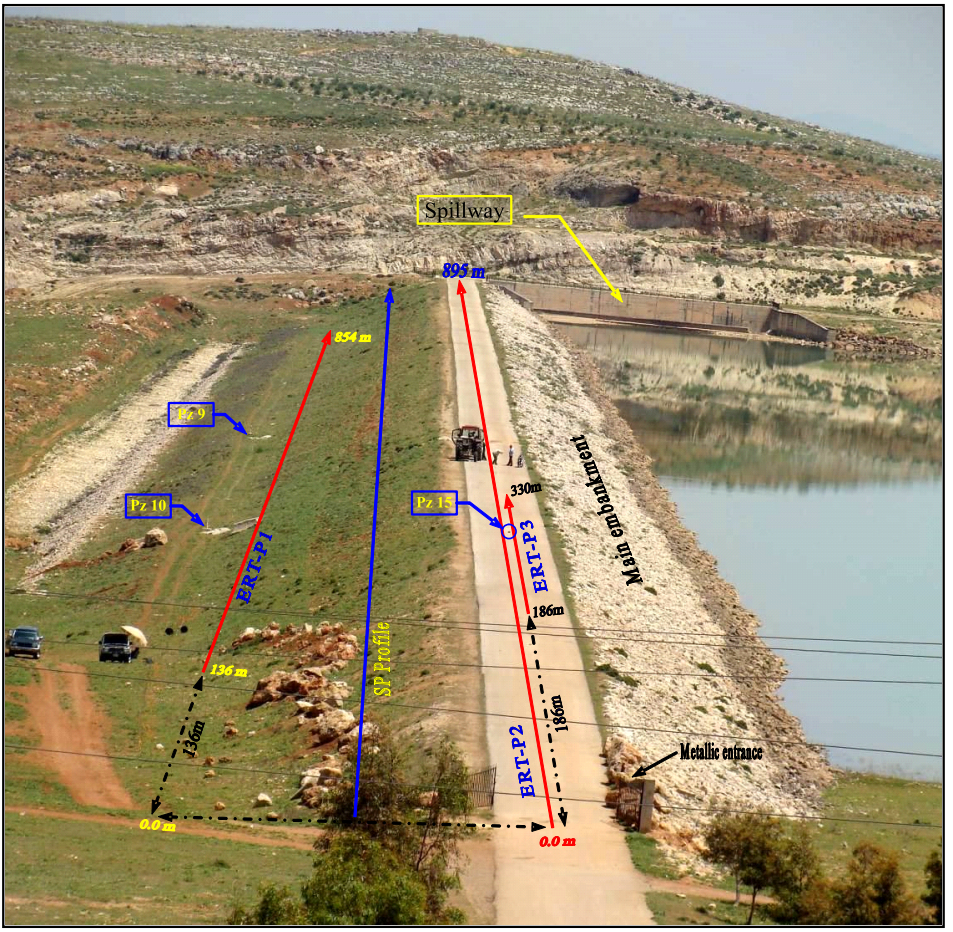

Fig. 3. View for arrangement of the ERT and SP profiles carried out in Salhab dam, and the locations of the piezometric boreholes Pz9, Pz10 and Pz15.

tomatically stored in the instrument's memory using Schlumberger-Wenner sequence with an inter-electrode spacing of 2 or 5 m.

3.2. SP measurements

Within the framework of this work, a team from the Directorate General of Water Resources of Damascus, implemented the field SP measurement simultaneously with the ERT surveys (*Omer and Habashiya, 2008*). The resisto-meter SAS-300 (Sudesh made) equipped by non-polarized electrodes was used to carry the SP measurements. To perform the field measurements, the non-polarized electrodes are filled with copper sulfate solution where one electrode remains fixed in a certain point and the other electrode is moved according to a constant measurement step every 5 m. More than 10 SP profiles were executed in upstream side of the main and the secondary embankments and the lake shoulders. The SP profile marked in the Figs. 2 and 3 was the closer to the ERT-P2 profile; therefore the two profiles were interpreted together.

4. Results and discussion

In order to interpret the ERT profiles, the raw data stored in the resisto-meter memory were transported to a PC and inverted using RES2DINV program developed by *Loke and Barker (1996).* The ERT data were inverted using the least-squares method including smoothing of model resistivity to get better results. This method depends on reducing the differences between the measured and calculated apparent resistivity values. The inverse model resistivity section represents the true resistivity values of the subsurface geological formations.

4.1. ERT-P1 profile

This profile is carried out on the terrace of the main embankment backside, which has a steady topographic level of 212 m (Fig. 3). This profile starts at the point 136 m from the metallic entrance of the dam. The dam entrance was considered as a reference start point for all of the ERT profile

implemented at the main embankment. This profile was carried out with 2 m inter-electrode spacing and extends along a distance of 718 m. The Fig. 4 shows the geo-electrical inverted section of the ERT-P1 profile where a surface layer extending horizontally along the profile section can be distinguished. The thickness of this layer ranges between 0 and 5 m and it increases toward the end of the geo-electrical section. The resistivity values of this layer vary between 15–30 Ωm, most likely related to the main components of the embankment terrace, which is composed of a mixture of sandy clays and some gravels. Structurally, this layer seems homogenous and no anomalous features can be noted.

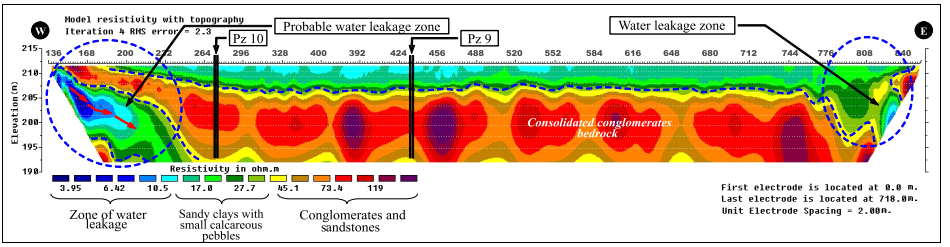

Fig. 4. Interpretation of the ERT-P1 profile carried out on the upstream terrace of the main embankment of Salhab dam, Pz9 and Pz10 are piezometric boreholes.

Underlying, a notable and geometric homogenous thick layer, parallel to the previous terrace, can be mapped. This layer structurally seems to be uniform over all the profile except at the two edges. It is almost related to the consolidated conglomerate and sandstone formation referred to it in the geological setting. This formation could be considered as the main compact bedrock in the basin of the dam lake. The thickness of this formation reaches more than 15 m and the resistivity values ranging between 40–150 Ωm. The available real data, derived from the piezometric boreholes logs Pz10 and Pz9, which are implanted on the terrace behind the dam body, confirms this finding (Figs. 4 and 5). Moreover, an up normal blue zone is observed at the beginning of the ERT-P1 section. This zone has a limited shape and it seems to be perched under the beginning of indicated previous bedrock layer. The observed zone is characterized by low resistivity values ranging between 4–10 Ωm. These low values could be influenced either by a groundwater flow coming from the neighbouring mountainous western slopes towards the dam area or it could be a result of leakage process from the dam's lake especially

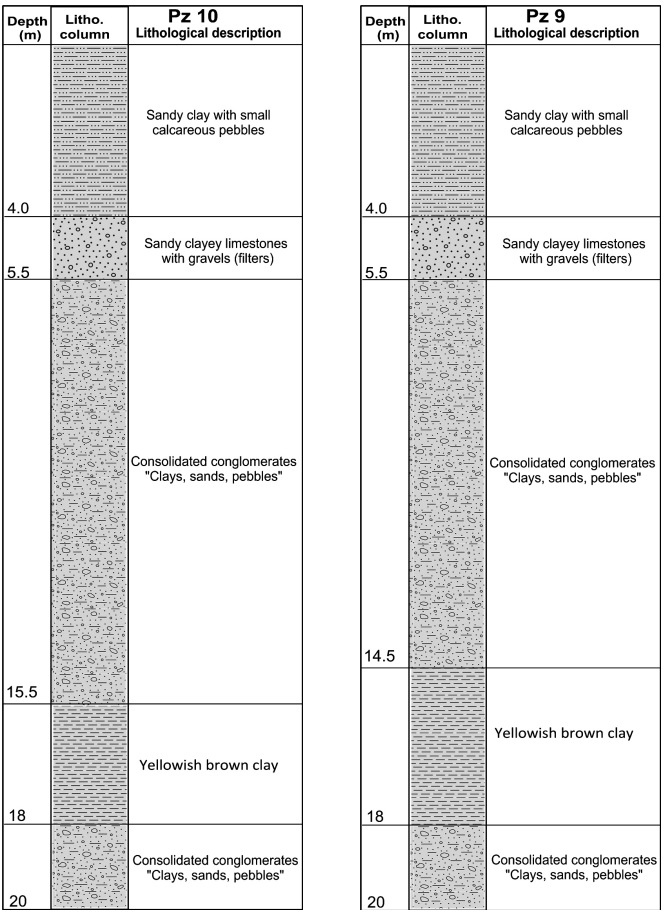

Fig. 5. The piezometric borehole logs of the Pz10 and Pz9 drilled on the terrace of the main embankment backside (modified after the *General Company for Water Studies, 2008*).

when the water storage level starts rising. Another structural anomaly is also identified at the end part of the geo-electrical section between the distance of 770 and 830 m, where a discontinuity feature can be traced at the end of the bedrock layer. This feature is situated opposite to the dam's flooding channel (spillway) and could constitute a possible flow path for water via the contact zone between the embankment body and adjacent rocks formation.

4.2. ERT-P2 profile

This profile is performed along the crest of the main embankment and it extends along a distance of 895 m long, with constant topographic elevation of 220 m above sea level (Fig. 3). In order to carry out this profile on the top of the dam, the hard asphaltic layer was punctured every 5 m using an electrical driller to facilitate the plantation of the electrodes. In this case, the investigation depth of the used configuration is about 50 m. The implanted electrodes were wetted with water and some clay added to ensure the contact with the ground and to reduce the perturbation resulting from the electrodes effect. The Fig. 6 shows the interpretation of the inverted geo-electrical section of the ERT-P2 profile. The blue doted straight line represents the water level in the lake through the measurements, while the red dotted line represents the boundaries of the dam body (clay core) with the natural land surface in the lake. According to the ERT-P2 section, a blue zone of low resistivity values (less than 20 Ωm) is appeared in the left part of the section and extends along the first 300 m beneath the boundaries of the dam body. The presences of this zone again in this section enhance what was observed in the previous profile. On other hand, the results obtained from the interpretation of the SP measurements which is carried out at the slope of main embankment backside, confirm the presence of this leakage zone. The Fig. 7 shows the compatibility between the results of the interpretation of SP and ERT-P2 section, where an anomaly of negative SP values (less than −40 mV) can be noted along the first 350 m of the two profiles which corresponds to the blue zone of the low resistivity mentioned above. This finding enhances again the possibility of the occurrence of the leakage processes through this sector and cause a flow of water from the piezometric boreholes drilled behind the dam particularly when the storage level rises.

The specified range of the red dotted line outlines the boundaries of the clay core of the main embankment (Fig. 5). Where, the resistivity values are ranging between 30 and 60 Ωm. Several separated small zones of low resistivity values, can be observed within the clay core at several distances 300, 480, 640, and 840 m along the ERT-P2 section. All of these zones are located between the 200 and 210 m topographic levels. The existence of such abnormal areas could be affected by the occurrence of some leaking or filtration processes through the clay core leading to wetting some parts

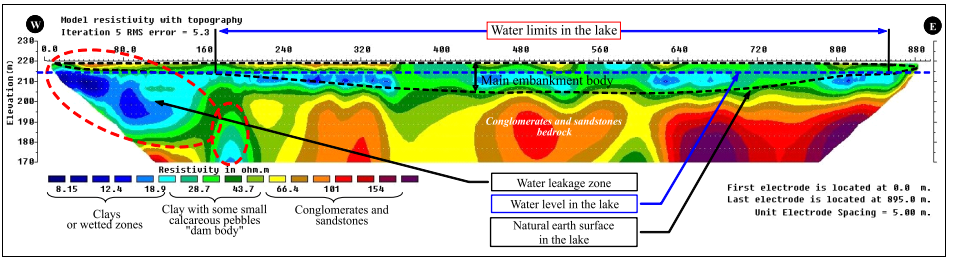

Fig. 6. Interpretation of the ERT-P2 profile carried out along the crest of the main embankment of Salhab dam.

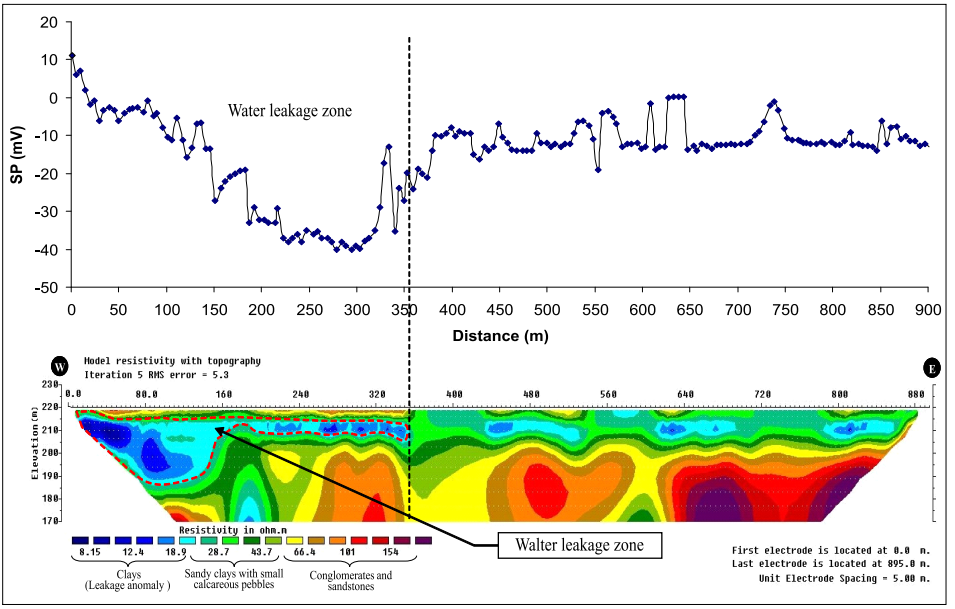

Fig. 7. Illustrates the compatibly between the results of the ERT section and the SP measurements carried out at the main embankment of Salhab dam.

inside the dam body. Therefore, to confirm the presence of such these filtration zones and to explain the appearance of water in the piezometric borehole Pz15, a short detail ERT profile was carried out at the top of the embankment adjacent to Pz15, this will be discussed later through the interpretation of ERT-P3 profile.

Just below the main embankment of the dam, a somewhat heterogeneous layer appears. This layer is expressed by resistivity values ranging between 70 and 200 Ωm. The heterogeneity in this layer could be due to the presence of consolidated conglomerates in some parts, accompanied with clay, sandstone and marl in other parts. The thickness of this layer exceeds more than 30 m forming the main bedrock beneath the dam body.

4.3. ERT-P3 profile

This profile is carried out on the top of the main embankment in order to clarify the presence of the water in the piezometer Pz15. The start point of this profile is located at 186 m from metallic dam entrance (Fig. 3). This profile extends along a distance of 144 m with 2 m as inter-electrodes spacing. The Fig. 8 illustrates the geo-electrical section of the ERT-P3 profile. A thin surface layer of 1–1.5 m thickness can be distinguished, this layer represents the plast layer which is composed of sands and gravel protected by a thin asphaltic sheet covering the top of the embankment. The resistivity of this layer reaches more than 220 Ωm.

The rest of the ERT section represents the clay core of the embankment body, where two geo-electrical layers can be outlighting: the first one extends alone all the section and has a thickness 5 m (net blue colour) and it is confined between the levels 212 and 217 m. This layer is relatively characterized by low resistivity values varying between 12–20 Ωm and seems to be uniform and homogenous. While, the layer below, represents the lower part

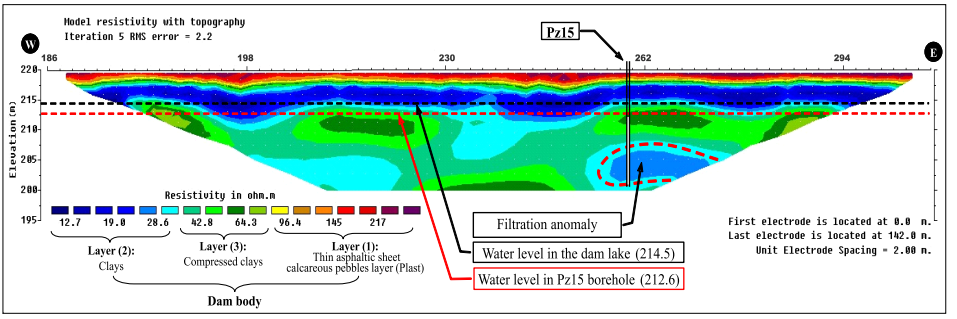

Fig. 8. Interpretation of the ERT-P3 profile carried out at the top of the main embankment, which is passed by the Pz15 borehole.

of the clay core which shows a slight increase in the resistivity values varying between 30–75 Ωm. The increasing in the resistivity values may possibly be attributed to the changing of the nature of the clay core components or it could be related to dynamic factors such as the compression applied on the clayey landfills through the construction of the dam body. On the other hand, an anomaly of low resistivity is appeared as a blue spot at the base and around the piezometric borehole Pz15 base (Fig. 8). This may explicate the presence of water inside the borehole, which could be almost related to the existence of a fable filtration in this part of the dam body. It is also worth mentioned that through the drilling of Pz15 borehole, it was noted that the drilling process was easy and fast within the depths from 16 and 17.5 m (20 m is the depth of the Pz15) and the samples' yield was less than 50% . This enhances again the occurrence of filtration or leakage at the toe of the dam (Fig. 9). Consequently, the presence of filtration zones or leakage within the clay core body could pose problems on the stability and the safety of the dam in the future. Therefore, a permanent monitoring program is required to ensure the safety of dam particularly at high water storage levels.

4.4. ERT-P4 profile

This profile was implemented at the top of the secondary embankment body and extends along a distance of 535 m which is the length of the secondary embankment (Fig. 2). The geo-electrical section of the ERT-P4 profile is shown in the Fig. 10. The red dotted line represents the lower boundary of the embankment with the natural ground surface in the lake. The embankment body (net blue colour) seems to be clear and homogeneous, and the resistivity values ranges between 20 and 60 Ωm and the thickness is about 10–12 m. The embankment overlays over a layer more resistant, where the resistivity values vary between 200 to 500 Ωm with a thickness reaches more than 30 m. The upper parts of this layer are linked to the alluvial deposits, which are compound of clay, sands and gravels. Whereas, the lower parts of this layer could be associated to the marl and chalky calcareous rocks, which form the bedrock of the secondary embankment of dam depending on the investigations and the geological setting. With regard to the last part of the geo-electrical section, the formations become more resistant and the

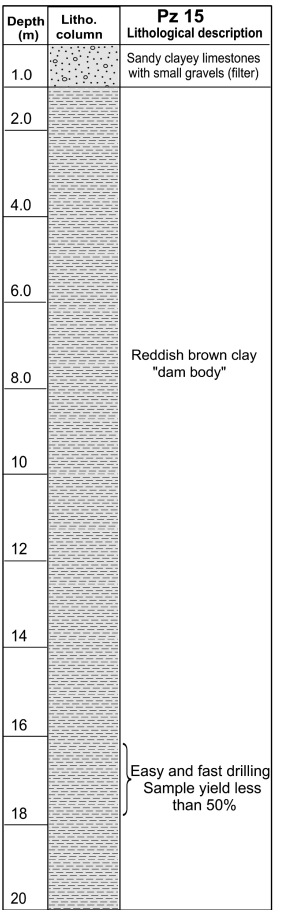

Fig. 9. The piezometric borehole log of Pz15 drilled on the top of the main embankment, which indicates to ease and speed in drilling within the depth 16–17.5 m (modified after the *General Company for Water Studies, 2008*).

resistively reaches more than 2000 Ωm. The high resistivity values are associated with the hard limestone and dolomite rocks, which form the nearby mountain slopes.

The contrast in the resistivity values at the last part of the section (at the distance 400 m of the profile), indicate to the existence of the fault, which separates the marly and chalky limestone formation (200–500 Ωm) and the hard calcareous rocks (2000 Ωm). The trace of this fault is clear in

the attached photo with the ERT section of the profile ERT-P4 (Fig. 10). On the other hand, the difference in the nature of the bedrock of the main embankment (sands and conglomerates) and the secondary embankment (marly and chalky limestone), confirms the presence of this fault on the right shoulder of the lake parallel to the actual main course of Salhab's river.

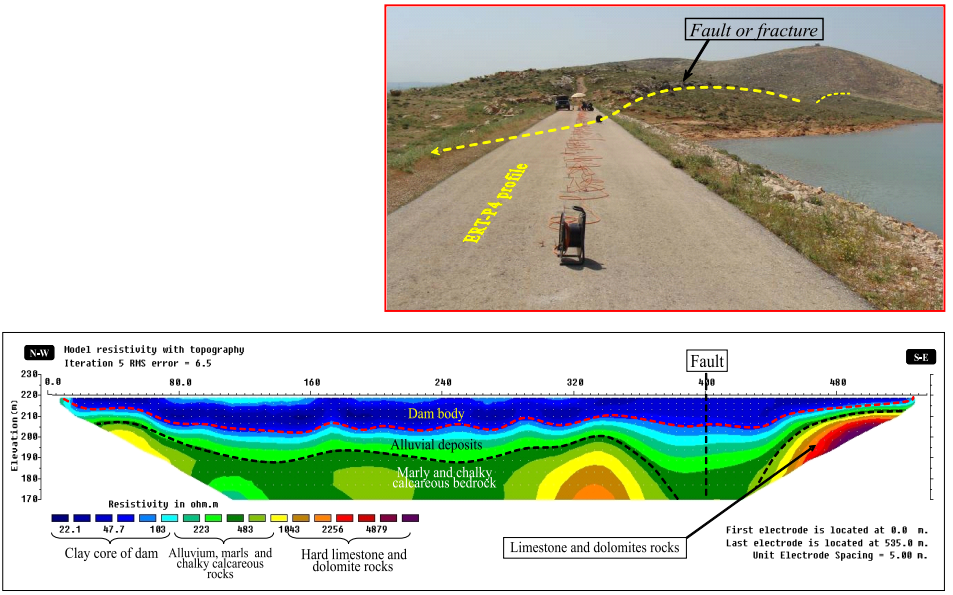

Fig. 10. Interpretation of the ERT profile P4 section carried out at the top of the secondary embankment of Salhab dam, the above photo shows the trace of the detected tectonic fault at the adjacent geological formations to dam body.

5. Conclusion

The interpretation of the Electrical Resistivity Tomography (ERT) sections carried out in Salhab earthen dam confirmed the differences in the subsurface geological structure under the main and secondary embankment bedrocks of the dam, which is due to the effect of a tectonic fault hits the right shoulder of the dam lake.

The interpretation of the ERT section of the profile performed behind the main dam's body revealed two possible leakage zones at the beginning

and end of the profile close to the spillway channel. Whereas, the interpretation of the section ERT profile and the SP measurements carried out at the top and backside of the main embankment, revealed a zone of low resistivity values, extends alone the 350 m distance of the section. This zone includes many probable punctual spots of leakage or filtration, one of these filtration spots explains the presence of water in the piezometric borehole (Pz15) drilled at the top of the dam.

With respect to the ERT section carried out on the top of the secondary embankment, the embankment appears to be homogeneous and impermeable, and the subsurface bedrock does not show any manifestations of leakage or filtration at least within the available investigation depth.

Consequently, it is believed that most of the leakage or outflow processes in Salhab earthen dam occur through the bedrock under the two edges of the main embankment of the dam as well as through the area close to the spillway channel.

Acknowledgements. The author would like to express his thanks and gratitude to Professor I. Othman, Director General of the atomic energy commission of Syria (AECS) for his encouragement and constant support. Thanks are also due to the colleagues in the department of geology for their helps. We gratefully acknowledge the anonymous reviewers for their important comments and suggestions that considerably enhanced the quality of the manuscript.

References

Al-Diab S., 2008: Report of the geophysical investigations executed under the technical conditions proposed by French EDF company to estimate the technical situation of Salhab dam, 44 pp. (internal report).

Al-Fares W., 2014: Application of electrical resistivity tomography technique for characterizing the leakage problem in Abu Baara earth dam, Syria. Int. J. Geophys., Article ID 368128, 9 p., doi: 10.1155/2014/368128.

Al-Fares W., 2011: Contribution of the geophysical methods in characterizing the water leakage in Afamia B dam, Syria. J. Appl. Geophys., **75**, 3, 464–471, doi: 10.1016/j.jappgeo.2011.07.014.

Asfahani J., Radwan Y., Layyous I., 2010: Integrated geophysical and morphotectonic survey of the impact of extensional tectonics on the Qastoon dam, Northwestern Syria. Pure Appl. Geophys., **167**, 3, 323–338, doi: 10.1007/s00024-009-0019-y.

Bedrosian P. A., Burton B. L., Powers M. H., Minsley B. J., Phillips J. D., Hunter L. E., 2012: Geophysical investigations of geology and structure at the Martis Creek Dam, Truckee, California. J. Appl. Geophys., **77**, 7–20, doi: 10.1016/j.jappgeo.2011.11.002.

Brew G. E., 2001: Tectonic evolution of Syria interpreted from integrated geophysical and geological analysis. Ph.D. dissertation at Cornell University, USA, 322 pp.

Cho I.-K., Yeom J.-Y., 2007: Crossline resistivity tomography for the delineation of anomalous seepage pathways in an embankment dam. Geophysics, **72**, 2, 31–38, doi: 10.1190/1.2435200.

Devyatkin E. V., Dodonov A. E., Sharkov E. V., Zykin V. S., Simakova A. N., Khatib K., Nseir H., 1997: The El-Ghab rift depression in Syria: its structure, stratigraphy, and history of development. Stratigr. Geol. Correl., **5**, 4, 362–374.

Foster M. A., Fell R., Davidson R., Wan C. F., 2002: Estimation of the probability of failure of embankment dams by internal erosion and piping using event tree methods. ANCOLD Bulletin, 121, 75–82.

General Company for Water Studies, 2008: Directorate of Investigation, Department of Engineering Geology, Salhab Dam Project 2008, Homs, Syria.

General Establishment for Geology and Mineral Resources, 1984: The geological map of Syria, Misyaf sheet scale 1:50,000. Ministry of Petroleum and Mineral Resources, Damascus, Syria.

Gomez F., Khawlie M., Tabet C., Darkal A. N., Khair K., Barazangi M., 2006: Late Cenozoic uplift along the northern Dead Sea transform in Lebanon and Syria. Earth Planet. Sci. Lett., **241**, 3-4, 913–931, doi: 10.1016/j.epsl.2005.10.029.

Gutiérrez F., Mozafari M., Carbonel D., Gómez R., Raeisi E., 2015: Leakage problems in dams built on evaporites. The case of La Loteta Dam (NE Spain), a reservoir in a large karstic depression generated by interstratal salt dissolution. Eng. Geol., **185**, 139–154, doi: 10.1016/j.enggeo.2014.12.009.

Ikard S. J., Revil A., Schmutz M., Karaoulis M., Jardani A., Mooney M., 2013: Characterization of focused seepage through an earthfill dam using geoelectrical methods. Ground Water, **52**, 6, 952–965 doi: 10.1111/gwat.12151.

Johansson S., Dahlin T., 1996: Seepage monitoring in an earth dam by repeated resistivity measurements. Eur. J. Environ. Eng. Geophys., **1**, 3, 229–247.

Loke M. H., Barker R. D., 1996: Rapid least-square inversion of apparent resistivity pseudo-section by a quasi-Newton method. Geophys. Prospect., **44**, 1, 131–152, doi: 10.1111/j.1365-2478.1996.tb00142.x.

Moore J. R., Boleve A., Sanders J. W., Glaser S. D., 2011: Self-potential investigation of moraine dam seepage. J. Appl. Geophys., **74**, 277–286, doi: 10.1016/j.jappgeo.2011.06.014.

Oh S., Sun C. G., 2008: Combined analysis of electrical resistivity and geotechnical SPT blow counts for the safety assessment of fill dam. Environ. Geol., **54**, 1, 31–42, doi: 10.1007/s00254-007-0790-y.

Omer Kh., Habshiya M., 2008: The geophysical investigations carried out in Salhab dam. General Water Resources Directorate in Damascus (internal report).

Osazuwa I. B., Chii C. E., 2009: A two-dimensional electrical resistivity imaging of an earth dam, Zaria, Nigeria. J. Environ. Hydrol., **17**, 28, 1–8.

Panthulu T. V., Krishnaiah C., Shirke J. M., 2001: Detection of seepage paths in earth dams using self-potential and electrical resistivity methods. Eng. Geol., **59**, 3-4, 281–295, doi: 10.1016/S0013-7952(00)00082-X.

Ponikarov V., 1963: The geological map of Syria, Hama-Latheqieh sheet, scale 1:1200,000, V.O. Technoexport. Ministry of Industry, Damascus, Syria.

Seaton W. J., Burbey T. J., 2002: Evaluation of two-dimensional resistivity methods in a fractured crystalline-rock terrain. J. Appl. Geophys., **51**, 1, 21–41, doi: 10.1016/S0926-9851(02)00212-4.

Sjödahl P., Dahlin T., Zhou B., 2006: 2.5D resistivity modeling of embankment dams to assess influence from geometry and material properties. Geophysics, **71**, 3, 107–114, doi: 10.1190/1.2198217.

Thompson S., Kulessa B., Luckman A., 2012: Integrated electrical resistivity tomography (ERT) and self-potential (SP) techniques for assessing hydrological processes within glacial lake moraine dams. J. Glaciol., **58**, 211, 849–858, doi: 10.3189/2012JoG11J235.

sciendo

Contributions to Geophysics and Geodesy Vol. 49/4, 2019 (459–478)

Characterization of Ar-Rassafeh Badyieh area (Area-2), Syria by using the airborne gamma-ray spectrometric and fractal modelling techniques

Jamal ASFAHANI

Atomic Energy Commission, P.O. Box 6091, Damascus, Syria
e-mail: cscientific@aec.org.sy

Abstract: The available aerial gamma-ray spectrometric data of Ar-Rassafeh Badyieh area (Area-2) are used herein for geological interpretations and mapping purposes. Those data are interpreted by the concentration-number (C-N) fractal modelling technique, with the use of log-log graphs. According to C-N model, different radioactive ranges of TC, eU, eTh, and K have been isolated. Those ranges are thereafter used to characterize the lithological outcrops in the study area. The radioactive signatures of all the outcrops in Area-2 have been discussed and documented through establishing the C-N maps of TC, eU, eTh, and K, and benefiting of the available geological map. The C-N fractal modelling technique proves its efficacy, where radioactive and lithological boundaries of outcrops are in concordance. The case study presented in this paper shows the importance and the role of airborne gamma-ray spectrometric and fractal modelling techniques to support the geological mapping and the interpretations in geological context, particularly when the study region is rugged and difficult to be accessed.

Key words: fractal modelling technique, aerial gamma-ray spectrometry survey, Al-Rassafeh area, Syria

1. Introduction

The airborne gamma-ray spectrometric survey has been essentially oriented towards defining radioactive anomalies related to uranium mineralization (*International Atomic Energy Agency, 1988*). It can also be employed to investigate the other useful minerals and sometimes the subsurface hydrocarbon accumulations (*Selley, 1998*). The gamma-ray spectrometric data have also been applied with variable degrees of success to the mapping of lithological units. The success of such a mapping depends on several factors; the most important one is the contrast in radioelement content between lithological assemblages. The geological mapping is based on the assumption that the absolute and relative concentrations of the radioelements vary measur-

doi: 10.2478/congeo-2019-0024

ably and significantly with lithology. Integrated interpretation, altogether with aerial photograph, satellite imagery and other airborne geophysical data sets, allows exploiting the complementary geological information and enables the radioelement distributions to be studied in a structural geologic and geomorphologic context.

Airborne gamma-ray spectrometry surveying also offers a promising tool for lithofacies mapping of sedimentary basins as evaporates, carbonates, sandstones and shales. Those lithofacies can usually be differentiated in their radioelement content, because clastic sediments often reflect the radioelement compositions of the provenance source materials (*Dickson and Scott, 1997*). *Saunders et al. (1994)* have already defined the typical radioelement concentrations over those mentioned lithofacies and indicated their importance for petroleum exploration.

The statistical factor analysis technique (SFAT) has been recently applied on aerial gamma-ray spectrometric related to the Ar-Rassafeh Badyieh area (Area-2), Syria to establish a lithological scored map (*Asfahani et al., 2018*). This lithological scored map is an important tool for geological mapping and allows the different isolated sectors to be characterized and interpreted geologically and radioactively.

This paper deals with the application of the concentration-number (C-N) fractal modelling technique as a suitable tool to interpret the aerial gamma-ray spectrometric data of Ar-Rassafeh Badyieh area (Area-2), Syria in terms of geological mapping for evaluating with details of the total radioactivity (TC) in Ur, equivalent uranium (eU) in ppm, equivalent thorium (eTh) in ppm, and potassium (K) in % signatures of the outcrop rocks in the study area. The reasons behind using the fractal modelling technique are the weakness and disadvantage points that characterize the traditional statistical techniques. In fact, those conventional techniques based on normal or log-normal distribution do not take into consideration the shape, extent and magnitude of radioactive anomalous areas (*Rafiee, 2005; Afzal et al., 2010*). Moreover, geological and geochemical conditions do not have any influence on the geophysical anomaly separation from background (*Reimann et al., 2005*). Traditional Euclidean geometry cannot consequently explain and examine the natural processes with their different populations, especially geo-related sciences (*Davis, 2002*).

The C-N fractal modelling technique was recently used by *Asfahani (2017)*

to differentiate among different kinds of basalt in Southern Syria through interpreting nuclear and electrical well logging. The same fractal technique was also used to interpret the aerial gamma-ray spectrometric for separating uranium anomalies from background in Area-3, and for characterizing the radioactive heat production of Area-1 (*Asfahani, 2018a, 2018b*).

The Area-2 study region is particularly a very rugged terrain, where we ignore and have only a little information about its geology. A detailed field geological investigations are therefore extremely required. Such needed geological works are not actually an easy task to be carried out in the near future, due to the present Syrian difficult conditions. The aerial gamma-ray spectrometric survey and its available data is therefore a powerful tool, and can be used to characterize geologically the study region and to determine the different radioactive ranges of TC, eU, eTh, and K signatures related to different lithological facies. The application of the aerial gamma-ray spectrometry technique with the C-N fractal modelling technique in the study Area-2 replaces temporarily the field geological works, and remedies consequently the scarcity of geological information of the mentioned region.

2. Object of study

The main objectives of this paper are therefore the following:

1. To interpret the available aerial gamma-ray spectrometry data related to the Area-2 by C-N fractal modelling technique.
2. To isolate different radioactive ranges of TC, eU, eTh, and K, by using the C-N model, and establish the different C-N maps accordingly.
3. To determine the radioactive signatures of the outcrop rocks in the study area for the TC, eU, eTh, and K.
4. To compare the obtained interpretative aerial gamma-ray spectrometry results with the available geological map of the study area to draw definitive conclusions.

3. Area of study

International Atomic Energy Commission and Risø National Laboratory conducted in Syria in 1987 the airborne gamma-ray spectrometric surveys

during SYR/86/005 project (*Risø, 1987; Jubeli, 1990*). Those surveys covered the following areas (Fig. 1a) (*Asfahani et al., 2018*):

1. The Syrian Desert (Area-1) (7189 line km at 4 km line spacing).
2. Ar-Rassafeh Badyieh (Area-2) (2240 line km at 4 km line spacing).
3. The Northern Palmyrides (Area-3) (1600 line km at 3 km line spacing).

The total radiometric TC (Ur) map of the covered three mentioned areas is shown in Fig. 1b (*Asfahani et al., 2018*).

The present paper is oriented towards geological mapping of the outcrop rocks of Ar-Rassafeh Badyieh (Area-2), through determining the different radioactive ranges (TC, eU, eTh, and K) by the application of the C-N fractal modelling technique, that could be used as radioactive signatures for

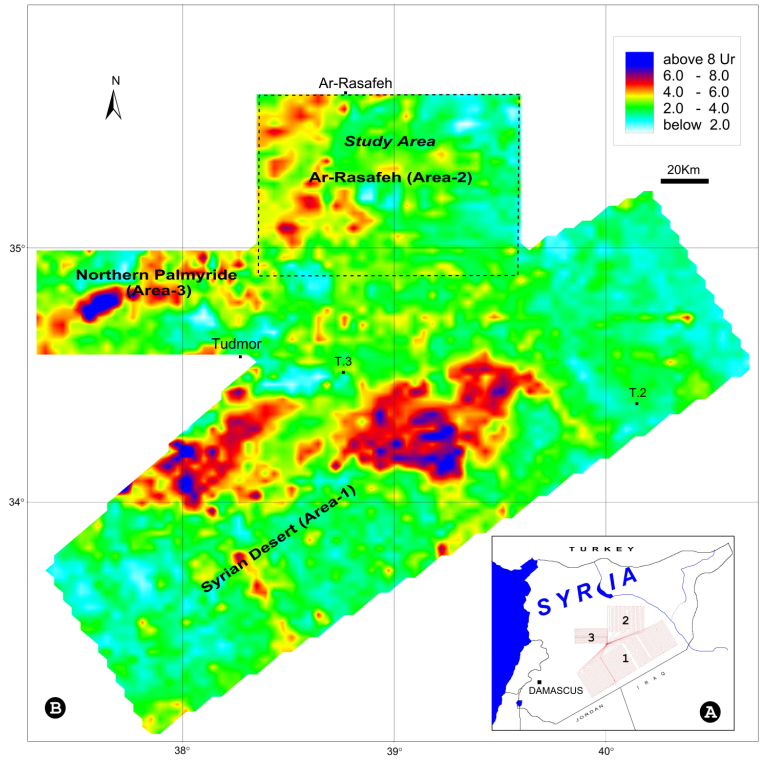

Fig. 1: (a) Total areas covered by the airborne gamma-ray spectrometry technique in Syria. (b) Radiometric map of TC resulting from gamma-ray spectrometric survey.

the lithological outcrop rocks. Fig. 2 shows the geology of the study Area-2 as described by *Asfahani et al. (2018)*. Readers are advised to consult the paper of *Asfahani et al. (2018)* for more geological details about the study region.

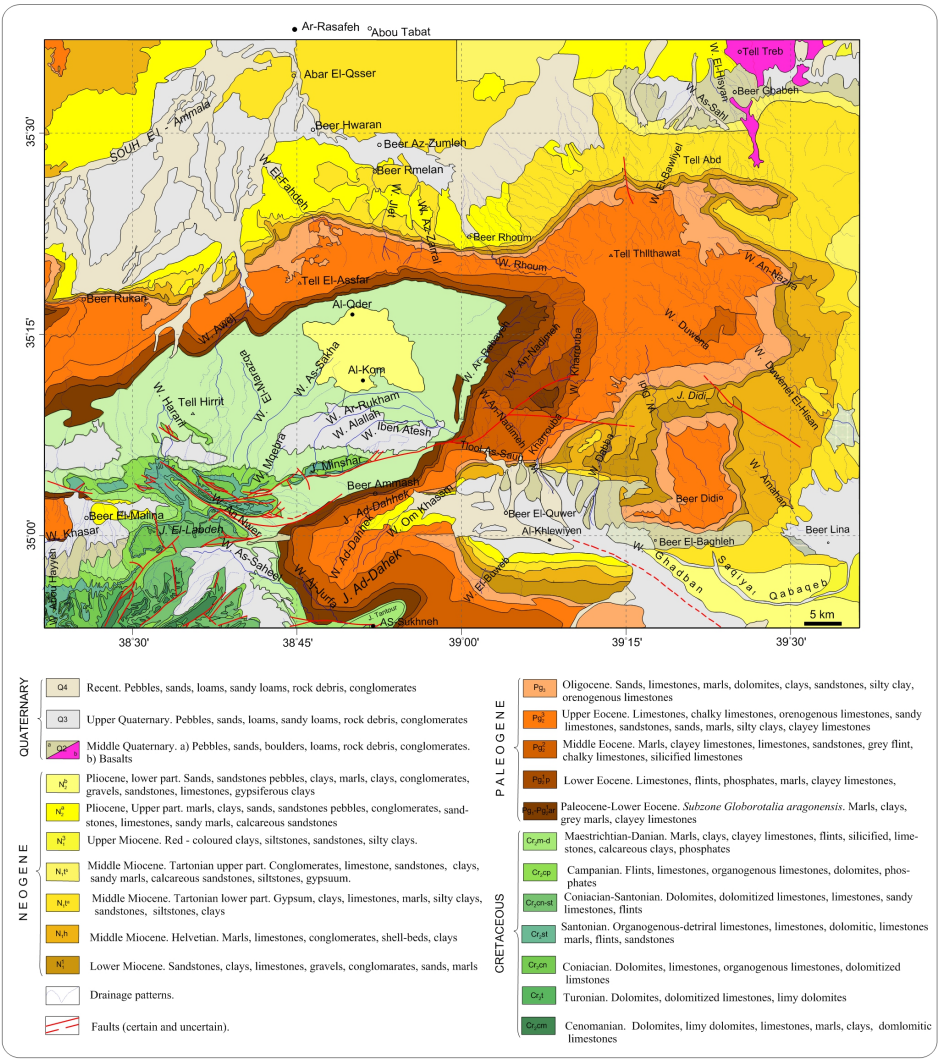

Fig. 2: Geological map of Ar-Rassafeh Badyieh area (Area-2) (*Asfahani et al., 2018*).

4. Methods of study

4.1. Aerial gamma-ray spectrometric technique

An airborne gamma-ray survey was carried out during 1987, over the Ar-Rassafeh Badyieh area (Area-2) situated north of Syrian desert in the region between the northern Palmyrides in the south-west and the Euphrates in the northern and east. Area-2 was covered by 28 north-south oriented aerial survey lines. Those lines are 80 km long, and spaced by 4 km, Fig. 1a. The typical survey speed was of 120 km/hr in a nominal survey, and the height was of 30 meters. A system of a compact, lightweight, four-channel gamma-ray spectrometer, (GAD-6, Scintrex, Canada), with a detector of 12.5 letters NaI(Tl) volume had been used to conduct this aerial survey. The energy windows used in the four-channel gamma-ray spectrometer are shown in Table 1. The system calibration took place at the calibration pads at the Dala airport in Sweden (*Risø, 1987*). An IGI Loran-C navigation system was used to provide efficient flight path control. Potassium, uranium, thorium, and total gamma-ray counts were recorded over one-second intervals and stored on a data tape together with the actual distance to the ground measured with a radar altimeter.

The raw data were corrected for background effects and the applicable interchange, Compton corrections. In addition, the exponential attenuation factors for height corrections were established (*Risø, 1987*).

Table 1. Range of energy with spectral windows used in the airborne survey.

window	airborne radiometric survey (MeV)	dominant radioisotope
potassium	1.38–1.56	K^{40}
uranium	1.66–1.90	Bi^{214}
thorium	2.44–2.77	Tl^{208}
total count	0.40–2.77	–

4.2. Concentration-number (C-N) fractal modelling technique

Fractal geometry is proposed by *Mandelbrot (1983)* to discuss and explain processes in nature. Different fractal analysis methodologies have been al-

ready proposed and applied in different geosciences domains, especially geophysical exploration since 1980s, such as Power Spectrum-Area (S-A; *Cheng et al., 1999*), and Power Spectrum-Volume (S-V; *Afzal et al., 2012; Afzal et al., 2017b*), Concentration-Volume (C-V; *Afzal et al., 2011*), Concentration-Area (C-A; *Cheng et al., 1994*), and Concentration-Number (C-N; *Hassanpour and Afzal, 2013*).

Log-log plots are used while applying fractal models, where the straight line segments fitted the log-log graph have some break threshold points (*Zuo 2011; Wang et al., 2011; Mohammadi et al., 2013*).

The present paper proposes the application of the C-N fractal modelling technique as a suitable tool to interpret the available aerial gamma-ray spectrometric data related to Ar-Rassafeh Badyieh area (Area-2), Syria. This fractal technique is oriented towards isolating different radioactive ranges of TC, eU, eTh and K, and radioactively characterizing the outcrop rocks in term of Area-2 geological mapping.

The superiority of the fractal modelling technique is proven because of using all the available data and considering their spatial relations with each other (*Afzal et al. 2010; Carranza, 2008; Cheng et al., 1994; Hassanpour and Afzal, 2013; Li et al., 2003; Wang et al., 2008; Heidari et al., 2013; Afzal et al., 2011; 2012; 2013; 2016; 2017a,b; Sadeghi et al., 2012; Rahmati et al., 2015; Meigoony et al., 2014; Nazarpour et al., 2015; Cheng 2007; Hosseini et al., 2015*).

The Concentration-Number (C-N) fractal model is expressed by the following equation:

$$N(\geq \rho) = F\rho^{-D}\,, \tag{1}$$

where ρ denotes the treated geophysical parameter values, which are in this case study a total radioactivity (TC), equivalent uranium (eU), equivalent thorium (eTh), and potasium (K%), $N(\geq \rho)$ denotes the cumulative number of the treated geophysical data, which are the cumulative number of total radioactivity (CNTC), the cumulative number of equivalent uranium (CNeU), the cumulative number of equivalent thorium (CNeTh), and the cumulative number of potasium (CNK%), with the geophysical parameter values greater than or equal to ρ, F is a constant and D is the scaling exponent or fractal dimension of the distribution of geophysical parameter values.

5. Results and discussion

The multifractal modelling technique with adapting concentration-number (C-N) model is developed and applied herein to analyse the behaviour of the TC, eU, eTh, and K% parameters in the Area-2. Table 2 represents the main statistical characteristics of TC, eU, eTh, and K%.

Table 2. Statistical characteristics of the radioactive variables in Area-2.

Variable	TC	K (%)	eU (ppm)	eTh (ppm)
Case number	61712	61712	61712	61712
Min	0.23	0.02	0.16	0.16
Max	17	0.85	13.61	9.28
$\bar{X}$	4.55	0.26	1.59	3.39
σ	1.36	0.09	0.95	1.15
CV	29.9	34	59.75	33.9
$\bar{X} + 2\sigma$	7.27	0.44	3.50	5.69

The advantages of using the multifractal modelling technique and its superiority in comparison with the traditional statistical technique are discussed above, which justify its application in such a quantitative interpretation.

The C-N log-log plots are proposed and applied to characterize the four radioactive parameters (TC, eU, eTh and K%) obtained by aerial gamma-ray spectrometry in Area-2. The concept of break point is adapted and used herein as a lithological boundary between different kinds of outcrop rocks to indicate the passage from a specific lithology to another different one.

Log-log plot of $N(\geq \rho)$ versus ρ(TC, eU, eTh and K) shows the straight line segments with the different slopes $-D$ corresponding to different radioactivity intervals. The break points of those line segments are considered as thresholds. The selection of break points as the threshold values appears to be an objective decision due to the different geophysical populations, which are recognized by different segments in the C-N log-log plot. The geophysical populations of those treated parameters are therefore divided and established based on linear segments and break points in the log-log plots.

5.1. Total radioactivity TC (Ur)

Based on the C-N log-log plot shown in Fig. 3, the total radioactivity log (TC) shows four threshold break points C1, C2, C3 and C4 at 0.54, 0.79, 0.94 and 1.05 respectively.

The log (TC) values indicate total radioactivity of 3.47, 6.16, 8.71, and 11.22 Ur respectively. Those four break points correspond to five natural radioactivity ranges as follows: The first range is less than 3.47 Ur, the second range is between 3.47 and 6.16 Ur, the third range is between 6.16 and 8.71 Ur, the fourth range is between 8.71 and 11.22 Ur, and the fifth range is bigger than 11.22 Ur.

According to those five TC natural radioactivity ranges, a map of the TC distributions is established for the study Area-2 region as shown in Fig. 4.

The range of below 3.47 Ur is belonging in some parts of Area-2 to Middle Quaternary of basalts, to Lower Miocene of sandstones, clays, limestones, gravels, conglomerates and sands, and to the Cenonian of dolomites, limy dolomites, marls, clays, and dolomitic limestones. The last range of above 11.20 Ur is removed from interpretation because it represents punctual values. The rest three ranges are therefore important and could be interpreted in lithological context as follows:

– The range of 3.47 to 6.16 Ur represents reef marine calcareous facies that change gradually to continental (Paleogene-Neogene), passing through

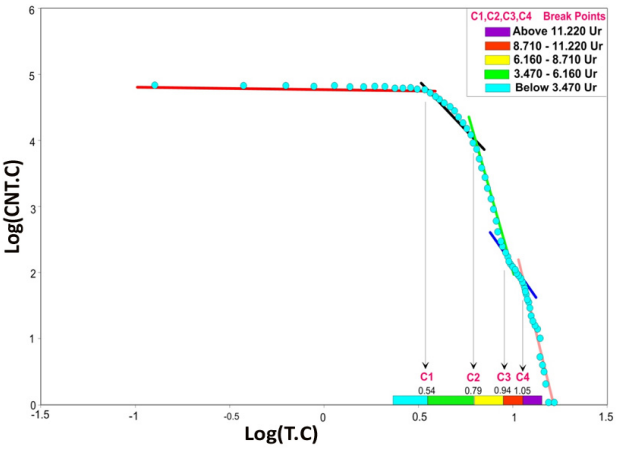

Fig. 3: Log-log plot of total radioactivity TC in the Area-2.

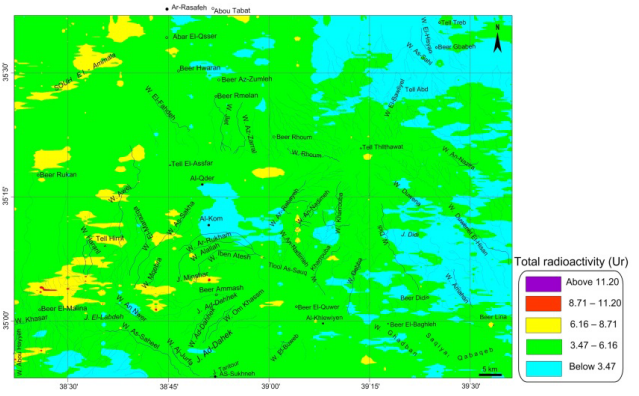

Fig. 4: Natural total radioactivity TC map derived by the C-N fractal modelling in Ar-Rassafeh Badyieh area (Area-2), Syria.

lagoon to coastal facies of sandstones and various sands.

– The range of 6.16 to 8.71Ur represents Quaternary flood surfaces composed of evaporates and alluvium and gathered deposits from the erosion materials of the adjoining rocks, which are usually deposited uncomfortably over the older rocks.
– The range of 8.71 to 11.20 Ur represents Upper Cretaceous rocks outcropping along the faulted zones, which are limestone, calcareous-dolomite and phosphates beds alternating with flints.

5.2. Equivalent uranium eU (ppm)

Based on the C-N log-log plot presented in Fig. 5, the equivalent uranium log (eU) shows also four threshold break points C1, C2, C3, and C4 at 0.22, 0.5, 0.63, and 1 respectively. The log (eU) values indicate an equivalent uranium eU of 1.66, 3.16, 4.26, and 10 respectively. Those four break points correspond to five uranium ranges as follows: The first range is less than 1.66, the second range is between 1.66 and 3.16, the third range is between 3.16 and 4.26, and the fourth range is between 4.26 and 10 and the fifth range is bigger than 10.

According to those five eU ranges, a map of the eU distributions is established for the study Area-2 region as shown in Fig. 6.

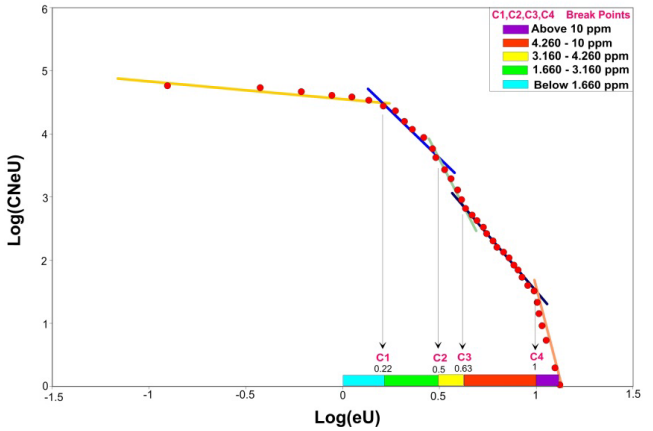

Fig. 5: Log-log plot of eU in the Area-2.

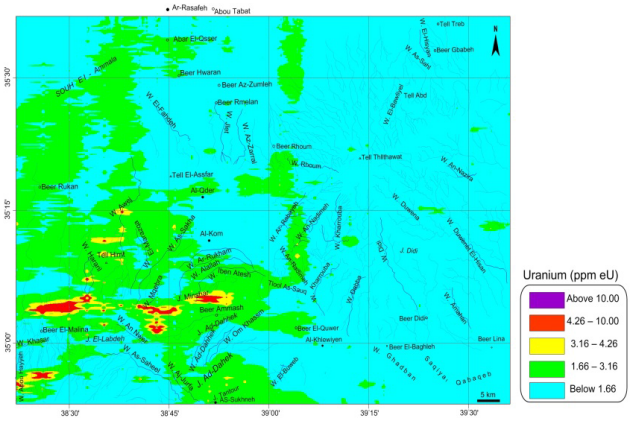

Fig. 6: Equivalent uranium eU map derived by the C-N fractal modelling in Ar-Rassafeh Badyieh area (Area-2), Syria.

The low range of below 1.66 ppm represents the most parts of Area-2. The different ages of Neogene, the Quaternary, and the different ages of Paleogene are characterized by equivalent uranium (eU) of bellow 1.66 ppm. One can match between Fig. 6 and Fig. 2 to follow the geological descriptions of the areas related to this low eU radioactive range. The last range of above 10 ppm is removed from interpretation because it represents punctual values. The rest three ranges are therefore important and could be interpreted in lithological context as follows:

– The range of 1.66 to 3.16 ppm represents surfaces flooding formations that uncomfortably overlie the Cretaceous rocks.
– The range of 3.16 to 4.26 ppm represents Calcareous rocks, phosphates, calcareous dolomites and flints.
– The range of 4.26 to 10 ppm represents Outcropped calcareous phosphates rocks, calcareous, dolomites along the faulted zones (calcareous breccias – alternating with of phosphates and flints).

The eU ranges established by C-N approach and the determined breakpoints indicate an obvious passage from a specific lithology to another different one. The multifractal technique with C-N model is consequently capable to reflect the lithology of the study Area-2, where a strong correspondence and coincidence between both geological and radioactive boundaries exists.

5.3. Equivalent thorium eTh (ppm)

Based on the C-N log-log plot shown in Fig. 7, the equivalent thorium log (eTh) indicates three threshold break points C1, C2, and C3 at 0.342, 0.549 and 0.793 respectively. The log (eTh) values indicate an eTh of 2.20, 3.54, and 6.21 respectively. The three indicated break points correspond to four eTh ranges as follows: The first range is less than 2.20, the second range is between 2.20 and 3.54, the third range is between 3.54 and 6.21, and the fourth range is bigger than 6.21.

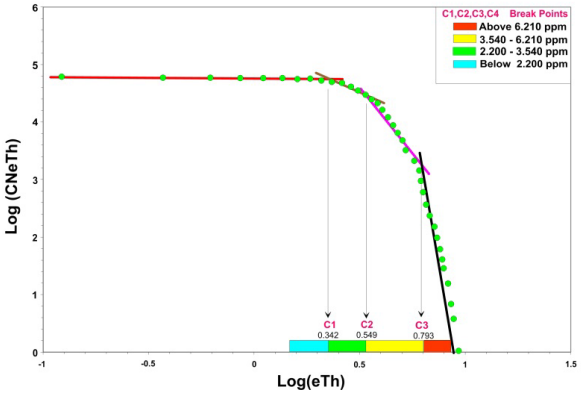

Fig. 7: Log-log plot of eTh in the Area-2.

According to those four eTh ranges, a map of the eTh distributions is established for the study Area-2 region as shown in Fig. 8.

The first range of below 2.20 ppm represents the background. The Cretaceous of Cenomanian and Turonian ages, The Neogene of Pliocene lower part, and Middle and lower Miocene are characterized by eTh of below 2.20 ppm. The matching between Fig. 8 and Fig. 2 allows to follow the geological descriptions of the areas related to this low eTh radioactive range. The rest three ranges are of geological significance and could be interpreted in lithological context as follows:

- The range of 2.20 to 3.54 ppm represents surfaces of tidal formations intervened by some deltaic zones and shallow sub/ littoral continental shelf deposits (sandy limestone, clayey calcareous, and sandy silt).
- The range of 3.54 to 6.21 ppm represents shallow marine deposits dominated by clayey silt facies (calcareous, clays, silt).
- The range of above 6.21 ppm represents in situ formation of terrestrial spotty soil deposits.

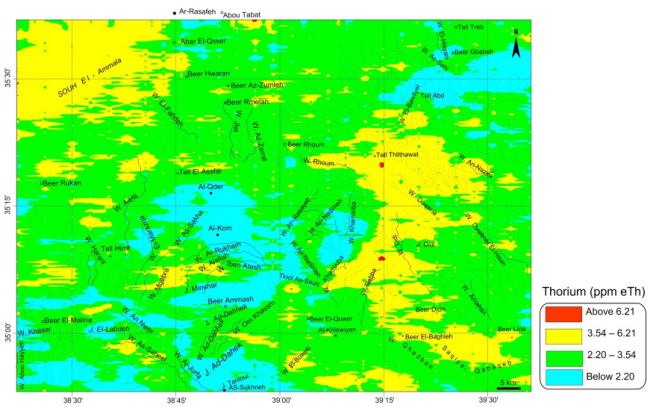

Fig. 8: Equivalent thorium eTh map derived by the C-N fractal modelling in Ar-Rassafeh Badyieh area (Area-2), Syria.

5.4. Potassium K (%)

Based on the C-N log-log plot shown in Fig. 9, the potassium log (K%) indicates four threshold break points C1, C2, C3 and C4 at −0.696, −0.59, −0.347 and −0.15 respectively. The log (K%) values indicate a K% of 0.20,

0.257,0.449 and 0.710 respectively. The above four break points correspond to five K% ranges as follows: The first range is less than 0.20, thesecond range is between 0.20 and 0.257, the third range is between 0.257 and 0.449, the fourth range is between 0.449 and 0.710 and the fifth range is bigger than 0.710.

According to those five K% ranges, a map of the K% distributions is established for the study Area-2 region as shown in Fig. 10.

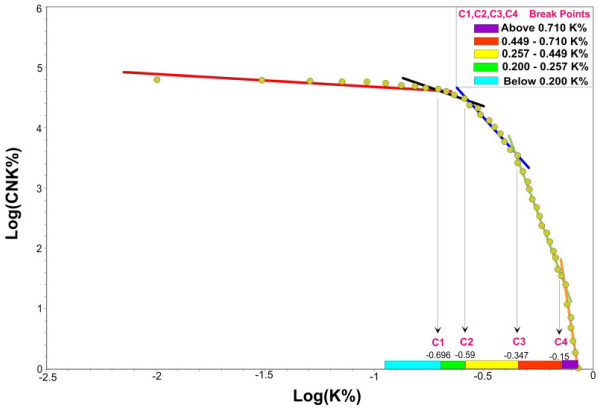

Fig. 9: Log-log plot of K% in the Area-2.

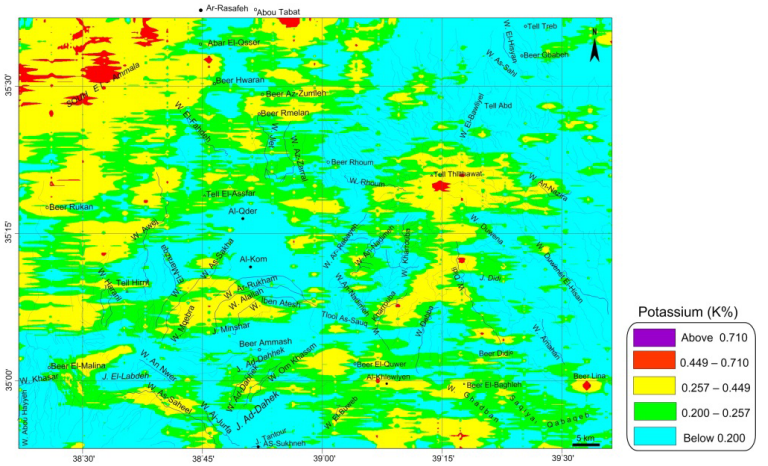

Fig. 10: Potassium K% map derived by the C-N fractal modelling in Ar-Rassafeh Badyieh area (Area-2), Syria.

The first range of below 0.20% represents the background. The Cretaceous of Cenomanian and Turonian ages, the Neogene of lower part age, and the upper Quaternary are characterized by a K% of below 0.20%. The matching between Fig. 10 and Fig. 2 allows to follow the geological descriptions of the areas related to this low K radioactive range. The last range of above 0.7% is removed from interpretation because it represents punctual values. The following three ranges are geologically important, and could be interpreted in lithological context as follows:

- The range of 0.20 to 0.257% represents the boundaries of gradual deposits from Paleocene-Neogene, that are covered by Quaternary formations of floods, conglomerates, evaporates, calcareous dolomites, sandy calcareous and clayey calcareous.
- The range of 0.257 to 0.449% represents shallow marine deposits, marine shelf (Paleocene) that changes gradually to continental deposits (Neogene), passing throughout lagoon and tidal facies of marl, silty clay, calcareous clayey, calcareous sandy, and sands.
- The range of 0.449 to 0.710% represents marine deposits (Paleogene) that are dominated by calcareous clays and sandy clays.

The log-log accumulative distributions presented and documented for the four studied parameters (TC, eU, eTh, and K%), (Figs. 3, 5, 7, and 9) show clearly the different line segments, characterized each by a specific slope. Each line segment presents an isolated radioactive level, and reflects a specific lithological outcrops.

The breakpoints shown in the different log-log of the studied parameters represent in this specific C-N multi fractal modelling application a kind of radioactivity boundaries and indicate the passage from radioactive lithological level to another different one. Each radioactive level reflects a distinguished lithological process and is strongly attached to a specific outcrop rocks. This observed and clear attachment between lithology and radioactivity is one of the advantages of the multifractal C-N approach applied in this research.

The case study presented in this paper obviously shows an example of the role of airborne gamma-ray spectrometric survey in geological mapping, by supporting and providing with additional geological knowledge, particularly in the rugged geology. The C-N fractal modelling technique is also a smart powerful tool to interpret the airborne gamma-ray spectrometric

data, where the different outcrops and lithologies in the study region are well differentiated.

6. Comparison between the statistical factor analysis technique (SFAT) and (C-N) fractal modelling technique

The two mentioned techniques (SFAT) and (C-N) are completely different from mathematically point of view. However, the combination of their results largely contributes in better understanding the geology of the study region, particularly in the rugged and complex geology, such as the case study of Area-2.

The SFAT applied already in a previous research is essentially based on determining the main rotated factors that could be interpreted geologically. SFAT is oriented towards transferring basically the geological map of the study region to a lithological scored map as done by *Asfahani et al. (2018)*. The resulting lithological scored map contained nine different lithological units, that were described and characterized according to different determined factors F1, F2, and F3 (*Asfahani et al., 2018*). The results obtained by this SFAT technique allow a reasonable geological interpretation to be done through understanding the mutual relations among the different lithological scored units.

The fractal C-N technique applied in this paper is differently oriented towards dealing only with the available original radioactive maps of TC, eU, eTh, and K% to determine the radioactive ranges for every studied parameter. It is essentially based on the threshold break points concept. The determination of those break points on the log-log graphs is essential for the subsequent determination of different radioactive ranges that are used to establish the different radioactive maps accordingly. Each determined radioactive range for (TC, eU, eTh, and K%) reflects a specific geology as documented and discussed in this paper. Each available original radioactive map (TC, eU, eTh, and K%) is separately treated and interpreted by the C-N technique as described above.

The different results obtained in this paper by applying the fractal C-N modelling technique are therefore original and new in comparison with those already obtained by application of the SFAT technique (*Asfahani et al., 2018*).

7. Conclusion

The C-N fractal modelling technique is applied in this paper to interpret the aerial gamma-ray spectrometric data of Area-2 in Syria. Different radioactive ranges of TC, eU, eTh, and K have been isolated, and used to characterize the lithological outcrops in the study area. The radioactive signatures of all the outcrops in Area-2 have been determined and geologically interpreted through establishing the C-N maps of TC, eU, eTh, and K. The radioactive break points accurately and precisely determined in this paper by the C-N model efficacy serve as lithological boundaries between different kinds of rocks, and indicate the passage from a specific lithology to another different one. The new different derived radioactive ranges of (TC, eU, eTh, and K) obtained by the C-N technique reflect each a specific geology as documented and discussed in this paper. Those ranges will be used as a helpful tool and a smart guide for sampling rocks and for future detailed geological exploration surveys in the study area. The obvious role of the airborne gamma-ray spectrometric and fractal modelling techniques in geological mapping is demonstrated herein through the case study presented in this paper. Those two techniques support the geological mapping and the interpretations in geological context, particularly when the study region is rugged and difficult to be accessed. The acquired knowledge of this paper will be potentially employed later, when detailed geological and geochemical mining investigations are lanced for radiometric and other useful elements prospecting.

Acknowledgements. With a courteous permission of Dr. I. Othman, General Director of Syrian Atomic Energy Commission to publish this paper and thanks to the anonymous reviewers and the editorial board of CGG journal for their critics, remarks and suggestions they have considerably improved the final version of this paper. As well as thank you belongs to Dr. Igor Kohút, the technical editor of CGG for his collaboration during the handling of this paper.

References

Afzal P., Khakzad A., Moarefvand P., Rashidnejad Omran N., Esfandiari B., Fadakar Alghalandis Y., 2010: Geochemical anomaly separation by multifractal modeling in Kahang (Gor Gor) porphyry system, Central Iran. J. Geochem. Explor., **104**, 1-2, 34–46, doi: 10.1016/j.gexplo.2009.11.003.

Afzal P., Fadakar Alghalandis Y., Khakzad A., Moarefvand P., Rashidnejad Omran N., 2011: Delineation of mineralization zones in porphyry Cu deposits by fractal concentration–volume modeling. J. Geochem. Explor., **108**, 3, 220–232, doi: 10.1016/j.gexplo.2011.03.005.

Afzal P., Zia Zarifi A., Bijan Yasrebi A., 2012: Identification of uranium targets based on airborne radiometric data analysis by using multifractal modeling, Tark and Avanligh 1:50000 sheets, NW Iran. Nonlinear Process. Geophys., **19**, 283–289, doi: 10.5194/npg-19-283-2012.

Afzal P., Dadashzadeh Ahari H., Rashidnejad Omran N., Aliyari F., 2013: Delineation of gold mineralized zones using concentration–volume fractal model in Qolqoleh gold deposit, NW Iran. Ore Geol. Rev., **55**, 125–133, doi: 10.1016/j.oregeorev.2013.05.005.

Afzal P., Mirzaei M., Yousefi M., Adib A., Khalajmasoumi M., Zia Zarifi A., Foster P., Yasrebi A. B., 2016: Delineation of geochemical anomalies based on stream sediment data utilizing fractal modeling and staged factor analysis. J. Afr. Earth Sci., **119**, 139–149, doi: 10.1016/j.jafrearsci.2016.03.009.

Afzal P., Ahmadi K., Rahbar K., 2017a: Application of fractal-wavelet analysis for separation of geochemical anomalies. J. Afr. Earth Sci., **128**, 27–36, doi: 10.1016/j.jafrearsci.2016.08.017.

Afzal P., Heidari S M., Ghaderi M., Yasrebi A. B., 2017b: Determination of mineralization stages using correlation between geochemical fractal modeling and geological data in Arabshah sedimentary rock-hosted epithermal gold deposit, NW Iran. Ore Geol. Rev., **91**, 278–295, doi: 10.1016/j.oregeorev.2017.09.021.

Asfahani J., 2017: Fractal theory modeling for interpreting nuclear and electrical well logging data and establishing lithological cross section in basaltic environment (case study from southern Syria). Appl. Radiat. Isot., **123**, 26–31, doi: 10.1016/j.apradiso.2017.02.020.

Asfahani J., 2018a: Multifractal approach for delineating uranium anomalies related to phosphatic deposits in Area-3, Northern Palmyrides, Syria. Applied Radiation and Isotopes, **137**, 225–235, doi: 10.1016/j.apradiso.2018.03.012.

Asfahani J., 2018b: Estimating and mapping radioactive heat production by using aerial spectrometric gamma and fractal modeling techniques in Syrian desert (Area-1), Syria. Appl. Radiat. Isot., **142**, 194–202, doi: 10.1016/j.apradiso.2018.09.004.

Asfahani J., Al-Hent R., Aissa M., 2018: Radioactive characterization of Ar-Rassafeh Badyieh area (Area-2), Syria by using statistical factor analysis technique. Contrib. Geophys. Geod., **48**, 2, 113–132, doi: 10.2478/congeo-2018-0004.

Carranza E. J. M., 2008: Geochemical anomaly and mineral prospectivity mapping in GIS, handbook of exploration and environmental geochemistry. Vol. 11, Elsevier, Amsterdam, 368 p., eBook ISBN: 9780080930312, hardcover ISBN: 9780444513250.

Cheng Q., Agterberg F. P., Ballantyne S. B., 1994: The separation of geochemical anomalies from background by fractal methods. J. Geochem. Explor., **51**, 2, 109–130, doi: 10.1016/0375-6742(94)90013-2.

Cheng Q., Xu Y., Grunsky E., 1999: Integrated spatial and spectral analysis for geochemical anomaly separation. In: Lippard S. J., Naess A., Sinding-Larsen R., (Eds.):

Proc. of the Fifth Annual Conference of the International Association for Mathematical Geology, Trondheim, Norway, 6-11th August 1999, Vol. 1, 87–92.

Cheng Q., 2007: Multifractal imaging filtering and decomposition methods in space, Fourier frequency, and eigen domains. Nonlinear Process. Geophys., **14**, 3, 293–303, doi: 10.5194/npg-14-293-2007.

Davis J. C., 2002: Statistics and data analysis in geology, 3rd ed. John Wiley & Sons Inc., New York, 656 p.

Dickson B. L., Scott K. M., 1997: Interpretation of aerial gamma ray surveys–adding the geochemical factors. AGSO J. Aust. Geol. Geophys., **17**, 2, 187–200.

Jubeli Y. M., 1990: Uranium exploration in Syria SY/86/005, Final report; Atomic Energy Commission of Syria, Damascus.

Hassanpour S., Afzal P., 2013: Application of concentration-number (C-N) multifractal modelling for geochemical anomaly separation in Haftcheshmeh porphyry system, NW Iran. Arab. J. Geosci., **6**, 3, 957–970, doi: 10.1007/s12517-011-0396-2.

Heidari S. M., Ghaderi M., Afzal P., 2013: Delineating mineralized phases based on lithogeochemical data using multifractal model in Touzlar epithermal Au-Ag (Cu) deposit, NW Iran. Appl. Geochem., **31**, 119–132, doi: 10.1016/j.apgeochem.2012.12.014.

Hosseini S. A., Afzal P., Sadeghi B., Sharmad T., Shahrokhi S. V., Farhadinejad T., 2015: Prospection of Au mineralization based on stream sediments and lithogeochemical data using multifractal modeling in Alut 1:100,000 sheets, NW Iran. Arab. J. Geosci., **8**, 6, 3867–3879 doi: 10.1007/s12517-014-1436-5.

International Atomic Energy Agency, 1988: Geochemical exploration for uranium. Technical Report Series 284, IAEA, Vienna, 97 p.

Li C., Ma T., Shi J., 2003: Application of a fractal method relating concentrations and distances for separation of geochemical anomalies from background. J. Geochem. Explor., **77**, 2-3, 167–175, doi: 10.1016/S0375-6742(02)00276-5.

Mandelbrot B. B., 1983: The Fractal Geometry of Nature, W. H. Freeman, San Francisco, 468 pp.

Meigoony M. S., Afzal P., Gholinejad M., Yasrebi A. B., Sadeghi B., 2014: Delineation of geochemical anomalies using factor analysis and multifractal modeling based on stream sediments data in Sarajeh 1:100,000 sheet, Central Iran. Arab. J. Geosci., **7**, 12, 5333–5343, doi: 10.1007/s12517-013-1074-3.

Mohammadi A., Khakzad A., Rashidnejad Omran N., Mahvi M. R., Moarefvand P., Afzal P., 2013: Application of number–size (N-S) fractal model for separation of mineralized zones in Dareh-Ashki gold deposit, Muteh Complex, Central Iran. Arab. J. Geosci., **6**, 11, 4387–4398, doi: 10.1007/s12517-012-0662-y.

Nazarpour A., Omran N. R., Paydar G. R., 2015: Application of multifractal models to identify geochemical anomalies in Zarshuran Au deposit, NW Iran. Arab. J. Geosci., **8**, 2, 877–889, doi: 10.1007/s12517-013-1183-z.

Rahmati A., Afzal P., Abrishamifar S. A., Sadeghi B., 2015: Application of concentration-number and concentration-volume fractal models to delineate mineralized zones in the Sheytoor iron deposit, Central Iran. Arab. J. Geosci., **8**, 5, 2953–2965, doi: 10.1007/s12517-014-1330-1.

Rafiee A., 2005: Separating geochemical anomalies in stream sediment media by applying combination of fractal concentration area model and multivariate analysis (Case study: Jeal-e-Barez 1:100,000 Sheet,Iran), 20th World Mining Congress Proceeding, Iran, 461–470.

Reimann C., Filzmoser P., Garrett R. G., 2005: Background and threshold: critical comparison of methods of determination. Sci. Total Environ., **346**, 1-3, 1–16, doi: 10.1016/j.scitotenv.2004.11.023.

Risø, 1987: Aerial gamma-ray survey in Syria. Uranium exploration in Syria. SYR/87/005, Technical report, Risø DTU National Laboratory for Sustainable Energy, Roskilde, Denmark.

Sadeghi B., Moarefvand P., Afzal P., Yasrebi A. B., Saein L. D., 2012: Application of fractal models to outline mineralized zones in the Zaghia iron ore deposit, Central Iran. J. Geochem. Explor., Special Issue "Fractal/Multifractal Modelling of Geochemical Data", **122**, 9–19, doi: 10.1016/j.gexplo.2012.04.011.

Saunders D. F., Branch J. F., Thomson C. K., 1994: Tests of Australian aerial radiometric data for use in petroleum reconnaissance. Geophysics, **59**, 3, 411–419, doi: 10.1190/1.1443603.

Selley R. C., 1998: Elements of petroleum geology, 2nd ed. Book, Academic Press, chapter 3: Methods of exploration.

Wang Z., Cheng Q., Xu D., Dong Y., 2008: Fractal modeling of sphalerite banding in Jinding Pb-Zn deposit, Yunnan, Southwestern. China. J. China Univ. Geosci., **19,** 1, 77–84, doi: 10.1016/S1002-0705(08)60027-8.

Wang Q. F., Deng J., Liu H., Wang Y., Sun X., Wan L., 2011: Fractal models for estimating local reserves with different mineralization qualities and spatial variations. J. Geochem. Explor., **108**, 3, 196–208, doi: 10.1016/j.gexplo.2011.02.008.

Zuo R., 2011: Decomposing of mixed pattern of arsenic using fractal model in Gangdese belt, Tibet, China. Appl. Geochem., **26**, Supplement, S271–S273, doi: 10.1016/j.apgeochem.2011.03.122.

sciendo

Contributions to Geophysics and Geodesy Vol. 49/4, 2019 (479–496)

Effective combination of microgravimetry and geoelectrical methods in the detection of subsurface cavities in archaeological prospection – selected case-studies from Slovakia

Roman PAŠTEKA[1,*], David KUŠNIRÁK[1,5], Dennis WILKEN[2], René PUTIŠKA[1], Juraj PAPČO[3], Dominika GODOVÁ[4], Ivan ZVARA[1], Ema NOGOVÁ[1], Lenka ONDRÁŠOVÁ[1]

[1] Department of Applied and Environmental Geophysics, Faculty of Natural Sciences, Comenius University, Mlynská dolina, Ilkovičova 6, 842 48 Bratislava, Slovak Republic

[2] Department of Geophysics, Institute for Geosciences, Christian-Albrechts University, Otto-Hahn-Platz 1, 24118 Kiel, Germany

[3] Department of Theoretical Geodesy, Faculty of Civil Engineering, Slovak University of Technology, Radlinského 11, 810 05 Bratislava, Slovak Republic

[4] Division of Geophysics, Earth Science Institute of the Slovak Academy of Sciences, Dúbravská cesta 9, 840 05 Bratislava, Slovak Republic

[5] GEODATA Group, Hans-Kudlich-Straße 28, 8700 Leoben, Austria

Abstract: This contribution is focused on a common utilization of microgravimetry (very precise and detailed gravimetry) and geoeletrical methods (ground penetrating radar and electric resistivity tomography) in the detection of subsurface cavities in non-destructive archaeological prospection. Both methods can separately detect such kind of subsurface objects, but their complementary and at the same time an eliminating aspect can be very helpful in the interpretation of archaeogeophysical datasets. These properties were shown in various published case-studies. Here we present some more typical examples. Beside this, we present here for a first time an application of the electric resistivity tomography in the interior of a building (a church) in Slovakia. We also demonstrate an example with an extremely small acquisition step in microgravity as a trial for the detection of cavities with very small dimensions – in this case small separated spaces for coffins as a part of the detected crypt (so called columbarium). Unfortunately, these cavities were too small to be reliably detected by the microgravity method. We have tried the well-known 3D Euler deconvolution method to obtain usable depth estimates from the acquired anomalous gravity field. Results from this method were in the majority of cases plausible (sometimes little bit too shallow), when compared with the results from the ground penetrating radar.

*corresponding author: e-mail: roman.pasteka@uniba.sk

doi: 10.2478/congeo-2019-0025

In one selected example, the 3D Euler solutions were too deep and in the present stage of study we cannot well explain this situation. In general, all presented results support an important role of common combination of several geophysical methods, when searching for subsurface cavities in non-destructive archaeological prospection.

Key words: archaeogeophysics, non-destructive prospecting methods, detection, interpretation

1. Introduction

Geophysical methods build an important and fundamental part of non-destructive detection methods in archaeological prospection (e.g. *Clark, 1990; Gaffney and Gater, 2003; Linford, 2006*). For the detection of subsurface cavities (large graves, tombs, crypts, cellars etc.), mainly geoelectrical methods have been and are commonly used. Among them, especially the GPR (Ground Penetrating Radar) and ERT (Electric Resistivity Tomography) can very well recognize subsurface cavities due to their intensive differences in geoelectrical properties to the subsurface. Since the air filled cavity gives a very distinct contrast of the physical parameters, either the relative dielectric permittivity or the conductivity. There were published several successful studies of this kind of application (e.g. *Leucci, 2006; Negri and Leucci, 2006; Cataldo et al., 2012; Zieliński et al., 2019*). Among other geophysical methods mainly the detailed and precise gravimetry (microgravimetry or microgravity method) proves high level of confidence in subsurface cavities detection. Cavities (hollow spaces) show intensive contrast in the density – even when these are filled by debris and/or water. There exist several examples of microgravimetric detection of subsurface cavities in non-destructive archaeological prospection (e.g. *Blížkovský, 1979; Lakshmanan and Montlucon, 1987; Slepak, 1997; Pašteka and Zahorec, 2000; Mrlina et al., 2005; Padín et al., 2012; Sarlak and Aghajani, 2017*). Very effective is the combination of geoelectrical and microgravimetric methods for cavities detection – there were published several examples of this combination in archaeological prospection (*Pašteka et al., 2007, Panisova et al., 2012, 2013, 2016* and others). Mainly the combination of GPR and microgravimetry appears to be very efficient and balanced combination – cavities are presented in 2D vertical GPR section with strong diffraction waves on the top of the cavity, in horizontal GPR sections as intensive re-

flecting anomalies and in incomplete Bouguer anomalies maps as dominant minima (gravity lows) with negative amplitudes of several tens of μGals ($1\,\mu\text{Gal} = 10^{-8}\,\text{m/s}^2$).

In our contribution we would like to summarize results and experiences of our research in this area and demonstrate on the showed case-studies the properties and limits of the use of microgravimetric and geoelectrical methods in subsurface cavities detection. We show and discuss here results obtained at three sites in Slovakia (interiors of three churches), where we have applied the discussed geophysical methods. For the realisation of GPR measurements, we have used the GSSI SIR-3000 equipment with 400 MHz antenna and for ERT measurements an automated multielectrode system ARES manufactured by GF-Instruments has been utilized. Microgravity data acquisition was realised by means of multiple Scintrex CG-5 Autograv instruments, necessary geodetic work (determination of heights) has been done using a simple optical levelling instrument GEO Fennel No. 10. For the quantitative interpretation of microgravimetric data we have used the well-known 3D Euler deconvolution method (*Reid et al., 1990; Pašteka et al., 2009*), which gave us in two cases acceptable results and in one case a controversial depth estimate.

We show here also the first trial of the use of the ERT method in an interior of a building (church) and we also show an example of very detailed microgravimetric research for the detection of separated spaces for coffins in a crypt (testing an acquisition step of 0.2 m).

2. First case-study: microgravimetric and GPR research of the interior of St. Mary's church in Dolné Dubové, SW Slovakia

This research was realised pursuant to the local authority demand and the main aim was detection of old architectonic features in the exterior and interior of the St. Mary's church in Dolné Dubové, a small village in SW Slovakia. Important phase of this survey was realized inside the church, mostly in a part of the aisle and in the presbytery (Fig. 1). GPR survey was realized with a 400 MHz antenna on a set of acquisition lines, separated 30 cm from each other. Acquired data were processed in the ReflexW software (*Sandmeier, 2019*). Main processing steps comprised: subtraction of

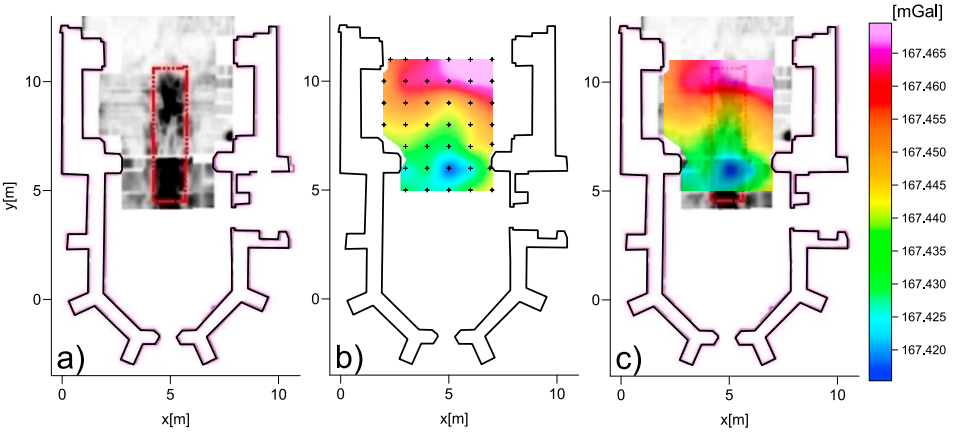

Fig. 1. Results from the GPR and microgravity method from the interior of St. Mary's church in Dolné Dubové, SW Slovakia. a) Horizontal GPR reflection map for the penetration depth of 90 cm, red dotted rectangle shows strongest reflection amplitude anomaly. b) Coloured image map of incomplete Bouguer anomalies for the correction density $2.0\,\mathrm{g/cm^3}$ (blue colour detects the minimum of the anomalous field); small crosses represent positions of gravity acquisition points. c) Common figure of both geophysical fields with transparent map of incomplete Bouguer anomalies.

the mean value (dewow), correction of the start-time, bandpass frequency filtering, gain adjustment, background removal and interpolation of the 2D radargrams into a 3D model. Results were displayed in a form of horizontal reflection amplitude maps for different penetration depths (example for the depth 90 cm is displayed in Fig. 1a, c). Microgravity data acquisition was realized in a net of points 1×1 m by means of a Scintrex CG-5 gravimeter (serial number 155). Acquired data we processed in the usual way for micogravity surveys (e.g. *Pašteka et al., 2007; Panisova et al., 2012*): instrument drift correction, recalculation to base-point value (to a selected relative value), free-air and planar Bouguer corrections, building effects calculation and interpolation into horizontal maps of incomplete Bouguer anomalies. Correction for the gravity effect of the building (building effects calculation) was realized by means of an approximation of set of 3D vertical prisms with polynomial footprint (*Cady, 1980; Potent modelling software User's guide, 2019*). Results were displayed in a form of incomplete Bouguer anomalies map for the correction density $2.0\,\mathrm{g/cm^3}$ (Fig. 1b, c). Acquired area by means of microgravimetry was smaller than that by the GPR

method (Fig. 1) due to limited time-schedule for its realisation in the field.

In the results from the GPR method (horizontal amplitude sections) the most important reflection amplitude anomaly from a detected large object has an approximate rectangular shape and it is positioned in a typical place for a crypt – in the central part of the aisle and its transition to the presbytery (red dotted rectangle in Fig. 1a). It can be split in two parts – a possible entering corridor and the main room of the crypt. Both parts start to be manifested at depths of approx. 0.5 m and continue down to approx. 2 m. In the incomplete Bouguer anomalies map (Fig. 1b, c) the detected cavity (crypt) is demonstrated by a well-developed local minimum

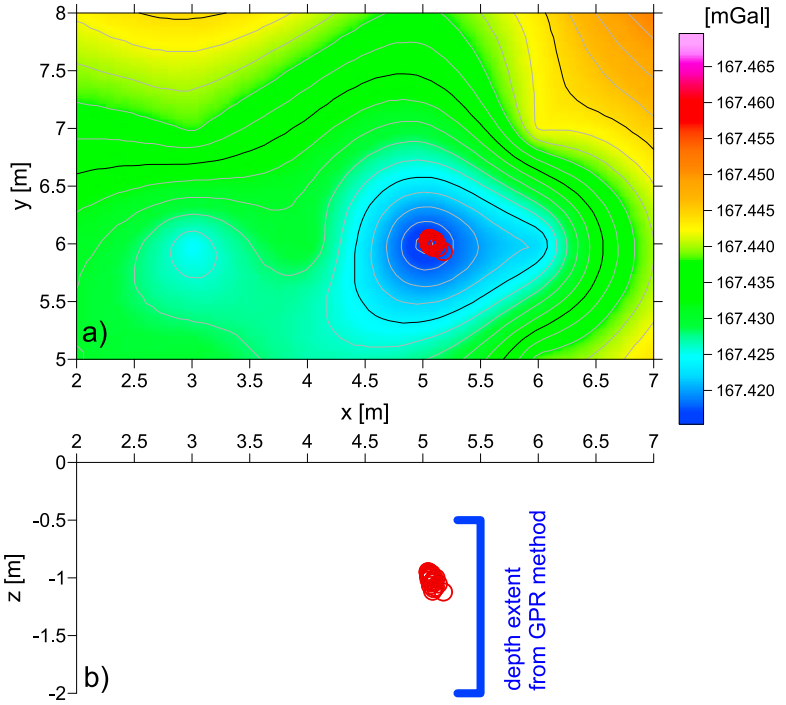

Fig. 2. Results from the 3D Euler deconvolution method, applied on the important negative anomaly from the microgravimetry (interior of St. Mary's church in Dolné Dubové). Used structural index value was $N = 2$ (centre of a sphere in gravimetry). a) Planar visualisation of the result – cluster of the Euler depth solutions is concentrated in the centre of the anomaly, b) vertical section with the displayed cluster of Euler depth solutions (average depth = 1 m). Depth extent (vertical interval) of the detected crypt from the GPR method was: approx. 0.5–2 m (thick blue segment line in the vertical section).

with an amplitude of approx. $-40\,\mu$Gals over the lower part of the cavity, detected by the GPR method (local coordinates of the centre: $x = 5$ m, $y = 6$ m). The upper part of the GPR anomaly (for higher values of the coordinate y) is demonstrated only by a weak bending of the contours of the anomalous gravity field. This could correspond to a cavity with smaller dimensions – maybe a corridor to the main crypt, which is positioned in the bottom part of the figure. Depth estimation of the source depth, realized by means of the 3D Euler deconvolution method (*Reid et al., 1990*) incorporating so called regularized derivatives (*Pašteka et al., 2009*) gives a cluster of depth-solutions (Fig. 2) with an average depth of approx. 1 m. This should give approximately the depth of the centre of the cavity. This result is little bit shallower in comparison with the result from the GPR method (approx. 1.5 m). Our experiences from the applications of the 3D Euler deconvolution method are consistent with this result (*Pašteka et al., 2011*). This crypt was not verified by means of any archaeological excavation or video-inspection.

3. Second case-study: microgravimetric, ERT and GPR research of the interior of St. Catherine's church in Banská Štiavnica, central Slovakia

Based on a discussion with local historians and local cultural heritage experts, a complex geophysical survey was realized in the frame of several international geophysical summer schools in collaboration with the Department of Geophysics, Institute of Geosciences, Christian-Albrechts University in Kiel, Germany. The major part of the aisle and a part of the presbytery (beside the places with large wooden banks) was covered by GPR and microgravity measurements. Gravity measurements could be realized also in the close vicinity of the altar, GPR measurements unfortunately not (this is the reason, why these two methods do not cover identical areas, Fig. 3). Used instruments, data acquisition and processing methods were identical with that, described in the previous case-study. For this publication we have selected the most important part of the church – the transition between the aisle and the presbytery (Fig. 3), where both main methods (GPR and microgravity) detected an important cavity, with high probability a crypt. In the horizontal reflection amplitude section from the GPR method it is

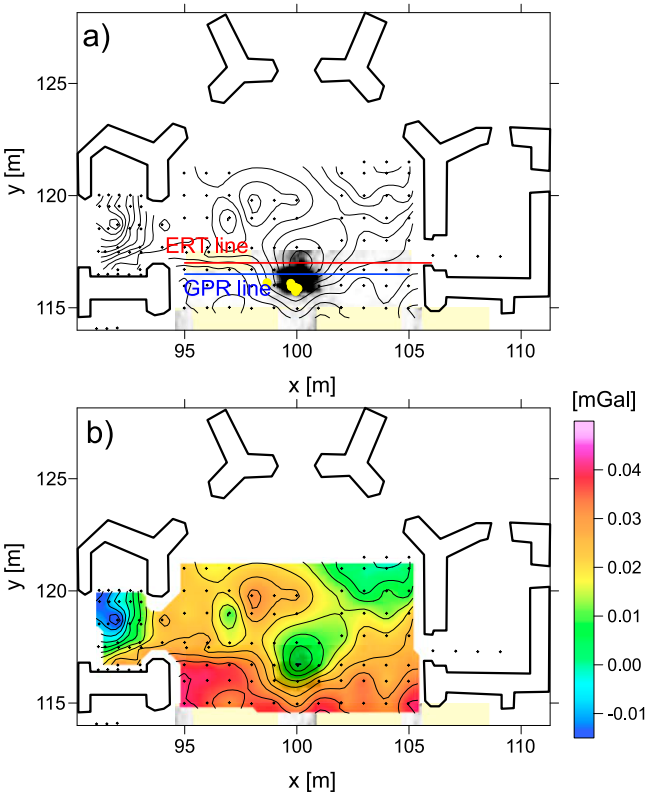

Fig. 3. Results from the GPR and microgravity method from the presbytery of St. Catherine's church in Banská Štiavnica, central Slovakia. a) Horizontal reflection amplitude map for the penetration depth of 50 cm together with contours of incomplete Bouguer anomalies. Red line segment shows the position of the realized ERT section inside the church, blue segment line is the position of selected vertical GPR section, showed in Fig. 5b. Yellow circles show positions of depth solutions, received from 3D Euler deconvolution method. b) Coloured contour image map of incomplete Bouguer anomalies for the correction density 2.0 g/cm^3 (in a medium transparent version).

characterized by a dominant symmetric anomaly in the centre of the figure (Fig. 3a). The anomalous gravity field (incomplete Bouguer anomalies for the correction density 2.0 g/cm^3) show a relatively complicated character – beside the central anomaly over the cavity of interest, there are also two intensive lows (negative anomalies) on the edges of the acquired area. These are connected with high probability with next cavities, positioned close to

the walls (Fig. 3b), but this can be confirmed only by applying other geophysical methods in the future.

Central anomaly was also inspected by the ERT method – along a line at local y-coordinate 117 m, crossing the manifestation of the cavity (Fig. 3a, red segment line). Separation distance of the electrodes was only 25 cm and the electrical contact between the electrodes and the floor was improved by a bentonite bed (for every single electrode outlet, Fig. 4). Tested methodology worked very well (electrical contact) and we have received sound results. From the commonly used concepts of ERT measurements, the Wenner-alpha, Schlumberger and dipole-dipole configuration have been used. Best results (best developed subsurface high resistivity anomalous feature) have been received for the dipole-dipole configuration (Fig. 5a), which is in confirmation with synthetic studies (e.g. *Putiška et al., 2012*). The well-known software RES2DINV for acquired ERT data inversion was

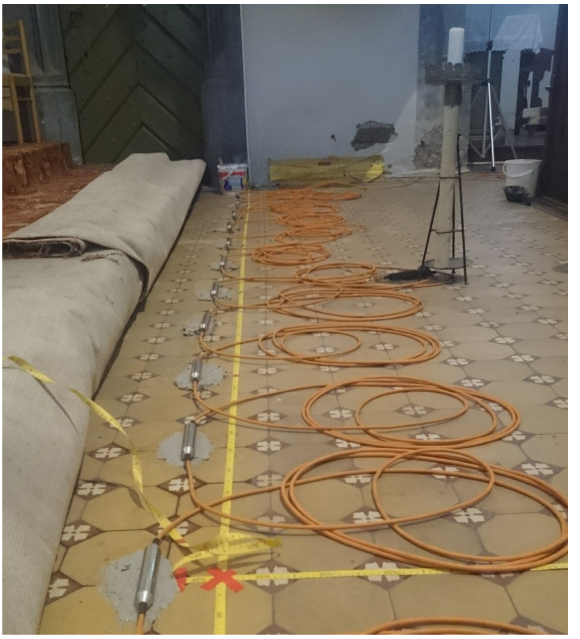

Fig. 4. Installation of the ERT electrodes section along a line inside the church of St. Catherine in Banská Štiavnica. Grounding conditions between the electrodes and the floor were improved by a bentonite bed (for every single electrode outlet).

used (*Loke, 2002*). Result shows a relatively shallow structure in the central part of the profile (with the higher resistivity from $x = 99.5$ to $x = 100.7$ m, Fig. 5a), starting almost from the surface down to the depth of approx. 1.4 m. There occurs also a local shallow high resistivity anomaly at $x = 99$ m, but we interpret it as a deformation of the section due to higher transient resistance at the group of electrodes at this place. The start of the depth extend of the main detected object is shallow, which means that the upper edge of the main cavity is probably positioned in a very small depth. This depth can be identical with the horizontal resolution of this section, which is very close to the separation of the electrodes (0.25 m).

These results are fully confirmed by the GPR results on a parallel line (Fig. 3a, blue segment line). As we can see in Fig. 5b, a dominant diffraction wave with the top at the TWT time (two-way travel time) of approx. 9 ns represents the upper edge of the main cavity. Converted into depths with an estimated velocity 8.5 cm/ns, (based on the analysis of selected diffrac-

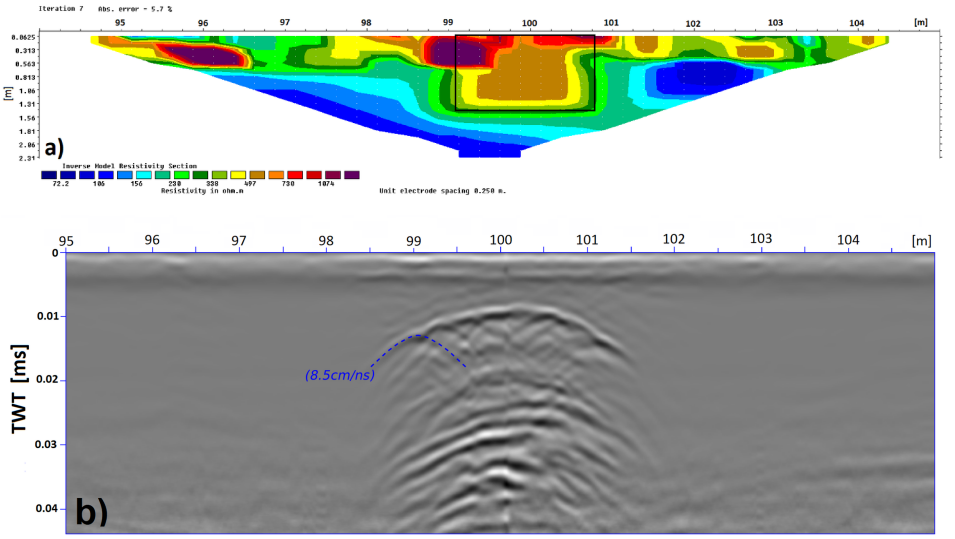

Fig. 5. Vertical sections from ERT (a) and GPR (b) methods along lines depicted in Fig. 3a. Inverted resistivity section (part a) was received after 7 iterations steps from the RES2DINV programme, for dipole-dipole configuration. Black rectangle represents the manifestation of the main interpreted cavity. In part b) in the vertical GPR section, there is depicted one selected local diffraction wave, used for the estimation of the penetration velocity (8.5 cm/ns).

tion hyperbola in the vertical section, Fig. 5b), it corresponds to a depth of approx. 40 cm. Estimation of the bottom edge of this cavity is much more ambiguous, because of the deformation of propagating waves (partly also through the air in the cavity). A strong reflection can be identified at the TWT time of approx. 30 ns, which represents a depth of approx. 130 cm. Both estimations from the ERT and GPR methods give such a relatively small depth extent of this detected cavity (approx. from 0.3–0.4 to 1.3–1.4 m), which corresponds more to a larger grave than to a crypt. Results from the 3D Euler deconvolution method are not as clear as in previous case. This depth estimation method was applied on the central anomaly from incomplete Bouguer anomalies (Fig. 3) – the average estimated depth of the cavity centre reaches approx. 1.6 m, which is quite deep in comparison with the results from the geoelectrical methods. We cannot explain this situation – in the absolute majority of previous studies we had achieved a good coincidence of these methods (GPR and Euler method). Possibly, the central negative anomaly represents a combined effect of the crypt with an effect of a corridor, running in the direction to another cavity, positioned in the upper right corner of the presbytery (Fig. 3b), but this interpretation is very speculative and is not supported by GPR data in this part of the church. Explanation of this situation will be probably given in the future, when next GPR survey together with archaeological excavation or video-inspection will be performed.

4. Third case-study: microgravimetric and GPR research of the interior of St. Joseph's church in Beckov, SW Slovakia

In this third example we show results of GPR and microgravimetric research of the interior of St. Joseph's church in the village Beckov (SW Slovakia), which was realized in the frame of a voluntary work of teachers and students from the Department of applied and environmental geophysics, Comenius University in Bratislava in collaboration with Franciscan fraters from the monastery in Beckov. Both methods were focused on the area of the transition from the main aisle to the presbytery (Figs. 6 and 7), because here was expected an existence of the main crypt in this church. Used instruments, data acquisition and processing methods were identical with that, described in previous two case-studies.

As it is nicely visible in the GPR horizontal reflection maps for various penetration depths (Fig. 6), a cavity with relatively complex structure was detected – it is composed from a major corridor and perpendicularly oriented separated spaces for positioning of coffins, so called columbarium. It is interesting to mention, that in our long year experience with geophysical

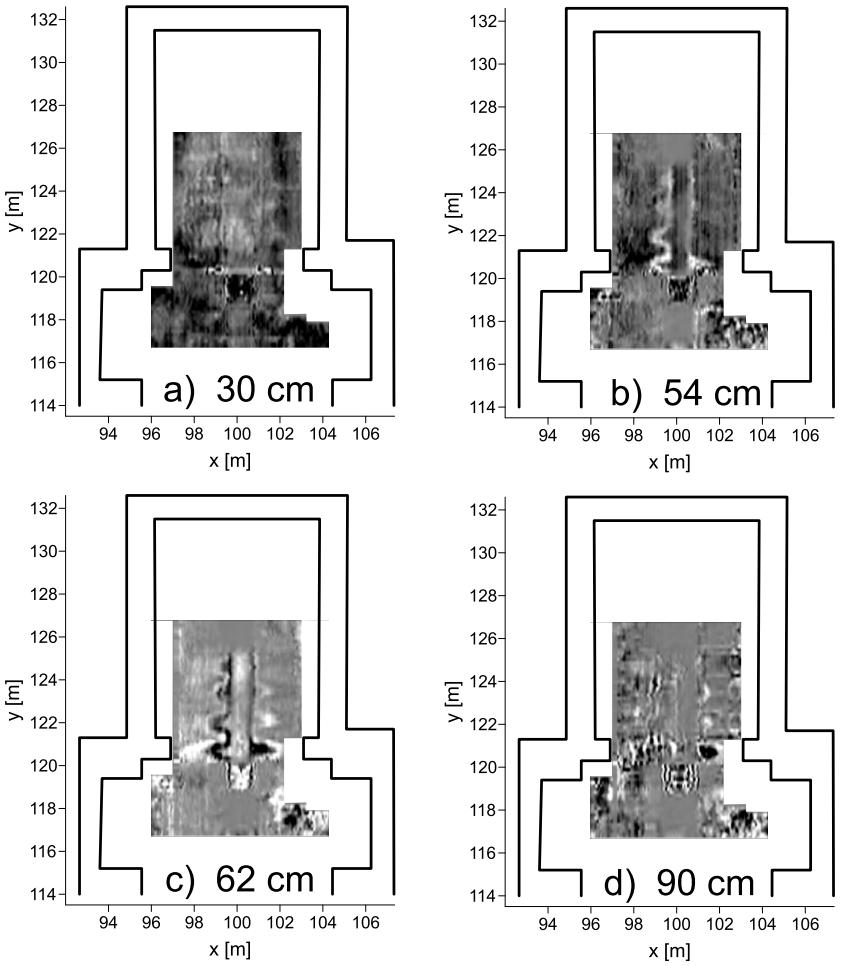

Fig. 6. Results from the GPR survey from the interior of St. Joseph's church in Beckov, SW Slovakia. a) Horizontal GPR reflection amplitude map for the penetration depth of 30 cm, b) horizontal map for the penetration depth of 54 cm, c) horizontal map for the penetration depth of 62 cm, d) horizontal map for the penetration depth of 90 cm.

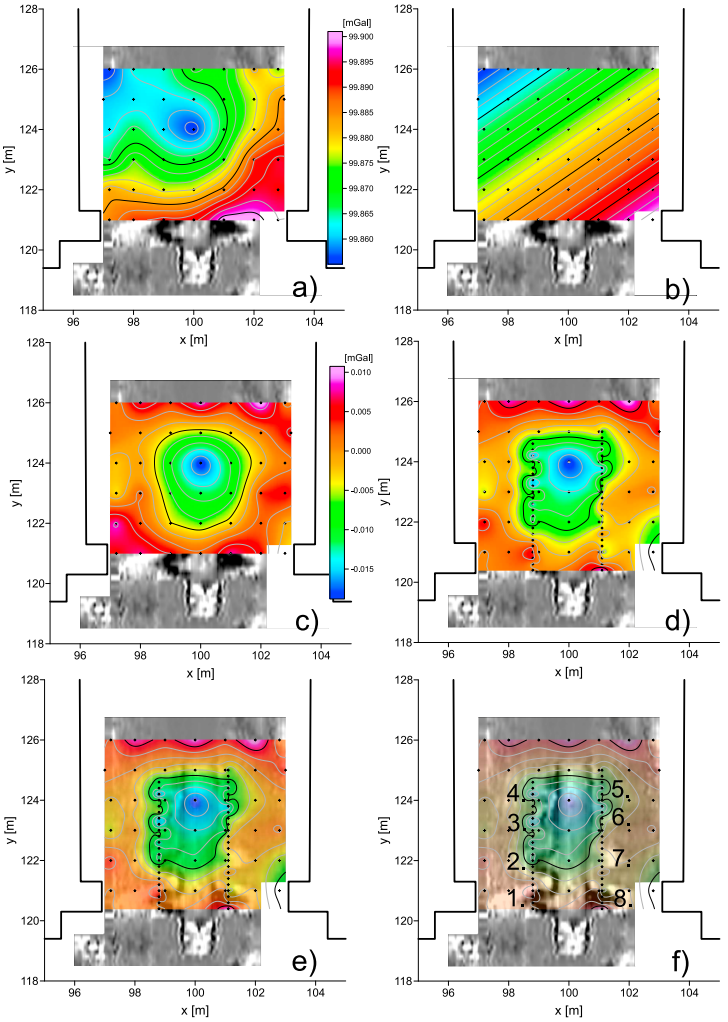

Fig. 7. Results from the microgravity survey from the interior of St. Joseph's church in Beckov, SW Slovakia. a) Coloured contour image map of incomplete Bouguer anomalies for the correction density 2.0g/cm^3 calculated from 1×1m separated points, b) Map of the planar trend, obtained from the field of incomplete Bouguer anomalies by means of LSQ method, c) Coloured contour image map of residual incomplete Bouguer anomalies, d) Coloured contour image map of residual incomplete Bouguer anomalies, calculated from 1×1m separated points together with detailed points (0.2m distance) on two added lines, e) The same field from part (d), but displayed with medium transparency, f) The same field from part (d), but with high transparency together with order numbers of detected "coffin cavities" in the columbarium.

data acquisition in historical objects and churches in Slovakia, this is the first occurrence of such a type of crypt or tomb, detected by means of the GPR method. The upper edge of this crypt appears in a relative shallow depth – of approx. 0.5 m. For depths larger than approx. 1.4 m this structure (pattern) disappears from the horizontal GPR sections (not shown in this paper).

Microgravity survey could be realized only in a part of the presbytery (Fig. 7), because of technical problems with one of the used instruments. Beside this limitation (not the whole area of the columbarium could be covered), obtained results are interesting. In the first stage, this area was covered by a net of 1×1 m points. Received incomplete Bouguer anomalies map (Fig. 7a) has a relatively strong trend in a diagonal direction, coming probably from deeper geological composition of the underground. This trend was constructed by means of planar regression (LSQ method) (Fig. 7b) and removed from the original field – the residual incomplete Bouguer anomalies map is displayed in Fig. 7c. In this map the complex columbarium structure is manifested as one simple cavity (one dominant negative anomaly) and the local separated spaces of coffins cannot be (of course) recognized. Beside this, the received residual field is deformed on its edges (because of a kind of edge effect, occurring during the linear trend removal) and only the central part of this field correctly reflects the presence of the cavity.

In the next step we have repeated the same procedure, but we have incorporated also two detailed lines ($x = 98.8$ m and $x = 101.2$ m), along which the data acquisition was realized with a step of only 20 cm (Fig. 7d). As we can see in details in Figs. 7e and 7f (here the residual field map is displayed with higher transparency), incorporation of these detailed values helped to obtain more "rangy" anomalous field and some parts could be maybe identified with the local separated spaces for coffins (order numbers of anomalies Nr. 3, 4, 5 in Fig. 7f). More precise analysis of this result shows that these local deviations in the new anomalous field have very small amplitudes – very close to the outer precision of usual data acquisition with Scintrex CG-5 gravity meters (approx. $\pm 5\,\mu$Gals). This can be well demonstrated in graphs of residual incomplete Bouguer anomalies along these two detailed lines ($x = 98.8$ m and $x = 101.2$ m), displayed in Fig. 8. Reader can see that achieved small amplitude negative anomalies have in the majority a random character and cannot be well synchronized with the positions of

coffin spaces (with exception of anomalies Nr. 3 and 6), derived from GPR measurements (thick black segment lines with order numbers in bottom of graphs in Fig. 8). Gravitational effects, caused by the presence of such small cavities (coffin spaces) in their actual depth position have very small amplitudes and cannot be therefore detected by the used microgravimetric method (with the used instrument, sampling intervals and processing procedure). Depth of the source of the central negative anomaly (mainly from the corridor in the columbarium), obtained from the 3D Euler deconvolution method, was estimated with a value: 0.9 m. When we compare this result with the results from the GPR method (0.5–1.4 m), solutions from 3D Euler deconvolution method are positioned in the first half and centre of the GPR values, which is also in this case consistent with our previous experiences with this method (e.g. *Pašteka et al., 2011*) and also from the results presented in the first case-study in this paper.

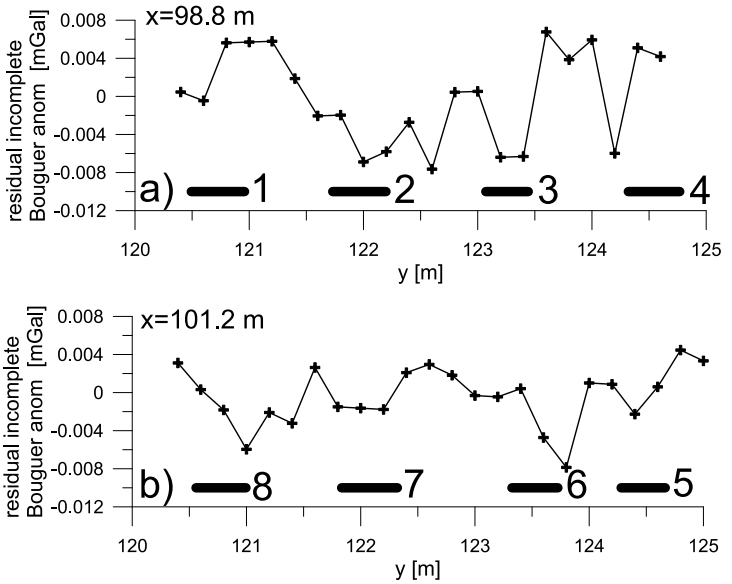

Fig. 8. Graphs of residual incomplete Bouguer anomalies (for the correction density 2.0 g/cm^3) along two detailed lines above the detected columbarium in the St. Joseph's church in Beckov (see Fig. 7d). a) Line along $x = 98.8$ m, b) Line along $x = 102.2$ m. Thick black horizontal lines with order numbers in bottom of both graphs represent the positions of coffin spaces (cavities) taken from the GPR method.

5. Conclusions

We have shown in these three presented case-studies from various churches in SW and central Slovakia that the combination of microgravimetric and geoelectrical methods can be very effective in the detection and study of subsurface cavities such as crypts. Particularly the combination of GPR and microgravimetry is very useful and effective: cavities (crypts) are manifested in horizontal GPR sections as intensive reflectors and in incomplete Bouguer anomaly maps as dominant minima. In the St. Mary's church in Dolné Dubové one central crypt was found by GPR and by microgravity method (depth extent: approx. 0.5–2 m). In the St. Catherine's church in Banská Štiavnica a relatively shallow central cavity (crypt?) was found by GPR and ERT methods (depth extent: approx. 0.3–1.4 m). Anomalous gravity field has confirmed this position, but depth estimates from the Euler deconvolution methods gave larger depths (approx. 1.6 m), which we cannot explain at this moment. In the St. Joseph's church in Beckov the GPR method has found a central crypt in the presbytery (in a form of so called columbarium) and microgravimetry has confirmed the presence of this crypt (but not the local coffin spaces in the columbarium).

We would like to emphasize two original points in this contribution:

1) We have realized, for the first time in Slovakia, ERT measurements inside a building in a completely non-invasive approach – in the St. Catherine's church in Banská Štiavnica. Separation distance of the electrodes was only 25 cm and the electrical contact between the electrodes and the floor ensured by applying a bentonite bed for every electrode outlet. The measurement system worked well and we have obtained a manifestation of relatively shallow cavity (crypt?) – in an almost identical position as obtained by the GPR method.

2) Also, for the first time, we have realized microgravimetric measurements with extremely small acquisition interval – only 20 cm (along two selected acquisition lines). This was realised in the church of St. Joseph in Beckov, where the GPR method has recovered a crypt with a relative complex structure – the so called columbarium (main crypt with perpendicularly oriented smaller separated spaces for placing the coffins). The result of this trial did not yield the expected results – anomalies caused by such small cavities are too small to be correctly detected by means of

microgravimetry.

In general, we can state that the GPR method is faster in data acquisition, when compared to microgravity method. As for processing the acquired data the situation is opposite. The great advantage of the GPR method is the fact that it gives also the depth information, while in gravimetry this kind of information comes from the interpretation process (which can be often ambiguous). A good example are the results obtained from the applied 3D Euler deconvolution method, where the depth estimates in some cases are not realistic – here in the example of the St. Catherine's church in Banská Štiavnica the received depth estimates were too deep.

Acknowledgements. Authors would like to express their thanks to all our students and colleagues from the Christian-Albrechts University in Kiel and from the Comenius University in Bratislava, who helped us with the data acquisition. We would also like to thank Bruno Meurers for borrowing the Scintrex CG-5 instrument from the Department of Meteorology and Geophysics, Vienna University. Our thanks belong also to Franciscan fraters from the monastery in Beckov, who allowed us to perform measurements in the church of St. Joseph's, which belongs to their guardianship. Published research was supported by the Slovak scientific agency VEGA in the frame of project 1/0462/16. Some methodical aspects have been solved also as a part of the scientific program in the frame of the COST Action SAGA: The Soil Science & Archaeo-Geophysics Alliance – CA17131 (`https://www.saga-cost.eu/`), supported by COST (European Cooperation in Science and Technology).

References

Blížkovský M., 1979: Processing and applications in microgravity surveys. Geophys. Prospect., **27**, 4, 848–861, `doi: 10.1111/j.1365-2478.1979.tb01002.x`.

Cady J. W., 1980: Calculation of gravity and magnetic anomalies of finite-length right polygonal prisms. Geophysics, **45**, 10, 1507–1512, `doi: 10.1190/1.1441045`.

Cataldo R., D'Agostino D., Leucci G., 2012: Insights into the Buried Archaeological Remains at the Duomo of Lecce (Italy) Using Ground-penetrating Radar Surveys. Archaeol. Prospect., **19**, 3, 157–165, `doi: 10.1002/arp.1423`.

Clark A., 1990: Seeing Beneath the Soil: Prospecting Methods in Archaeology. Bathsford, 196 p.

Gaffney C., Gater J., 2003: Revealing the Buried Past: Geophysics for Archaeologists. Tempus, 192 p.

Lakshmanan J., Montlucon J., 1987: Microgravity probes the Great Pyramid. Lead. Edge, **6**, 1, 10–17, doi: 10.1190/1.1439319.

Leucci G., 2006: Contribution of Ground Penetrating Radar and Electrical Resistivity Tomography to identify the cavity and fractures under the main Church in Botrugno (Lecce, Italy). J. Archaeol. Sci., **33**, 9, 1194–1204, doi: 10.1016/j.jas.2005.12.009.

Linford N., 2006: The application of geophysical methods to archaeological prospection. Rep. Prog. Phys., **69**, 7, 2205–2257, doi: 10.1088/0034-4885/69/7/R04.

Loke M. H., 2002: Tutorial: 2-D and 3-D electrical imaging surveys. Manuscript, online, accessed 2019-11-20, available from: http://personales.upv.es/jpadin/coursenotes.pdf.

Mrlina J., Křivánek R., Majer A., 2005: Geophysical Survey in the St. Vitus Cathedral in Prague (Geofyzikální prùzkum k lokalizaci hrobky v katedrále sv. Víta v Praze). Castrum Pragense, **6**, 105–124 (in Czech, English abstract).

Negri S., Leucci G., 2006: Geophysical investigation of the Temple of Apollo (Hierapolis, Turkey). J. Archaeol. Sci., **33**, 11, 1505–1513, doi: 10.1016/j.jas.2006.02.003.

Padín J., Martín A., Anquela A. B., 2012: Archaeological microgravimetric prospection inside don church (Valencia, Spain). J. Archaeol. Sci., **39**, 2, 547–554, doi: 10.1016/j.jas.2011.10.012.

Panisova J., Pašteka R., Papčo J., Fraštia M., 2012: The calculation of building corrections in microgravity surveys using close range photogrammetry. Near Surf. Geophys., **10**, 5, 391–399, doi: 10.3997/1873-0604.2012034.

Panisova J., Fraštia M., Wunderlich T., Pašteka R., Kušnirák D., 2013: Microgravity and Ground-penetrating Radar Investigations of Subsurface Features at the St. Catherine's Monastery, Slovakia. Archaeol. Prospect., **20**, 3, 163–174, doi: 10.1002/arp.1450.

Panisova J., Murín I., Pašteka R., Haličková J., Brunčák P., Pohánka V., Papčo J., Milo P., 2016: Geophysical fingerprints of shallow cultural structures from microgravity and GPR measurements in the Church of St. George, Svaty Jur, Slovakia. J. Appl. Geophys., **127** (April), 102–111, doi: 10.1016/j.jappgeo.2016.02.009.

Pašteka R., Zahorec P., 2000: Interpretation of microgravimetrical anomalies in the region of the former church of St. Catherine, Dechtice. Contrib. Geophys. Geod., **30**, 4, 373–387.

Pašteka R., Terray M., Hajach M., Pašiaková M., 2007: Microgravity measurements and GPR technique in the search for medieval crypts: a case study from the St. Nicholas church in Trnava, SW Slovakia. Proceedings of the Archaeological Prospection 7th conference in Nitra, Štúdijné zvesti, **41**, 222–224.

Pašteka R., Richter F. P., Karcol R., Brazda K., Hajach M., 2009: Regularized derivatives of potential fields and their role in semi-automated interpretation methods. Geophys. Prospect., **57**, 4, 507–516, doi: 10.1111/j.1365-2478.2008.00780.x.

Pašteka R., Karcol R., Pašiaková M., Pánisová J., Kušnirák D., Béreš J., 2011: Depth Estimation of Microgravity Anomalies Sources by Means of Regularized Downward

Continuation and Euler Deconvolution. Proceedings from the 73rd EAGE Conference & Exhibition, Vienna, Austria, 23–26 May 2011, 5 p., doi: 10.3997/2214-4609.20149399.

Potent modelling software, Geophysical Software Solutions, User's guide, version v4.16.07, Manuscript, online, accessed 2019-11-17, available from: http://www.geoss.com.au/downloads.html.

Putiška R., Nikolaj M., Dostál I., Kušnirák D., 2012: Determination of cavities using electrical resistivity tomography. Contrib. Geophys. Geod., **42**, 2, 201–211, doi: 10.2478/v10126-012-0018-3.

Reid A. B., Allsop J. M., Granser H., Millet A. J., Somerton I. W., 1990: Magnetic interpretation in three dimensions using Euler deconvolution. Geophysics, **55**, 1, 80–91, doi: 10.1190/1.1442774.

Sandmeier K. J., 2019: ReflexW Vers. 9, Manual. SandmeierGeo, Karlsruhe, Manuscript, online, accessed 2019-11-18, available from: https://www.sandmeier-geo.de/download.html.

Sarlak B., Aghajani H., 2017: Archaeological investigations at Tepe Hissar-Damghan using Gravity and Magnetics methods. J. Res. Archaeom., **2**, 2, 19–34, doi: 10.29252/jra.2.2.19.

Slepak Z., 1997: Complex geophysical investigations for studying the cultural layer and remains of ancient buildings in the territory of Kazan Kremlin, Kazan, Republic of Tatarstan, Russia. Archaeol. Prospect., **4**, 4, 207–218, doi: 10.1002/(SICI)1099-0763(199712)4:4<207::AID-ARP83>3.0.CO;2-L.

Zieliński A., Łyskowski M., Mazurkiewicz E., Lubarska K. W., 2019: Burial crypts in solid rock – a geophysical case study of a small church with a unique polychrome in Szydłów (S Poland). Geol. Geophys. Env., **45**, 2, 89–97, doi: 10.7494/geol.2019.45.2.89.

sciendo

Contributions to Geophysics and Geodesy Vol. 49/4, 2019 (497–510)

Calculation of temperature distribution and rheological properties of the lithosphere along transect IV in the Western Carpathian-Pannonian Basin region

Jana DÉREROVÁ[1,*], Miroslav BIELIK[1,2], Igor KOHÚT[1], Dominika GODOVÁ[1]

[1] Division of Geophysics, Earth Science Institute of the Slovak Academy of Sciences, Dúbravská cesta 9, 840 05 Bratislava, Slovak Republic

[2] Department of Applied and Environmental Geophysics, Faculty of Natural Sciences, Comenius University, Mlynská dolina, Ilkovičova 6, 842 48 Bratislava, Slovak Republic

Abstract: 2D integrated modelling algorithm was used to calculate the temperature distribution in the lithosphere along the transect IV located in the Western Carpathian-Pannonian Basin area. Based on the determined temperature field and given rheological parameters of the rocks, it was possible to calculate the strength distribution for both compressional and extensional regimes, construct the strength envelopes for chosen columns of the main tectonic units of the model, and thus construct a simple rheological model of the lithosphere along transect IV. The obtained results indicate decrease of the lithospheric strength from the European platform and the Western Carpathians towards the Pannonian Basin. The largest strength (valid for all tectonic units) can be observed within the upper crust with its maxima on the boundary between upper and lower crust, decreasing towards lower crust and disappearing in the lithospheric mantle, suggesting mostly rigid deformation occurring in the upper crust. A local increase in the values of strength can be observed in the eastern segment of the Western Carpathians where crustal thickening accompanies the lithospheric thickening (formation of the lithospheric root), unlike the previous models along transects I and II, that pass through the western segment of the Western Carpathians and their lithosphere-asthenosphere boundary is almost flat and therefore no accompanying crustal thickening is observed and the decrease in strength is slow and steady.

Key words: 2D integrated modelling, temperature field, rheological parameters, compressional and extensional strength, strength envelopes

*corresponding author: e-mail: geofjade@savba.sk

doi: 10.2478/congeo-2019-0026

1. Introduction

The Carpathian-Pannonian Basin region together with its surrounding tectonic units is a very complex lithospheric system where many different tectonic units can be identified in a relatively small area. Therefore, it provides a great opportunity to study their mutual interactions, the interaction of lithosphere and asthenosphere as well as many geodynamic interactions within the lithosphere during volcanic arc and related fore- and back-arc basin development.

The Pannonian Basin is young and hot, while the Western Carpathians, although being young as well, are colder. The evolution of the Carpathian arc was driven by the inter-related processes of rift genesis, crustal thinning, lateral displacement, rotational movements, convergence, collisional suturing, accretion, transpressive–transtensive subduction, slab rollback, asthenospheric up-welling and lateral extrusion of the Eastern Alps and Dinarides-Balkan orogens, while formation of the Pannonian Basin is related to interplay of contraction, strike-slip and extension (*Ratschbacher et al., 1991a,b; Csontos et al., 1992; Horváth, 1993*).

The Carpathian-Pannonian Basin region has been covered by extensive geophysical surveys, and an enormous amount of geological and geophysical data such as deep seismic reflection and refractions data (*Mayerová et al., 1994; Tomek et al., 1989; Vozár and Šantavý, 1999*), gravity data (*Bielik et al.,2006; Alasonati Tašárová et al., 2009; Zahorec et al., 2013*), surface heat flow data (*Čermák et al., 1991; Majcin, 1993*), geoelectric data (*Putiška et al., 2012a,b*), magnetotelluric data (*Ádám, 1996*) has been collected and is available for calculations and modelling in order to reconstruct the structure of the lithosphere and geodynamical and tectonic processes within it. Despite the fact that the Carpathian-Pannonian Basin area becomes very well explored and studied, the main focus still lays on the lithospheric structure reconstruction (*Alasonati Tašárová et al., 2009, 2016; Grinč et al., 2013; Hrubcová et al., 2010; Dérerová et al., 2006; Grad et al., 2006; Bielik et al., 2005* and many others). We believe that rheological modelling can provide additional information to already existing lithosperic models and contribute to better understanding of interactions among different tectonic units from rheological point of view.

The very first rheological models of the lithosphere have been calculated

by *Bielik and Striženec (1994)*, *Bielik and Ursíny (1997)* and *Lankreijer et al. (1999)*. 2-dimensional integrated modelling method has been used to calculate temperature distribution and construct the rheological model along transect I (*Dérerová et al., 2012*) and and transect II (*Dérerová et al., 2014)* passing through the Carpathian-Pannonian basin region. To improve the rheological model of the lithosphere in the study area, we decided to continue in our approach and calculate and construct rheological model along transect IV located in the same study area.

2. The Western Carpathian Transect IV

The studied transect IV (*Zeyen et al., 2002*) (Fig. 1) starts in the Polish European foreland, continues across the Western Carpathian molasse foredeep, the Outer Western Carpathian flysch, the Pienniny Klippen Belt, the Slovenské Rudohorie Mts. and finishes in the Pannonian Basin. From an interpretation point of view the direction of the transect IV is not optimal, since it is not perpendicular to the strike of the geological structures. We chose this profile nevertheless because it coincides with the international transect CEL04, which is one of the seismic profiles of the CELEBRATION 2000 project. Its length is 550 km and the layout of main geological structures it consists of can be seen on Fig. 2 (*Zeyen et al., 2002*).

3. Method

Lithospheric structure along Transect IV (Fig. 2) has previously been modelled as a part of a tectonic and geodynamical reconstruction of the Western Carpathians-Pannonian basin region (*Zeyen et al., 2002*), using 2D integrated geophysical modelling method. It is an algorithm that calculates lithospheric thermal structure based on the simultaneous interpretation of surface heat flow, gravity, and topography data. A finite element algorithm is used to calculate the two-dimensional temperature distribution in the lithosphere, given its thickness (here defined as the 1300 °C isotherm) and the distribution of heat production and thermal conductivity, solving the steady state heat conduction equation (*Lachenbruch and Sass, 1977*):

$$\lambda \nabla^2 T = A\,, \tag{1}$$

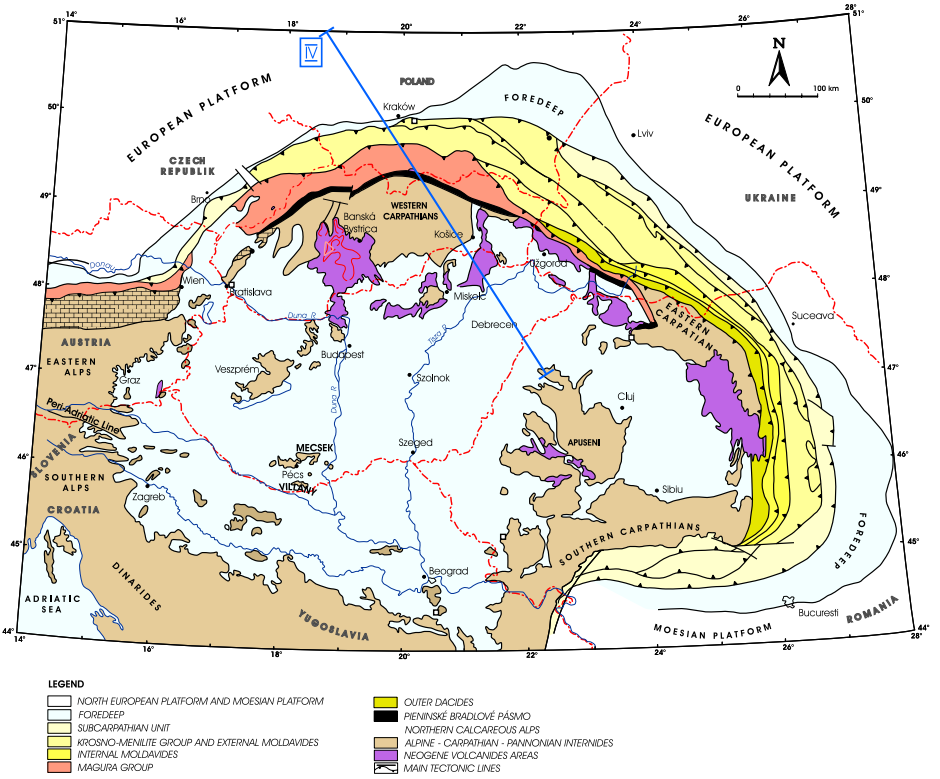

Fig. 1. Location of transect IV on the map of the Carpathian-Pannonian Basin region (modified after *Zeyen et al., 2002*).

where λ is the thermal conductivity [$\mathrm{Wm^{-1}K^{-1}}$], T is the temperature [K] and A the heat production [$\mathrm{Wm^{-3}}$]. More detailed description can be found in *Zeyen and Fernàndez (1994)*.

Based on the determined temperature distribution in the lithosphere, we can calculate the yield strength for a given distribution of rheological rock parameters. The strength is defined as the minimum of brittle and ductile strength at each point. For brittle strength calculation we have assumed that deformation occurs according to the frictional sliding law given by *Byerlee (1978)*:

$$\sigma_{brittle} = \alpha \rho g z (1 - \lambda)\,, \tag{2}$$

where $\sigma_{brittle}$ is brittle failure function [Pa], parameter $\alpha = R - 1/R$ is valid

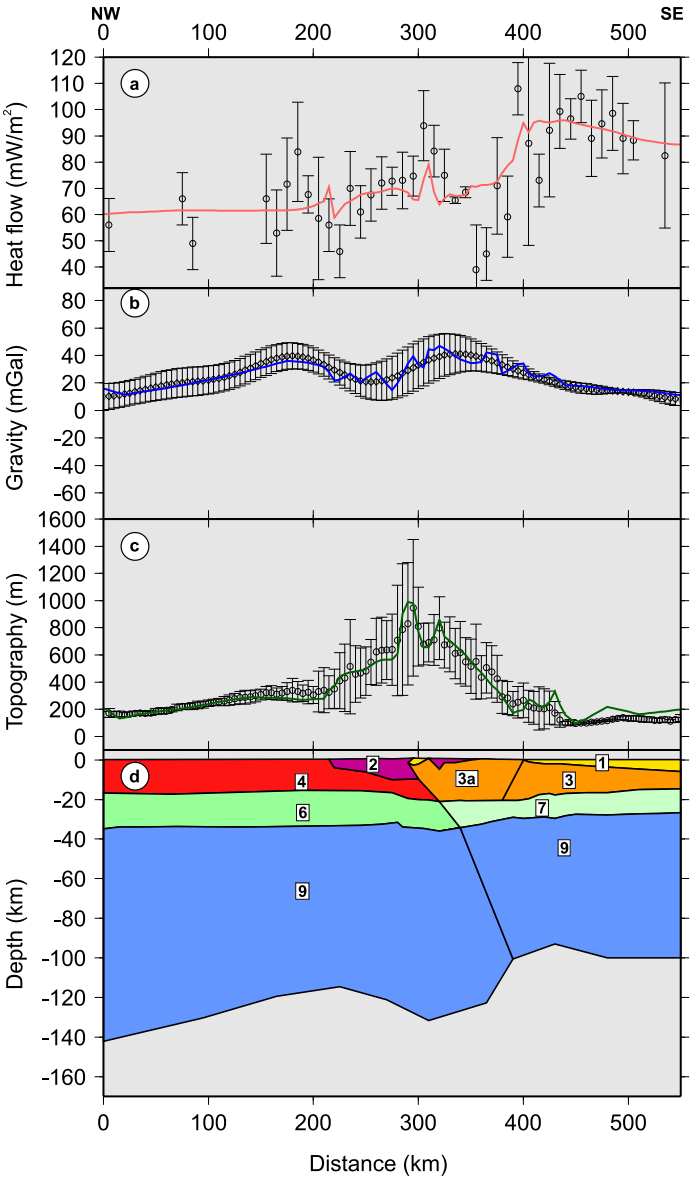

Fig. 2. Lithospheric model along transect IV. (a) Surface heatflow, (b) free air gravity anomaly, (c) topography with dots corresponding to measured data with uncertainty bars and solid lines to calculated values. Numbers in (d) correspond to material number in Table 1b (*Zeyen et al., 2002*).

for normal faulting, $\alpha = R - 1$ for thrust faulting, $\alpha = R - 1/[1 + \beta(R - 1)]$ for strike-slip faulting. Parameter $R = \left[\left(1 + f_s^2\right)^{1/2} - f_s\right]^{-2}$ depends on coefficient of static friction f_s, λ represents the hydrostatic pore fluid factor, ρ is material density [kg m^{-3}], g is acceleration of gravity [m s^{-2}], z is depth [m], β is extension factor.

Ductile strength is calculated assuming power-law creep deformation given as (*Lynch and Morgan, 1987*):

$$\sigma_{creep} = \left(\frac{\dot{\varepsilon}}{A_p}\right)^{1/n} \exp\left[\frac{E_p}{nRT}\right], \tag{3}$$

where σ_{creep} is power law creep function [Pa], $\dot{\varepsilon}$ denotes strain rate [s^{-1}], A_p is Dorn constant, n is power law exponent, E_p is power law activation energy [kJ mol^{-1}], R is universal gas constant [8.314 J mol^{-1} K^{-1}], T is temperature [K].

4. Results

2D integrated modelling algorithm has been used to calculate temperature distribution for a pre-modelled lithospheric structure of the transect IV (Fig. 3). The lower limit of the model corresponds to 1300 °C isotherm which represents the lithosphere-asthenosphere boundary in geotermics. On the surface (the upper boundary of the temperature model), the temperature 20 °C has been considered. The temperature distribution has been calculated for every node of the model. Temperature field reflects the distribution

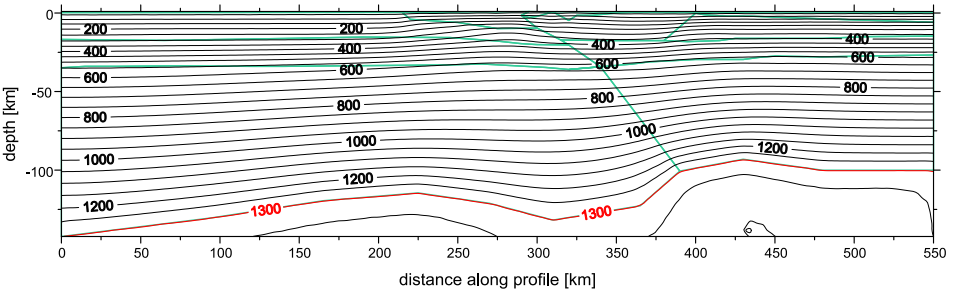

Fig. 3. Lithospheric temperature distribution calculated for transect IV, isoline values in °C. The bottom of the model corresponds to the 1300 °C isotherm (red line).

of the heat sources predominantly in the upper crust and background heat flow density from the lower mantle. The reliability of the temperature model usually depends on the accuracy and density of measurements of the surface heat flow density data but 2D integrated modelling algorithm ensures that our lithological model is constrained by calculation of free air anomaly and topography, which greatly increases the reliability of the model.

In the next step, the rheological parameters for every lithospheric unit of previously modelled transect IV has been assigned. These rheological parameters were carefully chosen based on the work of Carter and Tsenn (*Carter and Tsenn, 1987*) and Goetze and Evans (*Goetze and Evans, 1979*) and a previous rheological modelling in the Western Carpathians by *Lankreijer et al. (1999)*. We made sure that the assigned rheological parameters for transect IV were also in correlation with our previous rheological modelling on transects I and II (*Dérerová et al., 2012, 2014)*. These parameters are shown in Table 1a and Table 1b together with densities and geothermal parameters of the 2D integrated lithospheric model of transect IV.

Table 1a. General properties used for calculation of rheological model.

Definition	**Parameter**	**Value**
Gravity acceleration [ms^{-2}]	g	9.81
Universal gas constant [$\mathrm{J\,mol\,K}^{-1}$]	R	8.314
Temperature at the base of the lithosphere [°C]	T_m	1300
Static friction coefficient	f_s	0.6
Strain rate [s^{-1}]	$\dot{\varepsilon}$	10^{-15}
Hydrostatic pore fluid factor	λ	0.35

With the assigned parameters we were able to calculate the strength distribution in the lithosphere for studied transect. Fig. 4 shows vertically integrated compressional and extensional strength calculated along transect IV. Fig. 5 and Fig. 6 show the calculated yield strength contour plot for compressional and extensional deformation. In our calculations a strain rate 10^{-15} s^{-1} has been used because this value is commonly observed in compressional and extensional settings (*Carter and Tsenn, 1987*). We have calculated the strength envelopes for both compressional and extensional regimes in selected lithospheric columns of the model. We chose one column for each of the main tectonic units (European platform, the Western

Table 1b. Thermal and rheological parameters used for modelling along transect IV (after *Carter and Tsenn (1987)* and *Goetze and Evans (1979)*). HP: heat production [μWm^{-3}], TC: thermal conductivity [Wm^{-1}K^{-1}], ρ: density at room temperature [kg m^{-3}], A_p: power law pre-exponential constant, n: power law exponent, E_p: power law activation energy [kJ mol^{-1}].

Nr.	**Unit**	**HP**	**TC**	$\boldsymbol{\rho}$	$\boldsymbol{A_p}$	$\boldsymbol{n}$	$\boldsymbol{E_p}$
1	Neogene sediments	2.5 – 3.0	2.5	2400 – 2550	3.16E-26	3.30	186
2	Flysch and Volcanics	1.0 – 2.5	2.0 – 2.5	2550 – 2650	3.16E-26	3.30	186
3	Carpathian and Pannonian upper crust	3.0 – 3.5	3.0	2750	3.16E-26	3.30	186
3a	Inner Western Carpathian upper crust	2.0 – 2.5	3.0	2750	3.16E-26	3.30	186
4	European upper crust	0.5 – 2.0	2.5 – 3.0	2750 – 2800	3.16E-26	3.30	186
6	European lower crust	0.2	2.0	2960	6.31E-20	3.05	276
7	Carpathian and Pannonian lower crust	0.2	2.0	3000	6.31E-20	3.05	276
9	Lower (mantle) lithosphere	0.05	3.4	3325	7.94E-18	4.50	535

Carpathians and the Pannonian Basin). The strength distribution for given lithospheric columns is shown on Fig. 7.

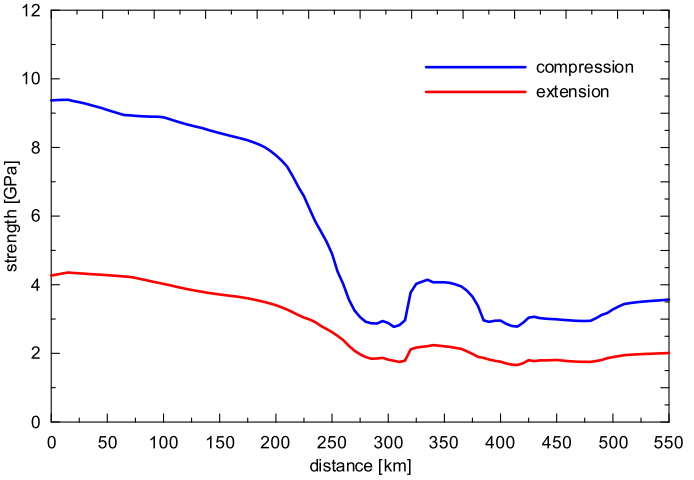

Fig. 4.Vertically integrated compressional (red line) and extensional (blue line) strength calculated along the transect IV.

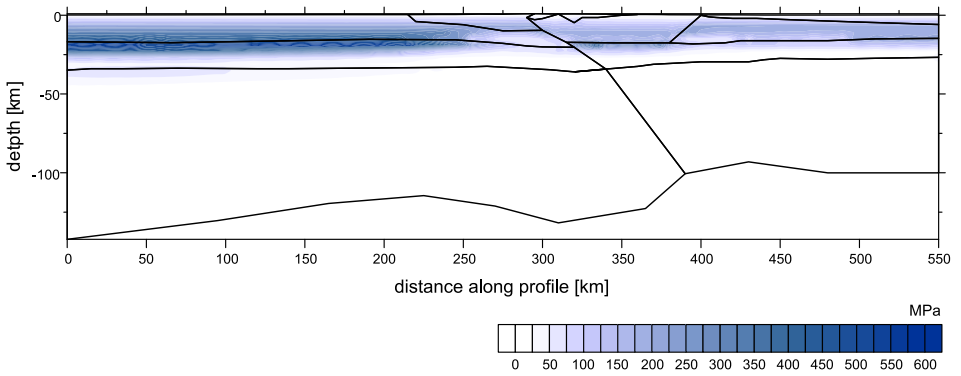

Fig. 5. Yield strength contour plot for compressional deformation calculated along transect IV calculated at a strain rate 10^{-15} s^{-1}.

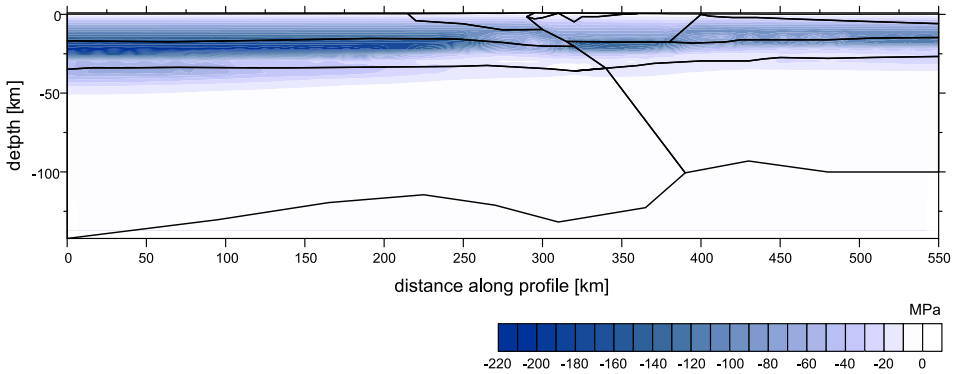

Fig. 6. Yield strength contour plot for extensional deformation calculated along transect IV calculated at a strain rate 10^{-15} s^{-1}.

5. Conclusions

Based on the results related to the vertically integrated compressional and extensional strength along transect IV (Fig. 4), we can say that the lithospheric strength decreases from the European platform and the Western Carpathians to the Pannonian Basin. Decrease is more prominent in the case of compressional strength. A local increase in the values of strength can be observed in the eastern segment of the Western Carpathians where the lithospheric thickening occurs. This thickening (forming of a lithospheric root), which is interpreted as a small remnant of a subducted slab, is also

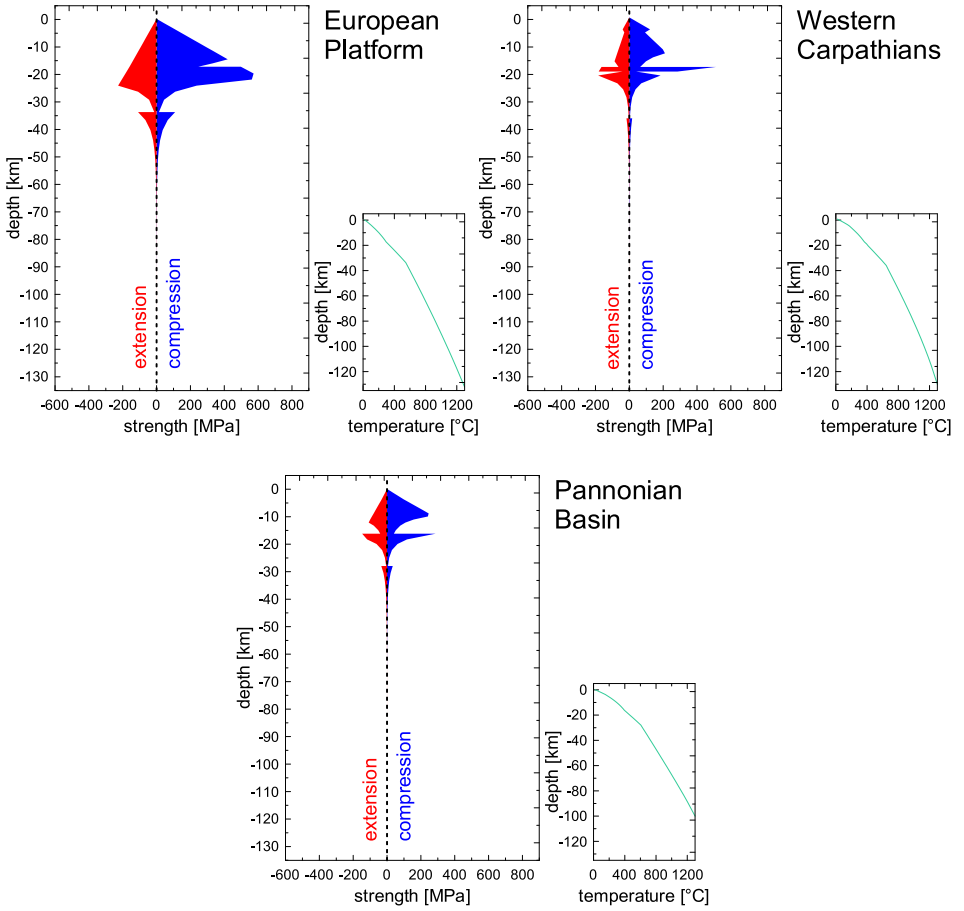

Fig. 7. Vertical strength distribution for different lithospheric columns calculated along transect IV. Negative and positive values correspond to extensional and compressional strength respectively.

accompanied by crustal thickening. If we look at the results of yield strength contour plot for compressional and extensional deformation (Figs. 5 and 6) and vertical strength distribution for different lithospheric columns (see the second strength envelope, where the column was chosen in the area of crustal and lithospheric thickening) for compressional and extensional deformation (Fig. 7), it shows that in the area of crustal thickening, the largest strength

occurs on the boundary between upper and lower crust, causing the increase in the values that can be clearly seen on our calculated vertically integrated strength graph as an increase in both compressional (more prominent) and extensional strength. Along previously modelled transects I and II (*Dérerová et al., 2012, 2014)*, where the lithosphere-asthenosphere boundary is almost flat and therefore no accompanying by crustal thickening is observed, the decrease in strength is slow and steady.

As general result, for all tectonic units (European platform, the Western Carpathians and the Pannonian basin), the largest strength occurs within the upper crust with its maxima on the boundary between upper and lower crust. Towards the lower crust, the strength significantly decreases. Within the uppermost mantle (lower lithosphere) the lithospheric strength almost disappears. These results suggest predominantly rigid deformation in the upper crust and ductile deformation (as a result of higher temperatures) in the lower part of the lithosphere. Similar results have been obtained in previously modelled transects I and II.

Acknowledgements. This research has been supported by the Slovak Grant Agency VEGA, grant No. 2/0006/19 and by the Slovak Research and Development Agency under grant APVV-16-0482, APVV-16-0146. Authors are grateful to Prof. Hermann Zeyen (Laboratoires IDES, Université Paris-Sud XI) for permission to use 2D integrated modelling software.

References

Ádám A., 1996: Regional magnetotelluric (MT) anisotropy in the Pannonian Basin (Hungary). Acta Geod. Geophys. Hung., **31**, 1-2, 191–216.

Alasonati Tašárová Z., Afonso J. C., Bielik M., Götze H.-J., Hók J., 2009: The lithospheric structure of the Western Carpathian-Pannonian region based on the CELEBRATION 2000 seismic experiment and gravity modeling. Tectonophysics, **475**, 3-4, 454–469, doi: 10.1016/j.tecto.2009.06.003.

Alasonati Tašárová Z., Fullea J., Bielik M., Oroda P., 2016: Lithospheric structure of Central Europe: Puzzle pieces from Pannonian Basin to Trans-European Suture Zone resolved by geophysical-petrological modelling. Tectonics, **35**, 3, 722–753, doi: 10.1002/2015TC003935.

Bielik M., Makarenko I., Starostenko V., Legostaeva **O**., Dérerová J., Šefara J., Pašteka R., 2005: New 3D gravity modeling in the Carpathian-Pannonian basin region. Contrib. Geophys. Geod., **35**, 1, 65–78.

Bielik M., Kloska K., Meurers B., Švancara J., Wybraniec S. & CELEBRATION 2000 Potential Field Working Group, 2006: Gravity anomaly map of the CELEBRATION 2000 region. Geol. Carpath., **57**, 3, 145–156.

Bielik M., Striženec P., 1994: Flexure of the lithosphere beneath the Pannonian Basin. Contrib. Geophys. Geod., **24**, 1, 87–104.

Bielik M., Ursíny M., 1997: Flexure of the elastic plate. Contrib. Geophys. Geod., **27**, 1, 81–93.

Byerlee J., 1978: Friction of rocks. Pure Appl. Geophys., **116**, 4-5, 615–626, doi: 10.1007/BF00876528.

Carter N. L., Tsenn M. C., 1987: Flow properties of continental lithosphere. Tectonophysics, **136**, 1-2, 27–63, doi: 10.1016/0040-1951(87)90333-7.

Čermák V., Král M., Krešl M., Kubík J., Šafanda J., 1991: Heat flow, regional geophysics and lithosphere structure in Czechoslovakia and adjacent part of Central Europe. In: Čermák V., Rybach L. (Eds.): Terrestrial heat flow and the lithosphere structure. Springer, Berlin, 133–165, doi: 10.1007/978-3-642-75582-8_6.

Csontos L., Nagymarosy A., Horváth F., Kováč M., 1992: Tertiary evolution of the Intra-Carpathian area: A model. In: Ziegler P. A. (Ed.), Geodynamics of rifting, I, Tectonophysics, **208**, 1-3, 221?241, doi: 10.1016/0040-1951(92)90346-8.

Dérerová J., Zeyen H., Bielik M., Salman K., 2006: Application of integrated geophysical modeling for determination of the continental lithospheric thermal structure in the eastern Carpathians. Tectonics, **25**, 3, TC3009, doi: 10.1029/2005TC001883.

Dérerová J., Kohút I., Bielik M., Bošanský M., Porubčanová B., 2012: Calculation of temperature distribution and rheological properties of the lithosphere along transect I in the Western Carpathians. Contrib. Geophys. Geod., **42**, 4, 345–356, doi: 10.2478/v10126-012-0016-5.

Dérerová J., Bielik M., Pašiaková M., Kohút I., Hlavňová P., 2014: Calculation of temperature distribution and rheological properties of the lithosphere along transect II in the Western Carpathians. Contrib. Geophys. Geod., **44**, 2, 149–160, doi: 10.2478/con geo-2014-0009.

Goetze C., Evans B., 1979: Stress and temperature in the bending lithosphere as constrained by experimental rocks mechanics. Geophys. J. Int., **59**, 3, 463–478, doi: 10.1111/j.1365-246X.1979.tb02567.x.

Grad M., Guterch A., Keller G. R., Janik T., Hegeds E., Vozár J., Ol1czka A., Tiira T., Yliniemi J., 2006: Lithospheric structure beneath trans-Carpathian transect from Precambrian platform to Pannonian Basin: CELEBRATION 2000 seismic profile CEL05. J. Geophys. Res., **111**, B3, B03301, doi: 10.1029/2005JB003647.

Grinč M., Zeyen H., Bielik M., Plašienka D., 2013: Lithospheric structure in Central Europe: Integrated geophysical modelling. J. Geodyn., **66**, 13–24, doi: 10.1016/j.jog.2012.12.007.

Horváth F., 1993: Towards a mechanical model for the formation of the Panonian basin. Tectonophysics, **226**, 1-4, 333?357, doi: 10.1016/0040-1951(93)90126-5.

Hrubcová P., Oroda P., Grad M., Geissler W. H., Guterch A., Vozár J., Hegeds E., Sudetes Working Group, 2010: From the Variscan to the Alpine Orogeny: crustal structure

of the Bohemian Massif and the Western Carpathians in the light of the SUDETES 2003 seismic data. Geophys. J. Int., **183**, 2, 611–633, doi: 10.1111/j.1365-246X.2010.04766.x.

Lachenbruch A. H., Sass J. H., 1977: Heat flow in the United States and the thermal regime of the crust. In: Heacock J. G., Keller G. V., Oliver J. E., Simmons G.: The Earth's crust. Geophys. Monogr. Ser., **20**, 626?675, Washington, D.C., doi: 10.1029/GM020p0626.

Lankreijer A., Bielik M., Cloetingh S., Majcin D., 1999: Rheology predictions across the Western Carpathians, Bohemian Massif and the Pannonian Basin: implications for tectonic scenarios. Tectonics, **18**, 6, 1139–1153, doi: 10.1029/1999TC900023.

Lynch H. D., Morgan P., 1987: The tensile strength of the lithosphere and the localisation of extension. In: Coward M. P., Dewey J. F., Hancock P. L. (Eds.): Continental Extension Tectonics. Geol. Soc. Spec. Publ., London, **28**, 1, 53–65, doi: 10.1144/GSL.SP.1987.028.01.05.

Majcin D., 1993: Thermal state of the West Carpathian lithosphere. Stud. Geophys. Geod., **37**, 4, 345–364, doi: 10.1007/BF01613581.

Mayerová M., Novotný M., Fejfar M., 1994: Deep seismic sounding in Czechoslovakia. In: Bucha V., Blížkovský M. (Eds.): Crustal structure of the Bohemian Massif and the West Carpathians. Academia Press, Springer Verlag, 13–20.

Putiška R., Dostál I., Kušnirák D., 2012a: Determination of dipping contacts using electrical resistivity tomography. Contrib. Geophys. Geod., **42**, 2, 161180, doi: 10.2478/v10126-012-0007-6.

Putiška R., Nikolaj M., Dostál I., Kušnirák D., 2012b: Determination of cavities using electrical resistivity tomography. Contrib. Geophys. Geod., **42**, 2, 201211, doi: 10.2478/v10126-012-0018-3.

Ratschbacher L., Merle O., Davy P., Cobbold P., 1991a: Lateral extrusion in the eastern Alps, Part 1: Boundary conditions and experiments scaled for gravity. Tectonics, **10**, 2, 245?256, doi: 10.1029/90TC02622.

Ratschbacher L., Frisch W., Linzer H.-G., Merle O., 1991b: Lateral extrusion in the eastern Alps, Part 2: Structural analysis. Tectonics, **10**, 2, 257?271, doi: 10.1029/90TC02623.

Tomek E., Ibrmajer I., Koráb T., Biely A., Dvooáková L., Lexa J., Zbooil A., 1989: Crustal structures of the West Carpathians on deep reflection seismic line 2T. Mineralia Slovaca, **21**, 1, 3–26 (in Slovak with English summary).

Vozár J., Šantavý J., (Eds.) 1999: Atlas of deep reflection seismic profiles of the Western Carpathians and their interpretation (Atlas hlbinných reflexných seizmických profilov Západnych Karpát a ich interpretácia). Ministry of Environment of the Slovak Republic, Bratislava, ISBN 80-88974-06-2, 76 p.

Zahorec P., Papčo J., Marušiak I., Mikuška J., Pašteka R., Ferianc D., Majkráková M., 2013: Reconstruction of the gravity acceleration from complete Bouguer anomalies in Slovakia – modern software solution. In: Nové poznatky z realizácie a interpretácie geodetických meraní. Zborník referátov. Slovenská spoločnosť geodetov a kartografov, Bratislava, 75–83.

Zeyen H., Fernàndez M., 1994: Integrated lithospheric modeling combining thermal, gravity and local isostasy analysis: Application to the NE Spanish Geotransect. J. Geophys. Res., **99**, B9, 18089–18102, doi: 10.1029/94JB00898.

Zeyen H., Dérerová J., Bielik M., 2002: Determination of the continental lithosphere thermal structure in the western Carpathians: Integrated modelling of surface heat flow, gravity anomalies and topography. Phys. Earth Planet. Inter., **134**, 1-2, 89–104, doi: 10.1016/S0031-9201(02)00155-3.

sciendo

Contributions to Geophysics and Geodesy Vol. 49/4, 2019 (511–523)

Seismic activity on the territory of Slovakia in 2018

Róbert KYSEL[1,2,*], Andrej CIPCIAR[1,2], Kristián CSICSAY[1], Lucia FOJTÍKOVÁ[1,4], Martin ŠUGÁR[1,3], Jozef KRISTEK[1,2]

[1] Earth Science Institute of the Slovak Academy of Sciences, Dúbravská cesta 9, P. O. Box 106, 840 05 Bratislava, Slovak Republic

[2] Faculty of Mathematics, Physics and Informatics, Comenius University in Bratislava, Mlynská dolina, 842 48 Bratislava, Slovak Republic

[3] Faculty of Natural Sciences, Comenius University in Bratislava, Mlynská dolina, Ilkovičova 6, 842 15 Bratislava, Slovak Republic

[4] Institute of Rock Structure and Mechanics of the Czech Academy of Sciences, V Holešovičkách 94/41, 182 09, Prague 8, Czech Republic

Abstract: The National Network of Seismic Stations of Slovakia (NNSS) consists of eight short period and five broadband permanent seismic stations and a data centre located at the Earth Science Institute of the Slovak Academy of Sciences (ESI SAS). The NNSS recorded and detected 11704 seismic events from all epicentral distances in 2018. Totally 86 earthquakes originated in the territory of Slovakia in 2018. This paper provides basic information on the configuration of the NNSS, routine data processing, seismic activity on the territory of Slovakia in 2018 as well as macroseismic observations collected in 2018.

Key words: Slovakia, National Network of Seismic Stations, seismicity, macroseismic observations

1. Introduction

The seismic activity on the territory of Slovakia and adjacent areas has been reported on the daily basis by the so called Seismo Reports published on the web sites of the Department of Seismology, ESI SAS `http://www.seismology.sk/Seismo_Reports/reports.html` and in annual reports as a part of the project Partial monitoring system – Geological factors (*Liščák et al., 2019*, in preparation) which is solved with a contract between ESI SAS and State Geological Institute of Dionýz Štúr. The aim of this paper is to provide a quick overview of earthquakes which originated on the territory of Slovakia or were macroseismically felt on the territory of Slovakia in 2018.

*corresponding author: e-mail: robert.kysel@savba.sk

doi: 10.2478/congeo-2019-0027

2. Seismic stations operating in 2018

The seismic monitoring of the Slovak territory is provided by the NNSS operated by the ESI SAS (*ESI SAS, 2004*), *Local Seismic Network in Eastern Slovakia* operated by the Faculty of Mathematics, Physics and Informatics of the Comenius University in Bratislava and local network of seismic stations around NPPs Jaslovské Bohunice and Mochovce operated by Progseis Ltd. company. The networks of seismic stations cooperate and the exchange of data is on the regular basis. The positions of the seismic stations on the territory of Slovakia are shown in Fig. 1.

In 2018 the NNSS consisted of thirteen permanent seismic stations, from which eight are short period and five are broadband. Broadband stations are: Červenica (CRVS), Kolonické sedlo (KOLS), Modra (MODS), Vyhne (VYHS) and Železná studnička (ZST). Short period stations are: Hurbanovo (HRB), Izabela (IZAB), Iža (SRO1), Kečovo (KECS), Liptovská Anna (LANS), Moča (SRO2), Stebnícka Huta (STHS) and Šrobárová (SRO). The HRB is the oldest NNSS seismic station that has been in operation since 1909 (*Pajdušák, 1997*). In 2018 the CRVS station was closed due to the changes in the property rights of the location site. A possibility to install a new station in the Šariš region has been investigated. The NNSS permanent

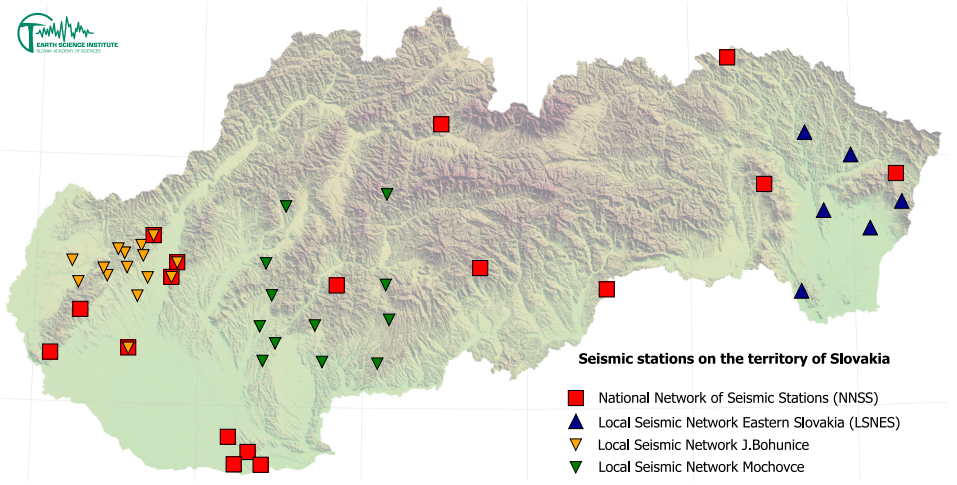

Fig. 1. Seismic stations operational on the territory of Slovakia in 2018.

seismic stations and their instrumentation are summarized in Table 1. More details can be found on the web page `http://www.seismology.sk/National_Network`.

Table 1. Equipment of seismic stations of the NNSS operating in 2018.

Station	**ISC code**	**Lat. [°N]**	**Long. [°E]**	**Alt. [m]**	**Sensor**	**DAS**	**Sampl. freq.**	**Data format**
Bratislava Žel. Studnička	ZST	48.196	17.102	250	3×SKD	Wave24	100/sec	mSEED
Červenica	CRVS	48.902	21.461	476	STS-2	Wave24	100/sec	mSEED
Vyhne	VYHS	48.493	18.836	450	STS-2	Wave24	100/sec	mSEED
Modra-Piesok	MODS	48.373	17.277	520	STS-2	Wave32	100/sec	mSEED
Hurbanovo	HRB	47.873	18.192	115	2× Mainka	Analog	–	smoked paper
Izabela	IZAB	48.569	19.713	450	3×SM3	Wave24	100/sec	mSEED
Iža	SRO1	47.7622	18.2328	111	LE3D	PCM	20/sec	mSEED
Kečovo	KECS	48.483	20.486	345	LE3D	Wave24	100/sec	mSEED
Kolonické sedlo	KOLS	48.933	22.273	460	Guralp-6T-30s	Wave32	100/sec	mSEED
Liptovská Anna	LANS	49.151	19.468	710	LE3D	SEMS	100/sec	mSEED
Moča	SRO2	47.763	18.394	109	Guralp-40T-1s	Wave24	100/sec	mSEED
Stebnícka Huta	STHS	49.417	21.244	534	LE3D	Wave24	100/sec	mSEED
Šrobárová	SRO	47.813	18.313	150	3× SKM-3	Wave24	100/sec	mSEED

Four additional short period seismic stations has been operated on the jointly bases of ESI SAS and the other institutions. The seismic stations Banka (BAN), Podolie (POD) and Jalšové (JAL) located in the Little Carpathians have been operated in cooperation with Progseis Ltd. company and the Institute of Rock Structure and Mechanics of the Czech Academy of Sciences (IRSM CAS) (*Fojtíková et al., 2015*). The seismic station Pusté Úľany (PULA) has been operated in cooperation with the IRSM CAS. These stations have been installed as temporary seismic stations.

3. Data processing

Digital data from all NNSS stations (except the analog seismic station HRB) are transferred in real-time to the data centre at the ESI SAS either by the

internet or satellite telemetry. Software package SeisComp3 (*Weber et al., 2007*) and SeedLink server are used for data acquisition and exchange.

Beside observations from the NNSS stations the data centre at ESI SAS also use the data from the above mentioned local networks of seismic stations in Slovakia and observations from networks of neighbouring countries: Austrian Seismic Network (*ZAMG – Zentralanstalt für Meterologie und Geodynamik, 1987*), Czech Regional Seismic Network (*Institute of Geophysics, Academy of Sciences of the Czech Republic, 1973*), Hungarian National Seismological Network (*Kövesligethy Radó Seismological Observatory, 1992*), Local seismological network for monitoring NPP Dukovany (*Institute of Physics of the Earth Masaryk University, 2014*), GEOFON Seismic Network (*GEOFON Data Center, 1993*), *Polish Seismological Network*. These stations form a so-called Regional Virtual Network of ESI SAS that consists of approximately 55 seismic stations.

Routine analysis of the digital recordings at the ESI SAS has been performed by the Unix package Seismic handler (*Stammler, 1993*). Interactive locations of seismic events within Seismic Handler are performed by external program LocSat. The collected digital observations are manually processed on the daily basis. The epicentre locations are based on the IASPI91 traveltime curves. Local magnitudes have been determined from the maximum vertical trace amplitudes of Sg waves, using the pre-defined Seismic Handler formula for local events. Continuous raw seismic data from the NNSS are stored in a local archive and seismic data interpretations (together with information on equipment of stations) are stored in a web accessible database.

4. Seismic activity in 2018

The NNSS analyzed 11704 local, regional and teleseismic events in 2018. More than 45800 seismic phases were determined. Seismic events identified as quarry blasts were excluded from further processing and were not included in the event statistics. All events recorded by the NNSS and analyses at the data centre at ESI SAS have been reported in the so called Seismo Reports and published on the above mentioned web sites of the Department of Seismology, ESI SAS.

Altogether 86 seismic events located by the NNSS originated in the territory of Slovakia in 2018 (Fig. 2). Known quarry blasts are not included in

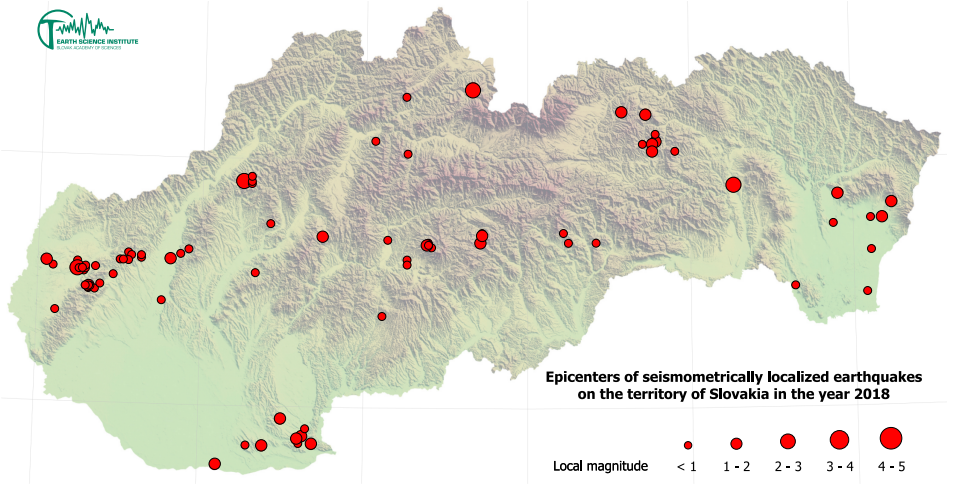

Fig. 2. Map of epicentres of local earthquakes originated on the territory of Slovakia in 2018. Diameters of the circles are proportional to local magnitudes.

this number. 31 earthquakes reached local magnitude 1.0 or more and are listed in Table 2. The strongest earthquake occurred on August 17 at 1:25 UTC in Strážovské Mts. with local magnitude M_L 2.9.

The seismicity of the Slovak territory is dominated by the Little Carpathians and Komárno seismic source zones (*Hók et al., 2016*). The strongest earthquake in the Little Carpathians source zone was detected on the May 7 at 21:23 UTC with local magnitude M_L 1.3. The strongest earthquake in the Komárno source zone was detected on the January 17 at 5:49 UTC with local magnitude M_L 2.0. Although the low level of seismic activity from the last decades remained unchanged in 2018, these two source zones remain of the primary interest for the monitoring of seismic activity within the territory of Slovakia.

5. Macroseismic observations

Five earthquakes were macroseismically felt on the territory of Slovakia in 2018 (Table 3), four of them with the epicentre on the territory of Slovakia and one with the epicentre in Poland (Fig. 3). All of these five earthquakes were also seismometrically observed and processed. Intensities were esti-

Table 2. List of earthquakes originated on the territory of Slovakia in 2018 with $M_L \geq 1.0$.

Date [YYYY-MM-DD]	**Origin Time (UTC) [HH:MM:SS]**	**Lat. [°N]**	**Lon. [°E]**	**Depth [km]**	M_L **[NNSS]**	I_0 **[°EMS]**	**Region**
2018-01-01	04:33:48.46	48.67	19.71	0	1.6	felt	Vepor Mts.
2018-01-02	07:28:58.28	48.70	19.72	0	1.1		Vepor Mts.
2018-01-12	15:24:13.62	49.19	20.73	0	1.4		Levoča Mts.
2018-01-17	05:49:52.23	47.84	18.39	0	2.0		Šamorín – Komárno – Štúrovo
2018-01-31	11:16:09.62	49.08	20.79	0	1.8		Levoča Mts.
2018-02-25	13:16:32.77	48.37	17.11	2.6	1.0		Little Carpathians
2018-03-13	20:05:11.06	48.69	18.74	0	1.8		Vtáčnik Mts.
2018-03-14	08:48:28.14	47.95	18.50	0	1.1		Danubian Hills
2018-04-05	02:51:39.39	47.76	18.11	2.9	1.7	felt	Šamorín – Komárno – Štúrovo
2018-04-10	23:30:20.01	49.20	20.58	0	1.1		Levoča Mts.
2018-04-22	17:10:18.02	48.82	22.24	4.4	1.4		Vihorlat Mts.
2018-04-26	13:04:46.31	48.59	17.81	0	1.2		Považský Inovec Mts.
2018-05-07	21:23:58.66	48.47	17.31	0.6	1.3		Little Carpathians
2018-05-16	08:13:00.88	48.86	21.91	3.0	1.2		Vihorlat Mts.
2018-06-11	09:11:40.00	49.07	20.77	0	1.4		Levoča Mts.
2018-07-20	13:44:18.40	49.04	20.77	0	1.2		Levoča Mts.
2018-08-17	01:25:12.86	48.91	18.25	0.3	2.9	4	Strážov Mts.
2018-08-24	14:410:43.75	48.90	21.27	0	2.1		Slanské Hills
2018-09-11	17:32:02.68	48.46	22.08	0	1.0		East Slovak Lowland
2018-10-02	21:56:53.28	47.88	18.63	2.2	1.7		Šamorín – Komárno – Štúrovo
2018-10-02	23:22:08.63	47.85	18.69	0	1.2		Ipeľ Hills
2018-10-14	15:37:33.84	48.67	19.39	0	1.0		Poľana

Table 2. Continued from the previous page.

Date [YYYY-MM-DD]	Origin Time (UTC) [HH:MM:SS]	Lat. [°N]	Lon. [°E]	Depth [km]	M_L [NNSS]	I_0 [°EMS]	Region
2018-10-17	04:32:13.12	48.66	19.38	0	1.3		Poľana
2018-11-06	14:05:14.03	48.57	17.05	0	1.1		Záhorie region
2018-11-12	09:07:04.00	48.76	22.18	5.1	1.1		Vihorlat Mts.
2018-11-14	23:16:12.71	49.29	19.66	0.8	2.1		High Tatras
2018-11-19	22:09:51.82	47.85	18.61	0	1.0		Šamorín – Komárno – Štúrovo
2018-11-27	22:29:37.37	47.87	18.60	0	1.2		Šamorín – Komárno – Štúrovo
2018-12-16	15:05:37.30	48.54	17.24	5.4	2.3	3	Záhorie region
2018-12-17	04:57:35.95	48.54	17.25	3.6	1.0		Záhorie region
2018-12-31	04:51:18.14	48.60	17.63	2.9	1.0		Little Carpathians

Table 3. List of macroseismically observed earthquakes on the territory of Slovakia in 2018.

Date [YYYY-MM-DD]	Origin Time (UTC) [HH:MM:SS]	Lat. [°N]	Lon. [°E]	Depth [km]	M_L [NNSS]	I_0 [°EMS]	Region
2018-01-01	04:33:48.5	48.68	19.71	0	1.6	–	Vepor Mts.
2018-04-05	02:51:39.4	47.76	18.12	3	1.7	–	Komárno
2018-07-15	21:19:50.3	49.34	20.93	7	2.6	–	Krynica
2018-08-17	01:25:12.9	48.91	18.25	1	2.9	4	Strážov Mts.
2018-12-16	15:05:37.3	48.54	17.24	5	2.3	3	Záhorie

mated by the European Macroseismic Scale 1998 (EMS-98) introduced by *Grünthal (1998)*.

The earthquake on January 1 at 4:33 UTC with epicentre near Brezno and local magnitude 1.6 was macroseismically felt on 1 location (Table 4). Because of lack of macroseismic data it was not possible to determine the epicentral intensity.

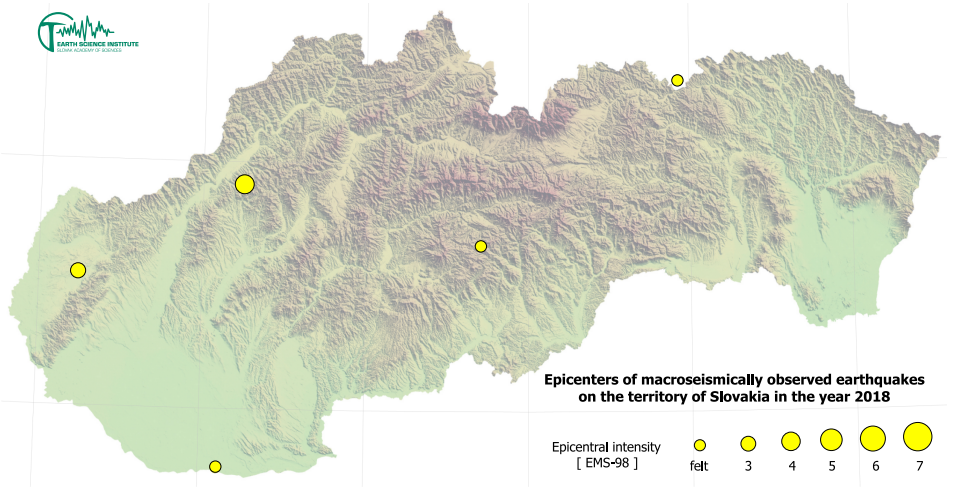

Fig. 3. Map of epicentres of macroseimically observed earthquakes on the territory of Slovakia in 2018. Diameters of the circles are proportional to epicentral intensity.

The earthquake on April 5 at 2:51 UTC with epicentre near Komárno and local magnitude 1.6 was macroseismically felt on 2 locations (Table 5). Because of lack of macroseismic data it was not possible to determine the epicentral intensity.

The earthquake on July 15 at 21:19 UTC with epicentre near Krynica, Poland and local magnitude 2.6 was macroseismically felt on 16 locations within the territory of Slovakia (Table 4). 47 macroseismic questionnaires were filled. People reported weak trembling or shaking and acoustic effects – rumbling. The maximum intensity on the territory of Slovakia was determined at 3–4° EMS-98.

The earthquake on August 17 at 1:25 UTC with epicentre near Trenčianske Teplice and local magnitude 2.9 was macroseismically felt on 26 locations (Table 7). 178 macroseimic questionnaires were filled. The event was described as a light trembling. Some people reported acoustic effects – rumbling and fizzling. The epicentral intensity was determined at 4° EMS-98.

The earthquake on December 16 at 15:05 UTC with epicentre in Záhorie region and local magnitude 2.3 was macroseismically felt on 4 locations (Table 8). 5 macroseimic questionnaires were filled. The event was described as a light trembling. The epicentral intensity was determined at 3° EMS-98.

Table 4. Macroseismic observations for January 1, 2018 earthquake, 4:33 UTC.

Locality	**Lat.** [°**N**]	**Lon.** [°**E**]	**No. of questionnaires**	***I*** [°**EMS-98**]
Čierny Balog	48.744	19.645	1	felt

Table 5. Macroseismic observations for April 5, 2018 earthquake, 2:51 UTC.

Locality	**Lat.** [°**N**]	**Lon.** [°**E**]	**No. of questionnaires**	***I*** [°**EMS-98**]
Komárno	47.766	18.118	1	felt
Nová Stráž	47.764	18.044	1	felt

Table 6. Macroseismic observations for July 15, 2018 earthquake, 21:19 UTC.

Locality	**Lat.** [°**N**]	**Lon.** [°**E**]	**No. of questionnaires**	***I*** [°**EMS-98**]
Malcov	49.305	21.065	8	3–4
Andrejovka	49.288	20.901	1	3–4
Hniezdne	49.304	20.632	1	3–4
Bardejov	49.297	21.272	7	3
Kružlov	49.311	21.136	4	3
Čirč	49.282	20.924	1	3
Sveržov	49.337	21.165	1	3
Hrabské	49.320	21.070	6	felt
Kurov	49.342	21.136	5	felt
Lenartov	49.310	21.017	4	felt
Gerlachov	49.098	20.210	3	felt
Snakov	49.326	21.046	2	felt
Fričkovce	49.186	21.245	1	felt
Gaboltov	49.367	21.145	1	felt
Lipany	49.156	20.964	1	felt
Lukov	49.293	21.083	1	felt

6. Conclusion and discussion

The NNSS is operated by the ESI SAS, Bratislava. Data from all stations (except station HRB) are transferred in real-time to the data centre at Bratislava. Data processing and routine analysis are performed digitally by in-

Table 7. Macroseismic observations for August 17, 2018 earthquake, 1:25 UTC.

Locality	**Lat.** [°**N**]	**Lon.** [°**E**]	**No. of questionnaires**	***I*** [°**EMS-98**]
Horná Súča	48.980	17.950	1	4
Motešice	48.824	18.183	1	4
Dubnica nad Váhom	48.958	18.183	63	3
Trenčianske Teplice	48.908	18.180	26	3
Omšenie	48.902	18.226	6	3
Trenčianska Teplá	48.937	18.121	6	3
Trenčín	48.890	18.043	5	3
Nemšová	48.970	18.115	3	3
Košecké Podhradie	48.969	18.311	2	3
Báb	48.307	17.872	1	3
Bojnice	48.779	18.583	1	3
Bolešov	49.000	18.170	1	3
Dobrá	48.923	18.106	1	3
Kopec	48.949	18.342	1	3
Nové Mesto nad Váhom	48.758	17.829	1	3
Poriadie	48.773	17.607	1	3
Pruské	49.031	18.201	1	3
Púchov	49.124	18.326	1	3
Nová Dubnica	48.938	18.161	38	felt
Horná Poruba	48.952	18.293	6	felt
Ilava	48.982	18.243	6	felt
Dolná Poruba	48.905	18.285	2	felt
Opatová	48.914	18.096	1	felt
Prejta	48.974	18.217	1	felt
Vyškovce nad Ipľom	48.072	18.864	1	felt
Žilina	49.219	18.751	1	felt

Table 8. Macroseismic observations for December 16, 2018 earthquake, 15:05 UTC.

Locality	**Lat.** [°**N**]	**Lon.** [°**E**]	**No. of questionnaires**	***I*** [°**EMS-98**]
Prievaly	48.558	17.350	2	3
Bílikove Humence	48.586	17.238	1	3
Buková	48.544	17.411	1	3
Lakšárska Nová Ves	48.569	17.159	1	3

teractive seismological software Seismic Handler. Digital data are accessible both on-line and off-line in standard data format. So called Seismo Reports of seismic events recorded by NNSS are published on the web page of the ESI SAS `http://www.seismology.sk/Seismo_Reports/reports.html`.

The lack of system approach to financing of the NNSS persisted also in 2018. The contribution from the budget of the Slovak Academy of Sciences is assigned for a day-to-day operation of the NNSS with insufficient additional funds for network improvement. In 2018 one new broadband sensor was purchased (the new sensor replaced the functionless one on VYHS station).

Epicentres and local magnitudes were determined for 86 earthquakes originated on the territory of Slovakia in 2018. Weak seismic activity was recorded from several seismic source zones: Little Carpathians, Komárno, Záhorie, Strážov Mts. and Vepor Mts.

Acknowledgements. The authors have been supported by the Slovak Foundation Grant VEGA 2/0144/19 and The Slovak Research and Development Agency Grant APVV-16-0146.

References

ESI SAS (Earth Science Institute of the Slovak Academy of Sciences), 2004: National Network of Seismic Stations of Slovakia. Deutsches GeoForschungsZentrum GFZ, Other/Seismic Network, `doi: 10.14470/FX099882`.

Fojtíková L., Kristeková M., Málek J., Sokos E., Csicsay K., Záhradník J., 2015: Quantifying capability of a local seismic network in terms of locations and focal mechanism

solutions of weak earthquakes. J. Seismol., **20**, 1, 93–106, doi: 10.1007/s10950-015-9512-1.

GEOFON Data Center, 1993: GEOFON Seismic Network. Deutsches GeoForschungsZentrum GFZ, Other/Seismic Network, doi: 10.14470/TR560404.

Grünthal G. (Ed.), 1998: European Macroseismic Scale 1998 EMS-98. Cahiers du Centre Européen de Géodynamique et de Séismologie, **15**, Luxembourg, 101 p., online, accessed 6 April 2019, available from: http://gfzpublic.gfz-potsdam.de/pubman/item/escidoc:56109:4/component/escidoc:56108/EMS-98_Original_englisch_pdf.pdf.

Hók J., Kysel R., Kováč M., Moczo P., Kristek J., Kristeková M., Šujan M., 2016: A seismic source zone model for the seismic hazard assessment of Slovakia. Geol. Carpath., **67**, 3, 273–288, doi: 10.1515/geoca-2016-0018.

Institute of Geophysics, Academy of Sciences of the Czech Republic, 1973: Czech Regional Seismic Network. International Federation of Digital Seismograph Networks, Other/Seismic Network, doi: 10.7914/SN/CZ.

Institute of Physics of the Earth Masaryk University (Czech), 2014: IPE_EDU. International Federation of Digital Seismograph Networks, Other/Seismic Network, doi: 10.7914/SN/D1.

Kövesligethy Radó Seismological Observatory (Geodetic and Geophysical Institute, Research Centre for Astronomy and Earth Sciences, Hungarian Academy of Sciences (MTA CSFK GGI KRSZO)), 1992: Hungarian National Seismological Network. Deutsches GeoForschungsZentrum GFZ, Other/Seismic Network, doi: 10.14470/UH028726.

Liščák P., Petro Ľ., Papčo J., Cipciar A., Csicsay K., Kristeková M., Stercz M., Pacajová K., Bednárik M., Briestenský M., Bella P., 2019: Partial Monitoring System – Geological Factors, Subsystem 02: Tectonic and seismic activity of the territory, Geological work number 207, Report for 2018 (Čiastkový monitorovací systém – Geologické faktory, Podsystém 02: Tektonická a seizmická aktivita, číslo geologickej úlohy 207, správa za obdobie: rok 2018). State Geological Institute of Dionýz Štúr, Regional centre Košice (in preparation).

Local Seismic Network of Eastern Slovakia. Faculty of Mathematics, Physics of the Earth and Informatics, Comenius University, html://www.fyzikazeme.sk/mainpage/index_en.htm.

Pajdušák P., 1997: Historical seismic instruments at the stations Hurbanovo (HRB) and Skalnaté pleso (SPC) of Slovakia. Cahiers du Centre Européen de Géodynamique et de Séismologie, **13**, 49–60.

Polish Seismological Network (PLSN), Institute of Geophysics Polish Academy of Sciences, https://www.igf.edu.pl/stacje-en.php.

Stammler K., 1993: Seismichandler—Programmable multichannel data handler for interactive and automatic processing of seismological analyses. Comput. Geosci., **19**, 2, 135–140, doi: 10.1016/0098-3004(93)90110-Q.

Weber B., Becker J., Hanka W., Heinloo A., Hoffmann M., Kraft T., Pahlke D., Reinhardt J., Thoms H., 2007: SeisComp3 – automatic and interactive real time data processing. Geophysical Research Abstracts In EGU General Assembly, **9**, 09129.

ZAMG – Zentralanstalt für Meterologie und Geodynamik, 1987: Austrian Seismic Network. International Federation of Digital Seismograph Networks, Other/Seismic Network, doi: 10.7914/SN/OE.